# Development of the Back End Electronics for the Wide Field Monitor on-board LOFT

Diploma Thesis

submitted by

Florian Jetter

Eberhard Karls University Tübingen
Faculty of Science
Kepler Center for Astro and Particle Physics
Section for High Energy Astrophysics

July 14, 2014

*We are at the very beginning of time for the human race. It is not unreasonable that we grapple with problems. But there are tens of thousands of years in the future. Our responsibility is to do what we can, learn what we can, improve the solutions, and pass them on.*

- Richard Feynman

# Abstract

The Large Observatory for X-Ray Timing (LOFT) originally was a mission candidate for the ESA M3 launch opportunity within the Cosmic Vision program. Due to the selection of the competing PLATO mission for the M3 launch slot, LOFT will also be proposed as a M4 mission candidate with a slightly altered design. The goal of the LOFT mission is to study matter under extreme conditions using the Large Area Detector instrument, i.e. to determine the equation of state of ultra dense matter in neutron stars and to test the predictions of general relativity by observing the effects of strong field gravity in the vicinity of black holes, as well as the long time observation of transient X-ray sources and the Detection of Gamma Ray Bursts with the Wide Field Monitor instrument (WFM).

This diploma thesis is dedicated to the development of the Back End Electronics (BEE) for the WFM instrument on-board the LOFT mission. The functionality of the BEE includes the communication with the Front End Electronics of the WFM cameras, the application of corrections to the recorded event data, the reconstruction of the incident photon's energy and position on the detector plane and the transmission of these data to the Detector Handling Unit. This was realized by the development of a configuration file for a Virtex-4 FPGA, using the hardware description language VHDL.
This thesis will start with a short introduction to the history of X-ray astronomy and will continue by giving an overview of the LOFT mission, the Large Area Detector instrument and the addressed scientific goals. Section 3 will introduce the Wide Field Monitor instrument of the LOFT mission, discuss its electronics design, the hardware used, as well as the science goals addressed by this instrument and the observed objects. The next section will then give a detailed description of the functionality of the BEE and how it was realized in the frame of this thesis. Section 5 will present the achieved results, discuss open tasks and suggest possible improvements, while Section 6 will conclude this thesis and give outlook into the future.

# Zusammenfassung

Diese Diplomarbeit befasst sich mit der Entwicklung der Back End Electronics für das Wide Field Monitor Instrument des Large Observatory for X-ray Timings (LOFT). LOFT ist eine Mission, die ursprünglich als Kanditat für die M3 Ausschreibung der ESA entwickelt wurde. Durch die Auswahl der PLATO Mission bei der M3 Ausschreibung, war diese ursprünglich angestrebte Realisierungsmöglichkeit für LOFT nicht weiter machbar. Derzeit werden verschiedene Möglichkeiten, die Mission mit einem teils veränderten Design weiter zu verfolgen, geprüft. Eine dieser Möglichkeiten, welche derzeit angestrebt wird, wäre das Einreichen eines Entwurfs für die M4 Ausschreibung der ESA.

LOFT umfasst zwei Instrumente: Den Large Area Detector (LAD), welcher das Hauptinstrument zur Verfolgung der wissenschaftlichen Ziele darstellt, und den Wide Field Monitor (WFM), welcher für die simultane Langzeitbeobachtung veränderlicher Quellen entworfen wurde und welcher den LAD beim Erreichen der wissenschaftlichen Ziele unterstützt. Im Rahmen dieser Diplomarbeit wird zuerst eine kurze Einführung in die Geschichte der beobachtenden Hochenergieastrophysik gegeben. Das darauffolgende Kapitel beschäftigt sich dann mit der LOFT Mission. Der LAD sowie die mit diesem Instrument angestrebten wissenschaftlichen Ziele werden in diesem Kapitel genauer erläutert. Im dritten Kapitel werden der WFM sowie eine Auswahl der mit ihm beobachteten Objekte und Phänomene vorgestellt. Kapitel 4 widmet sich der Back End Electronics (BEE) des WFM und damit dem eigentlichen Thema dieser Diplomarbeit. Die Funktionalität dieser Komponente wird durch die Konfiguration eines FPGAs mit einer durch VHDL Programmierung erzeugten Bitfile erreicht. Die BEE ist für die Kommunikation mit weiteren elektronischen Komponenten, sowie für Korrekturen und die Rekonstruktion vom Detektor registrierter Ereignisse zuständig. Die für die Kommunikation verwendete Technik, die den Korrekturen zugrunde liegenden Ursachen, die für die Rekonstruktion verwendeten Algorithmen und die erarbeitete Realisierung werden erläutert.
Die erzielten Ergebnisse werden in Kapitel 5 zusammengefasst, offene Aufgaben diskutiert und mögliches Verbesserungspotential aufgezeigt, wohingegen Kapitel 6 diese Diplomarbeit mit einem Ausblick in die Zukunft abschließt.

# Contents

# Chapter 1

# Introduction

Observational astronomy has come a long way since the invention of the first telescope. These instruments have run through a lot of improvements from the first use of a telescope for astronomical observations by Galileo Galilei around 1609, to the invention of the first mirror telescope by Isaac Newton in 1672 to the use of giant telescopes by George Hale in the first decades of the 20th century. These instruments established the observations and revolutionary discoveries of many famous scientists like Johannes Kepler (1571–1630), Charles Messier (1730–1817) and Edwin Hubble (1889–1953) to name just a few, which shaped our view of our solar system and the cosmos. Telescopes thus were the core of observational astronomy until deep into the 20th century.

However, the most pioneering advance in the history of observational astronomy was doubtless the overcoming of the restriction to groundbased observations, to the feasibility of spaceflight observatories. While many of the greatest successes have been achieved with groundbased observatories, these observatories were limited in the optical regime by disturbances caused by turbulences in the atmosphere and they were unable to perform observations at shorter wavelengths due to the absorption of highly energetic electromagnetic radiation by the atmosphere. The technical advances in the second half of the 20th century allowed to overcome these constraints. They led to the era of spaceflight and an emerging multiwavelength astronomy, extending the observable universe to higher energies.
This era started with the rocket missions in the late 1940s, which led to the identification of the Sun as an X-ray source by the Naval Research Laboratory in 1949, the discovery of Scorpius X-1 as first X-ray source beyond our solar system in 1962 (Giacconi et al. 1962) and gave birth to the branch of experimental X-ray astronomy. The successful launch of the first satellite Sputnik 1 in 1957 finally heralded the feasibility of orbiting astronomical observatories. In 1970 the first X-ray satellite UHURU was launched and performed the first survey of the X-ray sky. Until 1999 the X-ray sky was mapped two more times by HEAO-1* between 1977 and 1979 and by ROSAT between 1990 and 1999, leading to the discovery of approximately 150.000 X-ray sources. The

* High Energy Astronomy Observatory 1

increasing accessibility of highly energetic astronomical sources was correlated with the invention of new observational techniques. The HEAO-2* mission launched in 1978 was the first observatory using Wolter optics: A new type of focusing X-ray mirrors, which is used very successfully in today's largest X-ray observatories, ESA's XMM Newton† and NASA's Chandra X-ray Observatory. The simultaneous increase in computational power permitted the invention of the technique of coded mask imaging, which allows imaging wide field observations in the X-ray and $\gamma$-ray band. Its first use in space observatories was aboard the RXTE ASM‡ in 1995 and aboard BeppoSAX in 1996. Within six months after its launch, BeppoSAX provided for the first time the fast identification of bright, short lived flashes of gamma rays called Gamma Ray Bursts and allowed the identification of their extragalactical origin (Feroci et al. 1998). Today the coded mask's successful applications continue on recent instruments like the BAT§ on NASA's Swift satellite observatory and IBIS¶ on Integral‖.

Future missions will benefit from the continuous technical advancement in recent years. These advances include the invention of more accurate detectors and further improvements in miniaturization, leading to the preciser fabrication of even smaller structures as used for modern collimators or in electronic components like FPGAs. A significant increase in computational power established advanced onboard data processing and data reduction as well as in an increase in the bandwidth for the telemetry from the spacecraft to the ground. These advances make new instruments with a larger collective area, a higher precision in spatial resolution as well as in temporal resolution and an increased data throughput feasible, and thus allow to address open questions in astronomy, to which providing an answer by observations has yet been out of reach.
One of these future missions is the Large Observatory for X-ray Timing (LOFT). LOFT mission concept was developed by the LOFT consortium in the frame of ESA's M3 call for proposals. The mission's main instrument, the Large Area Detector, has an unprecedented huge effective area of $10\,\mathrm{m}^2$ at 6 keV. This large collective area, its modular design and the modern Silicon Drift Detectors used for the instrument will allow observations with a very high timing resolution of 1 µs. With these capabilities it is dedicated to determine the composition of neutron stars and to observe the effects of spacetime bending near black holes. The mission's second instrument is called the Wide Field Monitor and is a well suited addition to the Large Area Detector. While the Large Area Detector is a collimated, non imaging instrument with a narrow field of view, the Wide Field Monitor is an imaging, coded mask instrument with a wide field of view of 4.1 steradian. The Wide Field Monitor will perform long time observations of a large number of transient sources

* High Energy Astronomy Observatory 2, also known as Einstein Observatory
† X-ray Multi-Mirror
‡ Rossi X-ray Timing Explorer's All-Sky Monitor
§ Burst Alert Telescope
¶ Imager on-Board the INTEGRAL Satellite
‖ International Gamma-Ray Astrophysics Laboratory

simultaneously, discover new sources and provide a fast notification to ground in case of the detection of Gamma Ray Bursts. Both of these instruments have to master new technical challenges, which appear with the use of these new technologies. This diploma thesis is dedicated to one of these challenges and addresses the development of the Back End Electronics (BEE) for the LOFT mission's Wide Field Monitor instrument.

There will be an introduction to compact objects and an overview of the LOFT mission in the second chapter of this document. Science goals of the mission will be discussed as well as the Large Area Detector. The third chapter is dedicated to the Wide Field Monitor. It also includes an overview of relevant sources for observation, the technical requirements to meet the scientific goals and the instrument itself. Chapter number four describes the BEE and represents the main part of this thesis. The tasks of the BEE and their realization in the frame of this thesis will be presented. The achieved results and potential options for further improvements will be critically discussed in Chapter 5, while Chapter 6 concludes the thesis with an outlook into the future.

# Chapter 2

# The LOFT Mission

The Large Observatory for X-ray Timing (LOFT) is an X-ray observatory planned by a collaboration of 22 countries. The content of this section is based on its assessment study report (Barret et al. 2013). LOFT was designed to address ESA's Cosmic Vision theme by putting constraints on the Equation of State (EOS) of ultra-dense matter, testing the predictions of general relativity in the direct surrounding of black holes and long time observations of transient objects. The mission is equipped with two instruments for that purpose.
The Large Area Detector (LAD) is LOFT's main instrument. Its most remarkable attributes are the huge effective area of more than 9.5 $m^2$ at 6 keV, which is larger than that of any other constructed or planned X-ray mission, and a high timing resolution of 10 µs. The LAD will attend to the goals of determining the EOS and to measure the effects of strong field gravity. The LAD is discussed in detail in Section 2.2. LOFT's second instrument is the Wide Field Monitor (WFM). The WFM has a large field of view and is designed for long time observations of transient X-ray sources and for the fast detection of Gamma Ray Bursts with the so-called LOFT Burst Alert System. Since the WFM is an important part of this diploma thesis, it is first discussed as a short overview in Section 2.3 and in following by detailed treatment in Chapter 3. The LOFT satellite will be launched within a Soyuz rocket to its planned low-earth orbit of 550 km with an inclination of $<2.5°$. In that orbit it will have a nominal sky visibility of more than 40 %. It will stay in that orbit for its intended lifetime of $3 + 2$ years and will during that time provide observational data at a rate of 100 Gbit/day. For a detailed overview of LOFT's technical data see Table 2.1.

The LOFT mission was originally planned as one of five competitors for ESA's Cosmic Vision M3 launch slot. LOFT's competitor missions in that call for proposals were:

- The Planetary Transit Observatory (PLATO), which will detect terrestrial exoplanets in the habitable zone of solar-type stars and characterize different types of planets by optical wide-field observations. (Rauer et al. 2013)

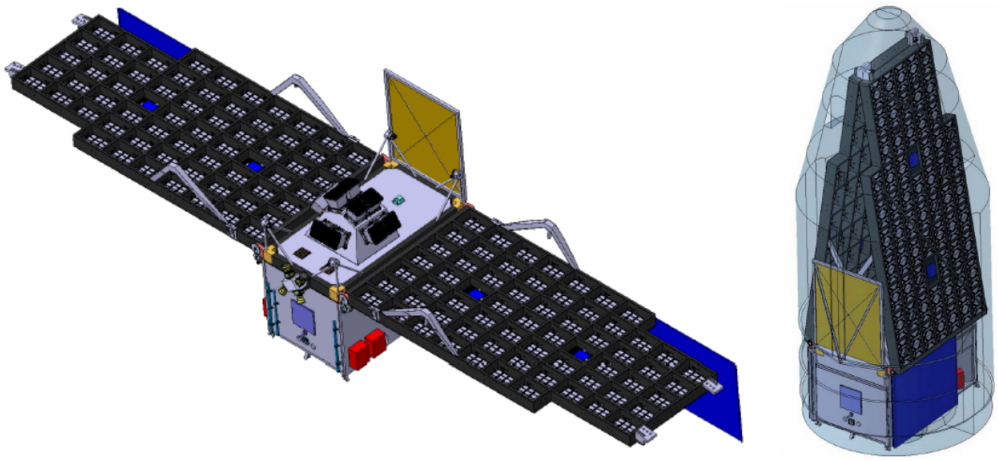

**Figure 2.1:** *Left:* Illustration of one possible LOFT design. The black, grid structured panels at the side of the satellite are detectors of the LAD instrument. The blue area that is only visible in parts is the solar array. The grey, hill-shaped object on the satellite is the WFM. The black, mounted boxes are its cameras, adjusted at different angles to provide a large field of view. The yellow screen is the sunshield to cover the WFM from the Sun's direct radiation. *Right:* The LOFT satellite as it is stored inside the Soyuz. The LAD panels are folded in a vertical position. *Image: Barret et al. 2013*

- MarcoPolo-R, which was designed to retrieve a sample from a near-earth asteroid. (Barucci et al. 2013)
- The Exoplanet Characterization Observatory (EChO), which has the goal to analyze the atmospheres of exoplanets via spectroscopy. (Drossart et al. 2013)
- The Space-Time Explorer and Quantum Equivalence Principle Space Test (STE-QUEST), which will put each sub principle of Einsteins's equivalence principle to test. These sub principles are the Weak Equivalence Principle, the Local Lorentz Invariance and the Local Position Invariance. (Bongs et al. 2013)

On February 18th, 2014, the ESA Science Program Committee decided on the recommendation of Plato as M3 mission. However, LOFT's science goals were recognized by the committee as very strong and LOFT was explicitly ranked 2nd. Based on the positive feedback, the LOFT Consortium therefore announced its intention to continue the development of the mission and to participate in ESA's M4 call for proposals.

**Table 2.1:** Overview of the technical data of the LOFT mission. (Barret et al. 2013)

| | **Large Area Detector** | | **Wide Field Monitor** | |
|---|---|---|---|---|
| **Reference Core Payload** | Effective area: ~10 $m^2$ at 6 keV | | Source localization: 1 arcmin | |
| | Throughput: 240 000 cts/s (1 Crab) | | Angular resolution 5 arcmin | |
| | Maximum flux: 15 Crab | | Energy band: 2 keV–50 keV | |
| | Spectral resolution: 180 eV–240 eV at 6 keV (CCD-class) | | Effective area: 170 $cm^2$ (peak) | |
| | Time resolution: 10 µs | | Sensitivity: 3 mCrab (5 σ, 50 ks) | |
| | Timing capabilities: 15 x RXTE (variability S/N) | | Field of view: 4.1 steradian | |
| | Spectral timing capabilities: >200 x XMM-Newton (FeKα variability S/N at >0.2 Crab) | | Onboard transient events localization | |
| | Sensitivity: 0.1 mCrab in 100 s (5σ) | | Broadcast events coordinates <30 s | |
| | Field of view: 1 degree (collimated) | | Technology: 10 coded mask cameras, 40 Silicon Drift Detectors | |
| | Technology: 2016 Silicon Drift Detectors | | | |
| **Overall Mission Profile** | Lifetime: 3 yr+2 yr | | Low-Earth Orbit: 550 km, <2.5° inclination | |
| | Consumables: 10 yr | | Ground station: Kourou & Malindi | |
| | Launcher: Soyuz | | Pointing: 3 axis stabilized (15 ” knowledge) | |
| | Launch date: 2022 | | Sky visibility: >40% nominal &>65% extended | |
| | High gain antenna: steerable, X-band | | Observing efficiency: >60% | |
| | Data rate: 100 Gbit/day | | | |
| **Description of the Spacecraft** | | **Mass (Kg)** | | **Power (W)** |
| | LAD | 967 | LAD | 1305 |
| | WFM | 125 | WFM | 108 |
| | Service module | 1254 | Service module | 389 |
| | Spacecraft dry mass | 3472 | Losses | 200 |
| | Propellant | 482 | Battery charging | 1450 |
| | Launch adapter | 125 | Total Power demands | 3814 |
| | Total Mass ( + margins) | 4070 | | |

## 2.1 Scientific goals

LOFT was designed for three main scientific goals:

- To put constraints on the EOS of matter of supranuclear density under the extreme conditions occurring in the center or in the surroundings of neutron stars and black holes.
- To put general relativity's predictions of spacetime curvature to test in the direct surrounding of black holes.
- For long time observations of already known and exploration of new transient X-ray sources.

The third goal is addressed mainly by the WFM and it is discussed along with different examples of X-ray transients in Section 3.1, while the first two goals are covered by the LAD. This section gives a short overview of the science behind the goal of putting constraints on the EOS of ultra dense matter and the goal of strong field gravity as well as of the techniques used to address them, starting by giving an introduction to the astronomical objects associated with these science goals.

### 2.1.1 Compact Objects

In high energy astrophysics compact objects are one of the most important sources of radiation, especially when focusing on transient sources. This section therefore gives a short introduction in the formation and in the attributes of compact objects, while the transient sources are discussed in Section 3.1.
When a star has exceeded its lifetime and there is not enough nuclear fuel left to keep the radiation pressure up, it collapses under its own gravitational pressure in a supernova explosion. While the star's outer shells are blown off and create a supernova remnant, the collapsed core remains, keeping large parts of the stars magnetic field and spin. The further evolution of the core depends on the initial star's mass.

- For $M_{star} \leq 4M_{\odot}$ the star evolves into a white dwarf. White dwarfs have masses comparable to that of the Sun, but have a radius similar to that of the Earth. White dwarfs consist mainly of carbon but are not heavy enough to burn it in fusion processes. The pressure keeping the gravitational forces in balance is that of a degenerate electron gas. White dwarfs are the origin of some transient phenomena like novae and dwarf novae.
- If the remaining central object of the supernova explosion has a mass above the Chandrasekhar limit of $1.44\,\mathrm{M}_{\odot}$, the core collapses into a neutron star. Neutron stars are the densest objects in the universe with a typical mass $M$ $\sim$1 $\mathrm{M}_{\odot}$–2 $\mathrm{M}_{\odot}$

and radius $R \approx 10\,\text{km}$–$14\,\text{km}$. These stars were given their name since they are composed mainly of neutrons, which keep them stable by their degeneracy pressure. However the exact composition of neutron stars remains unknown as discussed in Section 2.1.2. Neutron stars are classified in subclasses like magnetars and pulsars dependent on the strength of their magnetic field and their spin. (Woosley and Heger 2014; Ivanova 2013)

- Black holes are amongst the most massive objects in our universe. Black holes are created if the gravitational pressure exceeds the neutron degeneracy pressure and the core collapses completely. They have masses between $3\,M_\odot - 10^{10}\,M_\odot$ and their compactness leads to gravitational potential large enough to bend spacetime, hence below a certain radius even light cannot escape (McConnell et al. 2011). This radius is called Schwarzschild radius and it prohibits the access to any information within this radius. According to the No-Hair theorem a black hole is therefore described only by its mass, its electric charge and by its spin. Even with information within the Schwarzschild radius being out of reach, matter accreting onto a black hole can be observed and is one possible way to get information from the vicinity of these objects. The accreting matter forms a hot accretion disc around the black hole due to the conservation of angular momentum, it circles inwards while emitting radiation, and finally vanishes at the Schwarzschild radius. Since the Schwarzschild radius is a function of the black hole's mass, the observation of radiation emitted by accreting matter and its vanishing point is therefore an indirect way to measure the black hole's mass. Another phenomenon allowing to measure a black hole's mass is the effect of spacetime bending. According to general relativity objects with compactnesses in the order of black holes bend spacetime. These curvatures result in the gravitational lensing effect, making sources behind and obscured by the black hole visible. Another effect predicted by general relativity is the so-called Frame-Dragging or Lense-Thirring effect (Lense and Thirring 1918). This effect is caused by the rotation of an astronomical object, which affects the motion of an orbiting object by dragging its inertial frame. LOFT will test the predictions of general relativity in the direct vicinity of black holes.

### 2.1.2 The Equation of State of supranuclear density matter

The Equation of State (EOS) of matter with supranuclear density describes the behavior and composition of matter under different pressures, temperatures and densities. For extreme densities in the order of the nuclear matter saturation density $\rho_\infty$ as in neutron stars, a theoretical approach to the EOS by computer simulations is not possible because of the so called fermion sign problem (Barret et al. 2013). This problem has its origin in the odd parity of fermions, e.g. protons and neutrons, creating additional terms for

many-body systems. As a result, the predictions of Quantum-Chromodynamics for many-body systems under extreme densities cannot be computed yet and so phenomenological models are used.
Today there are several models, which make different predictions on the composition of a compact object with a certain mass and, as a result, yield different predicted radii. Vice versa it is possible to measure the composition of a neutron star by determining its mass and radius. Since neutron stars are the densest objects in the universe, they are thus the perfect objects to test the EOS for ultra-dense matter.

Observations with the LAD will help to put constraints on the EOS by employing three different techniques to measure M and R. Each of these techniques is used on a different type of neutron star.

- Pulse Profile Modeling is used for accretion powered sources, which have a hot spot due to magnetic channeling of accreting material and/or thermonuclear X-ray bursts (Section 3.1). The rotation of the neutron star results in an oscillation in the flux measured by the observer. The frequency of this pulsation gives the angular velocity. Doppler boosting affects the color of the spectra and relativistic beaming increases the amplitude, both yielding the velocity at the neutron star's surface. Together these results constrain the radius R of the neutron star.
  The mass can be calculated by effects of general relativity. Gravitational light bending effects make parts of the hot spot visible, even while on the far side of the neutron star, affecting the amplitude of the pulse profile. The strength of this effect depends on the compactness M/R of the neutron star. With the result for R from above one is able to deduce the mass M. For this calculation one has to take into account other parameters such as the hot spot size and its inclination, the observer's inclination, emission from the star and the disc. However, calculating M and R from these measurements is possible (Bauböck et al. 2013; Psaltis, Ozel, and Chakrabarty 2013; Lo et al. 2013).

- Spin measurements of neutron stars can put constraints on the EOS by measuring the limiting spin rate at which mass shedding occurs. According to Haensel et al. 2009 the maximum spin rate is given by the empirical formula

$$f_{\max} \approx C \left(\frac{M}{M_\odot}\right)^{\frac{1}{2}} \left(\frac{R}{10\,\mathrm{km}}\right)^{-\frac{3}{2}}.$$

  $M$ is the gravitational mass of the rotating star and $R$ is the radius of the non-rotating star of the same gravitational mass. $C$ depends on the EOS (e.g. for the EOS consisting of baryons and mesons C = 1.08 kHz) and so does $f_{max}$. The discovery of neutron stars spinning faster than currently observed will put constraints on the EOS. Currently the fastest spinning neutron star PSR J1748-2446ad, that has a frequency of 716 Hz (Hessels et al. 2006). It was discovered with the Green-Bank-Observatory radio telescope. However, during an accretion phase neutron

stars are visible in the X-ray wavelength (see Section 3.1). Accretion powered pulsations are known to show up periodically (Casella et al. 2008; Altamirano et al. 2008). Observations suggest that this phenomenon is more likely to occur for faster spin rates (Barret et al. 2013). LOFT's sensitivity to detect brief pulsations is well suited to discover more neutron star spins.

- Asteroseismology is a technique to study the interior of stars by detection of seismic vibrations. In the case of neutron stars, these vibrations originate from giant flares or intermediate flares and are visible as oscillations in the spectrum (Barret et al. 2013). Because the occurance of these flares is unpredictable, it is important that these QuasiPeriodic Oscillations (QPO) in the hard X-ray emission can be detected by the LAD even via off-axis detection at higher energies. By analyzing the fundamental oscillations and the overtones, one can constrain mass and the radius of the neutron star as shown in Figure 2.2.

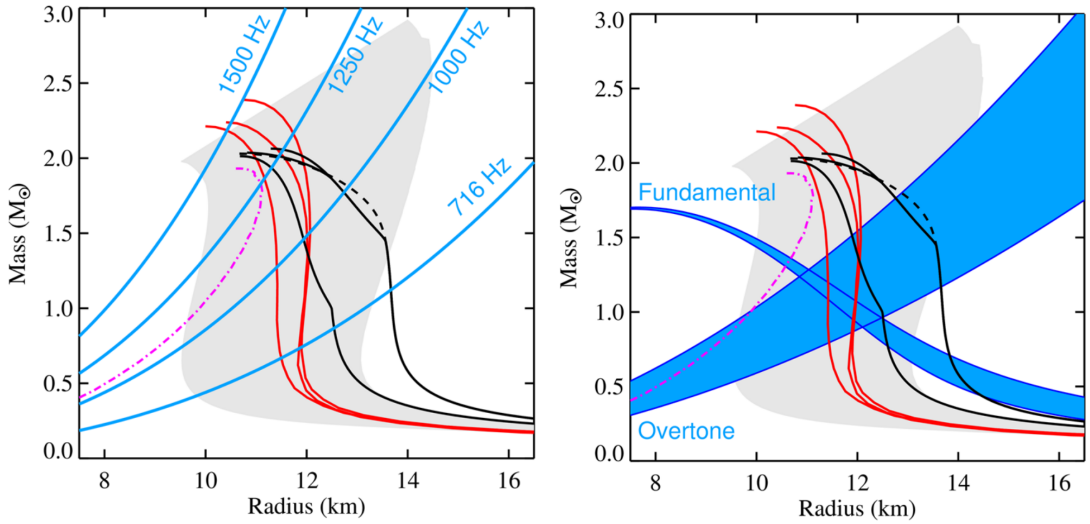


**Figure 2.2:** Both figures show different possible EOS. The gray area shows the possible range for chiral effective theory based EOS (Hebeler et al. 2013), the black solid line shows the possible range for a hybrid EOS (Zdunik and Haensel 2013), while the black dashed line illustrates the range for a nucleon and hyperon core EOS (Bednarek et al. 2012). The red lines are calculated for a nucleonic neutron star and the magenta line is calculated for a quark star (Pons et al. 2002).
*Left:* Spin Limits on the EOS. Spinning neutron stars must lie to the left of or above the corresponding frequency line, otherwise mass-shedding would occur. This puts constraints on the mass and radius of the object, but can as well rule out some EOS if spin frequencies high enough are observed. *Right:* Constraints on mass and radius by measurement of fundamental oscillation and overtones in the spectrum of SGR 1806-20. The neutron star's mass and radius are constricted to the overlap of both blue bands.
*Image: A. Watts / LOFT Assessment Study Report*

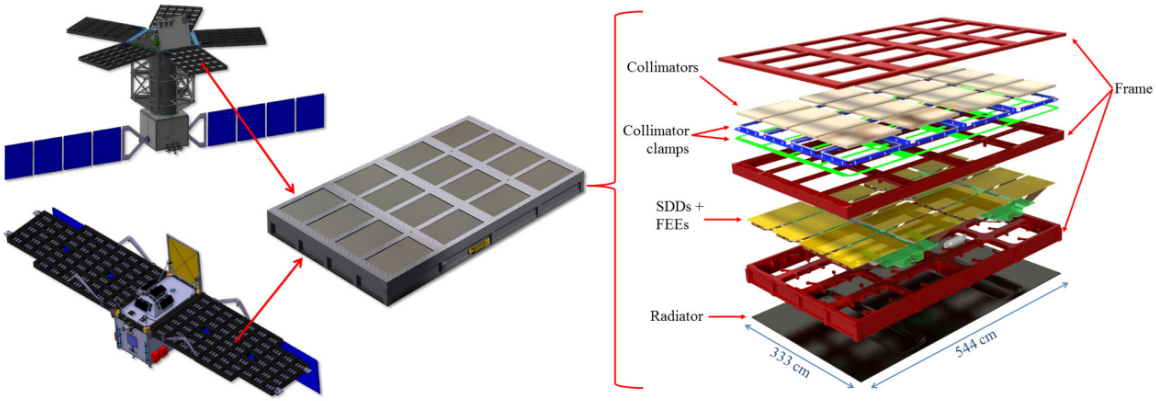


**Figure 2.3:** *Left:* Different LAD designs, either with five panels (*top*) or two panels (*bottom*). Each panel supports a total number of 25 modules (*top*) or 62 modules (*bottom*). *Middle:* A LAD module consisting of 4x4 SDDs. On the side of the module a connector for the 28 V supply voltage and data transmission can be seen. *Right:* Different components of the module. Assembly of MCP collimators, SDDs, FEEs and their framework. To dissipate heat from the module there is a radiator at the bottom. *Image: Barret et al. 2013*

### 2.1.3 Strong Field Gravity

The second large science goal of LOFT is to test the predictions of general relativity at a distance of a few Schwarzschild radii from a black hole. In the inner regions of its accretion disc, material reaches velocities in the order of the speed of light. Most of the energy released by the accretion is released in these regions and the radiation therefore includes information about the curvature of the spacetime as well as information about the mass and spin of the black hole (LOFT Consortium 2012). This information can be retrieved by analysis of either QPOs or the relativistically broadened Fe $K_\alpha$ line (Dauser et al. 2010; van der Klis et al. 1996). LOFT will be the first experiment able to resolve the relativistically broadened Fe line spectrally as well as temporally for supermassive black holes with a mass of $10^8\,M_\odot$ and stellar mass black holes. Stellar mass black holes are especially important, because spacetime curvatures at the event horizon scale with $M_{\rm BH}^{-2}$ and are therefore stronger for smaller $M_{\rm BH}$.

## 2.2 The Large Area Detector

The Large Area Detector (LAD) is the main instrument of LOFT. It is designed for spectroscopy and variability measurements of faint sources down to a detection threshold

of 0.1 mCrab in 100 s (5 σ), has a time resolution of 10 µs and a spectral resolution of 180 eV in the beginning of the mission down to 240 eV at 6 keV in the end of the mission. The loss in the energy resolution in due to damages on the Silicon Drift Detectors (SDD) caused by particles and micro meteorites. To achieve these requirements the LAD has a huge effective area of around 10 $m^2$ at 6 keV. It is a collimated instrument with a field of view of 1 degree. It will probe the motion of matter close to black holes and neutron stars by measuring the variability in the X-ray flux and the spectral variability. This will allow to put constraints on the EOS and measure the effects of strong field gravity as described in Section 2.1.
There are currently three different favored designs of the LAD, differing in the number of panels and slightly in the number of modules used. The first model was proposed by the LOFT consortium and favors a telescope with 6 panels of 21 modules each resulting in an effective area of 12 $m^2$ at 8 keV (Feroci et al. 2012). The other two models are the result of an industrial study and include either 2 or 5 deployable panels consisting of a total number of 124 modules for 2 panels or 125 modules for 5 panels (Figure 2.3, left hand side). Both have a total anticipated effective area of 9.8 $m^2$ at 6 keV. The facts presented in this section are based on the industrial study (Barret et al. 2013).

The LAD has a strict hierarchical and modular design. A module is the LAD's most basic unit. As shown on the right hand side of Figure 2.3, a module consists of different components and their framework. On top there is a film of aluminium with a thickness of 80 nm to reflect sunlight and acts as thermal shield. Below follow 16 X-ray collimators, one for each SDD. To achieve a field of view $< 1$ degree micro-channel plates (MCP) originally designed for BepiColombo* are used. These MCPs consist of a 5 mm thick layer of Lead glass and provide an open area ratio of 70%. Lead glass is a good absorber for radiation with energies up to 30 keV. The LAD is still sensitive for energies up to 80 keV, but since the photoelectric effect's cross section decreases for higher energies the field of view increases.
Between MCP and SDD there is a 1 µm film of Kapton coated with 40 nm aluminum that filters out UV light. Each module consists of 16 Silicon Drift Detectors differing from those used in the WFM (see Section 3.4) in the number of anodes and dimensions. There are 224 anodes per SDD with an anode pitch of 970 µm for the LAD in contrast to 896 anodes per SDD with an anode pitch of 145 µm in the WFM. The layer below the SDDs is made of Pb to shield the detector from the backside and a radiator to dissipate heat completes the module.

*BepiColombo is a planned orbiter mission to Mercury. It is a joint project of the ESA and the JAXA with a planned launch in 2016 (*Source: ESA*).

### Hierarchical design

The LAD's electronic design differs strongly from that of the WFM. With a total of 124 – 126 modules (depending on the design) the LAD's electronics need to be organized very hierarchically to minimize error susceptibility and the amount of cables used. These modules are embedded in the hierarchical structure as shown in Figure 2.4. To read out the anodes, each SDD has a Front End Electronics (FEE) consisting of 14 ASICs. All the FEEs of one module are handled by the so called Module Back End Electronics (MBEE). The communication between FEE and MBEE is the same for the LAD and the WFM and is discussed in detail in Section 4.2. The module also contains a Power Supply Unit (PSU) which converts the supply voltage of 28 V to 3.3 V for the MBEE and FEE and 100 V and 1.3 keV for the SDDs.

The MBEEs are handled by the Panel Back End Electronics (PBEE) and one PBEE handles either 25 or 31 modules depending on the satellite design. The MBEEs transmit the science and housekeeping data to the PBEE, which sends it to the ICU via a SpaceWire connection (see Section 4.5.1). In turn, the PBEE distributes the clock-signal and supply power to the MBEE. The ICU consists of the Data Handling Unit (DHU), the Power Distribution Units (PDU) and the mass memory to store science data and will be cold redundant. Cold redundancy means, that the connection to the redundant unit is only established in cases where the connection to the primary unit is lost. The DHU stores, compresses, and transmits the data received by the PBEE to the ground while the ICU handles the communication with the PBEE and the spacecraft. The health of the instruments is also observed by the ICU. Again, this hierarchical, modular design is crucial for the mission, since it minimizes the instruments weight and the required data rate (since MBEE and PBEE already reduce redundant data) and thus enables the large effective area of about 10 $m^2$ at 6 keV with an event data throughput of 240 000 cts/s (1 Crab) and a maximum flux of 15 Crab.

## 2.3 The Wide Field Monitor

The second instrument of LOFT is the WFM, which addresses the simultaneous, long time observations of the mission. The WFM is a wide field instrument using a coded mask imaging technique, consisting of ten cameras allowing source localization down to 1 arcminute. It is designed for long time observation of transient objects in the X-ray band and is sensitive from 2 keV–50 keV. The WFM operates in large parts in the same energy band as the LAD (2 keV–30 keV) and observes about one third of the whole sky simultaneously. With the WFM it is possible to track the state and provide long term emission history of transient sources. In addition the WFM has a so-called burst alert system, allowing fast identification of GRBs and transmission of their coordinates to the

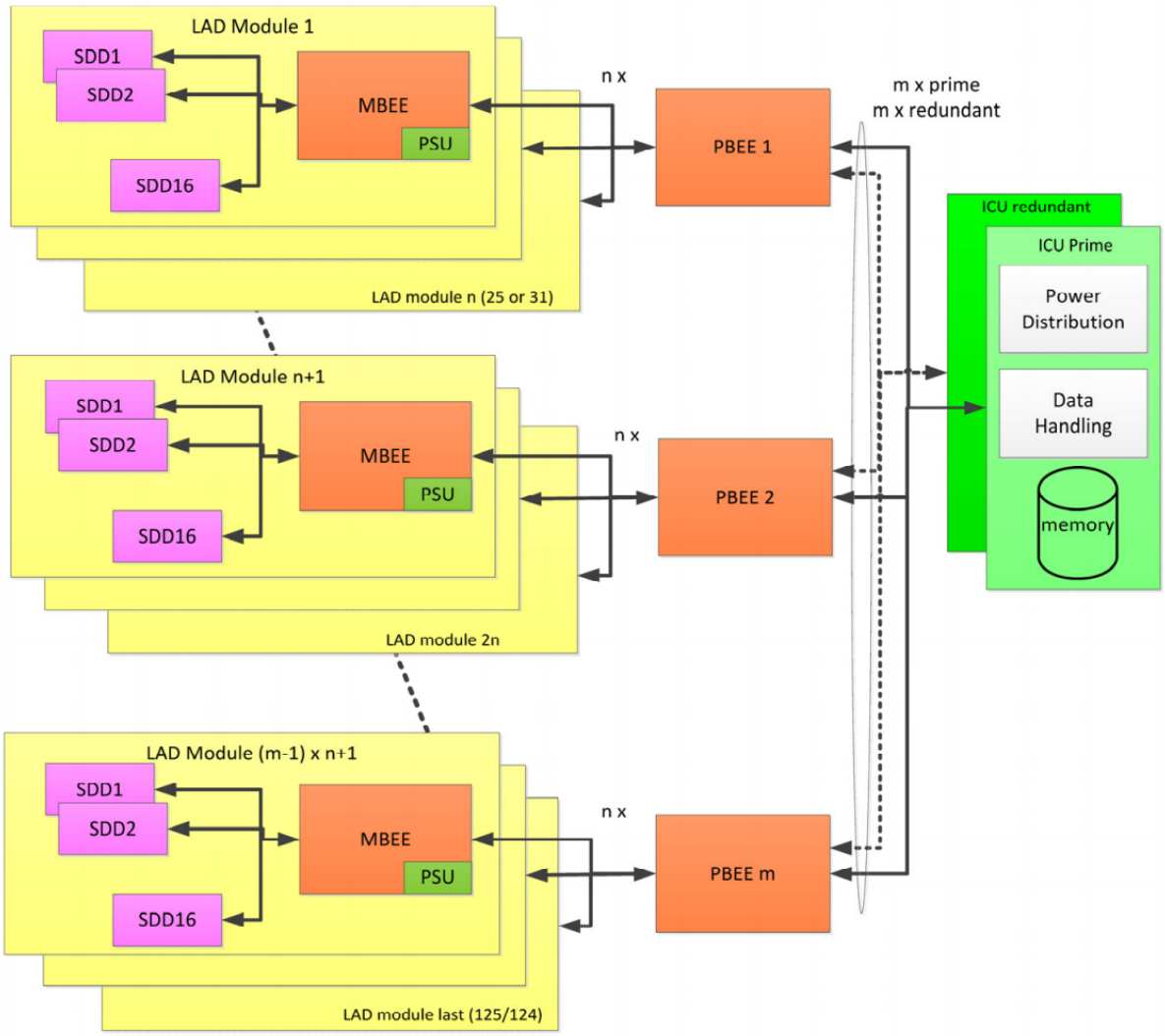


**Figure 2.4:** Hierarchical structure of the LAD electronics. The MBEE of one module handles the FEEs of 16 SDDs as well as the PSU. The PBEE provides the power supply and the clock for the MBEEs and receives their science and housekeeping data in turn. It then processes the data to and receives power from the ICU. The ICU stores the data and transmits it to the ground. Since the ICU is the most important unit there is a redundant ICU. *Image: D. Walton / LOFT Assessment Study Report*

ground within 30 s. The WFM is a well suited addition to the LAD as the LAD is a pointed, collimated instrument with a narrow field of view of 1 armin and no angular resolution, but a large effective area of around 10 $m^2$ at 6 keV, dedicated to observe one source with a high timing resolution of 10 µs. The WFM in contrast uses a coded mask technique yielding an angular resolution of less than 3 arcmin and a large field of view of $1.5\pi$ sr, allowing the monitoring and tracking of the emission state of many transient objects. The task of this diploma thesis is the development of the Back End Electronics (BEE) for the WFM and the WFM is thus discussed in more detail than the LAD, even though it is not LOFT's main instrument. The design of the BEE affects the accuracy of the position reconstruction as well as the time tagging and the data throughput. The BEE is also responsible for the (re)calibration of Front End Electronic (FEE). Section 3 will therefore give a detailed overview of the WFM's design to get a better understanding of the context between the BEE and the WFM in total. It will also discuss the objects observed with the WFM and the coded mask technique, while Section 4 discusses the BEE setup.

# Chapter 3

# The Wide Field Monitor

## 3.1 The observational objects of the WFM

The WFM is designed for long time observations in the 2 keV-50 keV band. The objects of interest are sources with emission rates that strongly vary in time, so-called transient sources or just transients. Transients include a range of sources that have either periodic variations in their emission rate or a singular, heavy outburst. It is the purpose of this section to give an overview over these WFM's objects of interest.

### 3.1.1 Binary systems

The information in this subsection is based on the work of Reig 2011. Binary systems consist of two stars that orbit around their common center of mass. These systems are quite common as nearly half of all stars are in binary or multiple systems. Binaries are called close binaries if mass accretion from one star onto the other star occurs. If one of the stars in a close system is a compact object, then the radiation released by the accretion process can be X-rays or even $\gamma$-radiation. These so-called X-ray binaries (XRB) are divided in subclasses depending on the compact object and its companion star as shown in Figure 3.1. In this diploma thesis the name XRB is only used if the compact object is a black hole or neutron star. For a white dwarf compact object the binary system is called cataclysmic variable.

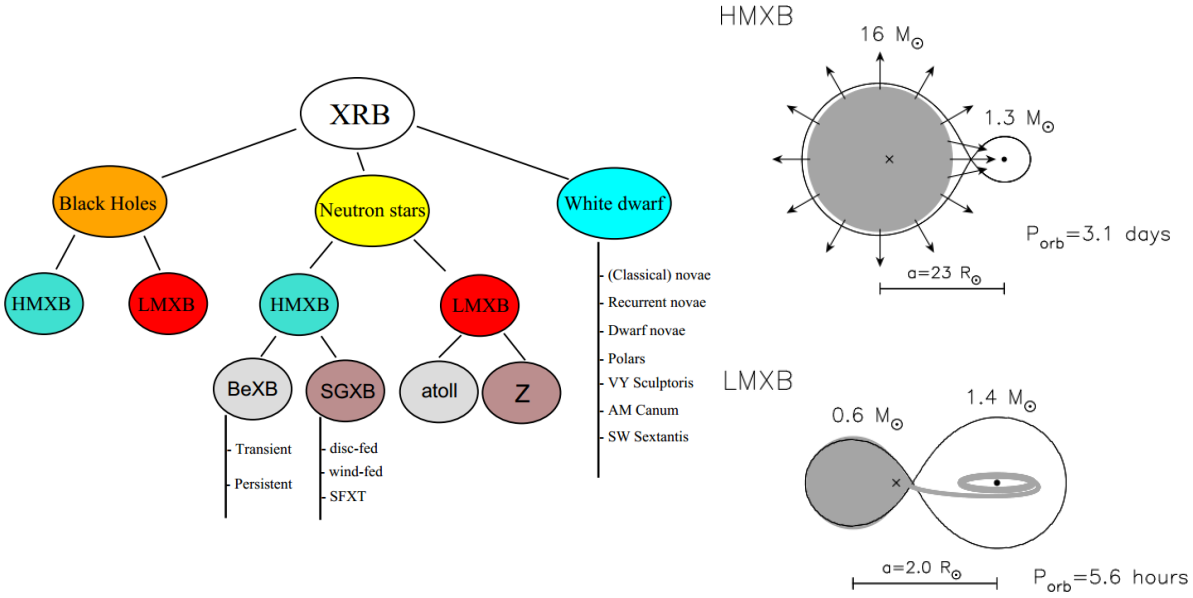


**Figure 3.1:** *Left:* Classifications of XRBs. (Reig 2011) *Right:* Examples of typical HMXB (*top*) and LMXB (*bottom*) geometries. The neutron star in the HMXB is fed by a strong high-velocity stellar wind and/or by beginning atmospheric Roche-lobe overflow. The neutron star in an LMXB is surrounded by an accretion disc which is fed by Roche-lobe overflow. There is also observational evidence for HMXBs and LMXBs harboring black holes. *Image: Tauris and van den Heuvel 2006*

### X-ray binaries

This subsection about X-ray binaries is based on the work of (Chaty 2013; Ivanova 2013; Chaty 2012) Neutron star and black hole XRBs can be subdivided in two different categories depending on the type of companion star:

- Low mass X-ray binaries (LMXB) have a main sequence star or a white dwarf as companion star. Because of their limited brightness, accretion cannot happen by stellar winds but by so-called Roche-lobe overflow. The Roche-lobe is a region around the star in which material is gravitationally bound to the star. In an X-ray binary system the compact object therefore has a strong influence on the Roche-lobe of its companion star. If the companion star fills or extends over its Roche-lobe, material can be transferred to the compact object via the Lagrangian Point L1.
- High mass X-ray binaries (HMXBs) have bright and massive companion stars ($M_{companion} > 4M_{\odot}$). The companion star is usually a main sequence star, a giant or a supergiant. Their X-ray luminosities are in the range of $10^{34}$ erg/s - $10^{38}$ erg/s. These high luminosities result in a high radiation pressure on the outer layers of the star and thus a strong ejection of ionized particles called stellar wind. If now, as in X-ray binaries, a compact object happens to be in the direct neighborhood, parts of the stellar wind are caught in the gravitational potential of the compact object. This stellar wind accretion is the main accretion mechanism for HMXBs.

As mentioned above, X-ray binaries have large variability in luminosity on timescales ranging from milliseconds to years. While one of the intentions for building the LAD is the observation of the accretion of neutron stars and the variation of their spectra and luminosities on short timescales like in pulsars, the purpose of the WFM is the long time monitoring of many transient objects like Be-star X-ray binaries and X-ray bursts and to provide trigger for the LAD in case of an outburst in the activity of an object.

### Pulsars

Pulsars are neutron stars with a misalignment between their rotational axis and their magnetic poles. Pulsars have rapid spins and rotation periods ranging from milliseconds to seconds, which is a leftover of the spin of the former star. This rotation causes the beam emitted at the magnetic poles to sweep over the observer resulting in the characteristic pulsation effect. While Pulsars can also be powered by rotation (Gold 1968), the driving mechanism in binary X-ray pulsars is accretion. Accreting material cannot fall directly on the surface of the neutron star due to conservation of angular momentum so it spirals inwards creating a so-called accretion disc. In the disc gravitational and frictional forces raise the temperature and lead to ionization. At the Alfvén radius the material couples to

the magnetic field lines and finally falls onto the neutron star's surface on the magnetic poles, making them the main site of emission, the so-called *hot spots*. The thermal radiation of the hot spots is scattered to even higher energies by the in-falling electrons via inverse Compton scattering. Other effects that take place are synchrotron emission by interaction of the ionized matter with the magnetic field and bremsstrahlung by internal interaction within the ionized matter.

### Be-star X-ray binaries

Be-star X-ray binaries are HMXBs which consist of a neutron star and a rapidly spinning B star showing emission lines (hence "e" for emission). They show variability in their luminosity on a wide timescale from days to years, indicating that stellar winds play a minor role in the accretion processes. The Be star's fast rotation creates an extended circumstellar disc. As the neutron star passes the periastron of its orbit, it passes near or sometimes even through the Be star's disc. This results in a rapid rise of the accretion rate and therefore in an increase of the binaries brightness (See Fig 3.2). (Paul and Naik 2011)

### Cataclysmic variables

Even though the gravitational potential well of a white dwarf is not as deep as that of a black hole or a neutron star, cataclysmic variables too can be the source of transient phenomena in the X-ray waveband.

One example are novae: Originating from *stella nova*, which is Latin and means *new star*, the word nova was first used to describe the rise of the luminosity in the optical wavelength, making a star visible to the naked eye, which was not visible before. As the physical knowledge about the origins of the change in the luminosity increased over the years, the meaning of the word nova changed and it is now used for an underlying specific physical process and not just for the increasing luminosity for which there are different possible reasons. A nova is created by the white dwarf's accretion in a cataclysmic variable system (Singh 2013). If the accreted matter consists mainly of hydrogen (which is the case for a main sequence or red giant companion star) a small but dense layer on the surface of the white dwarf is created. Since the white dwarf consists of degenerate matter (no particle - particle interaction), the volume does not increase and as additional matter falls in, the temperature rises. When the temperature reaches some $10^8$ K, hydrogen fusion takes place. The helium created by the fusion process of hydrogen cannot undergo another fusion process at first, because the temperature is not high enough. But the fusion of hydrogen increases the temperature further to a point where helium fusion takes place, leading to a so-called runaway process. Due to the large amount of energy set free, remaining gas is blown away leading to a huge rise in the stars luminosity. Unlike

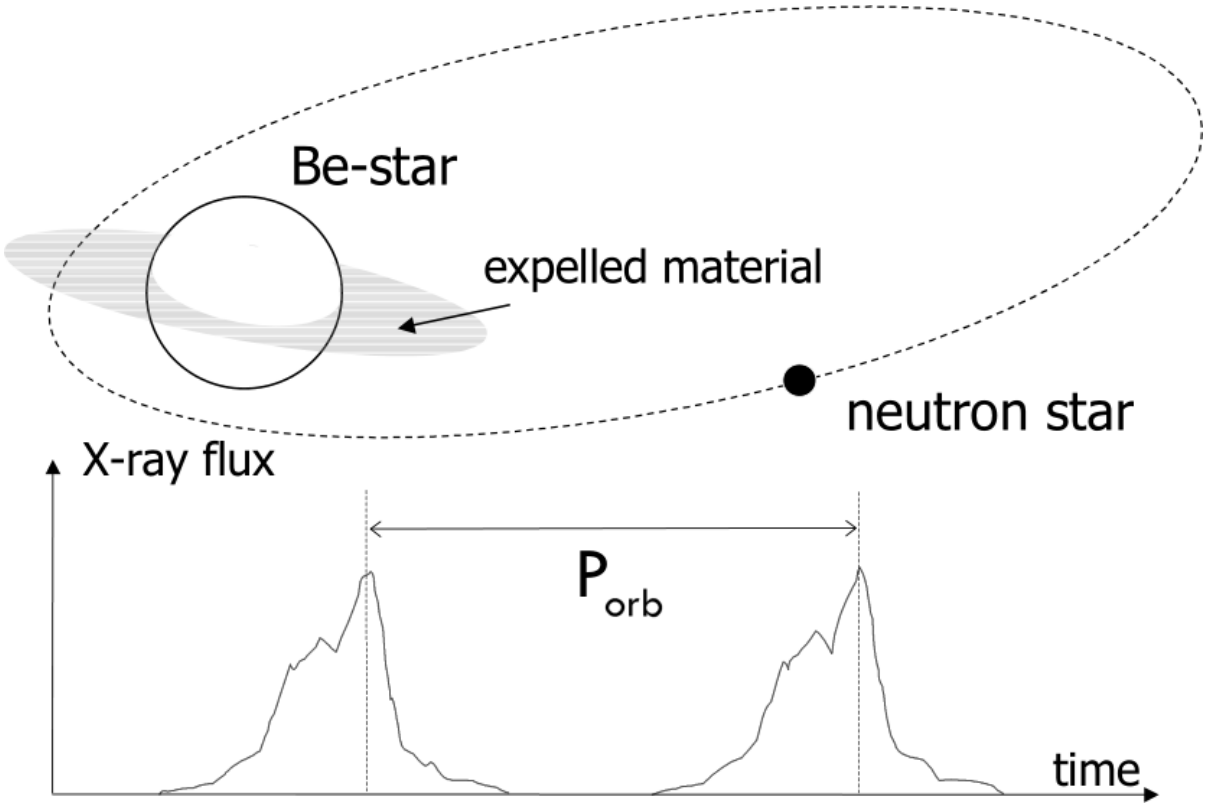


**Figure 3.2:** Schematic model of a Be-star X-ray binary system. The neutron star moves in an eccentric orbit around the Be-star which is not filling its Roche-lobe. However, near the periastron passage the neutron star accretes circumstellar matter, ejected from the rotating Be-star, resulting in an X-ray outburst lasting several days. *Image: Tauris and van den Heuvel 2006*

in supernovae 1a, the white dwarf is not disrupted. Therefore, these events will reoccur, if enough matter has been accreted, with a recurrence time in the order of $10^4$ yr–$10^5$ yr (Hernanz 2013). Some years ago, X-ray emission (Bode et al. 2006; Schwarz et al. 2011) and recently even $\gamma$-ray emission (Hays, Cheung, and Ciprini 2013) were detected in these events. With the WFM's ability to quickly catch those bright novae, a LAD observation of the temperature and density evolution can then be accomplished and shed light in the detailed origins of the high energetic radiation.

Another example for a transient, high energetic event in cataclysmic variables are dwarf nova outbursts. While classical novae result from events on the surface of the white dwarf as discussed above, dwarf nova outbursts result from changes in the accretion disc (Balman 2014). Current models favor a change in the disc's viscosity, when the gas in the disc reaches a critical mass (Lasota 2004; Lasota 2001). This causes a rise in the accretion rate and in the emitted radiation. There are several proposed numerical magnetohydrodynamic accretion flow models and thermal disc instability models, that will be put to test by observations with the WFM and the LAD (Barret et al. 2013).

### 3.1.2 Gamma Ray Bursts

This subsection is based on the work of Seward and Charles 2010, if not stated otherwise. One of the WFM's main targets are Gamma Ray Bursts (GRB). GRBs are sudden flashes of $\gamma$-rays, which were first observed in 1967 by the Vela satellites (Klebesadel, Strong, and Olson 1973). These $\gamma$-ray flashes have two components: The prompt emission with a duration between several milliseconds and hundreds of seconds and the following, slowly decaying emission at longer wavelengths called the afterglow. Their peak energies are in the range of several hundred keV to MeV and their high energy tail may even extend up to GeV. Measurements by the Burst and Transient Source Experiment (BATSE) provided the first distribution of GRBs 25 years after their discovery, which was found to be completely uniform across the sky and which is illustrated in Figure 3.3. Because of their uniform distribution, their origin had to be either extragalactical or in direct surrounding of our solar system. To determine the origin of the source, a counterpart in other wavelength observations had to be located. This was done for the first time with help of the BeppoSAX and the HETE satellite observatories. These instruments were able to detect the bursts, locate them with an accuracy of a few arcminutes and quickly transmit the results to the ground. Thus, other observatories could target the afterglow and identify extragalactical sources as their origin. The observed cosmological distance leads to burst energies which can exceed $10^{53} \frac{\Omega}{4\pi}$erg, where $\Omega$ is the opening angle of emission, making GRBs the most luminous events in the universe (Gehrels, Ramirez-Ruiz, and Fox 2009). Currently there are two controversial models describing the GRB's prompt emission.

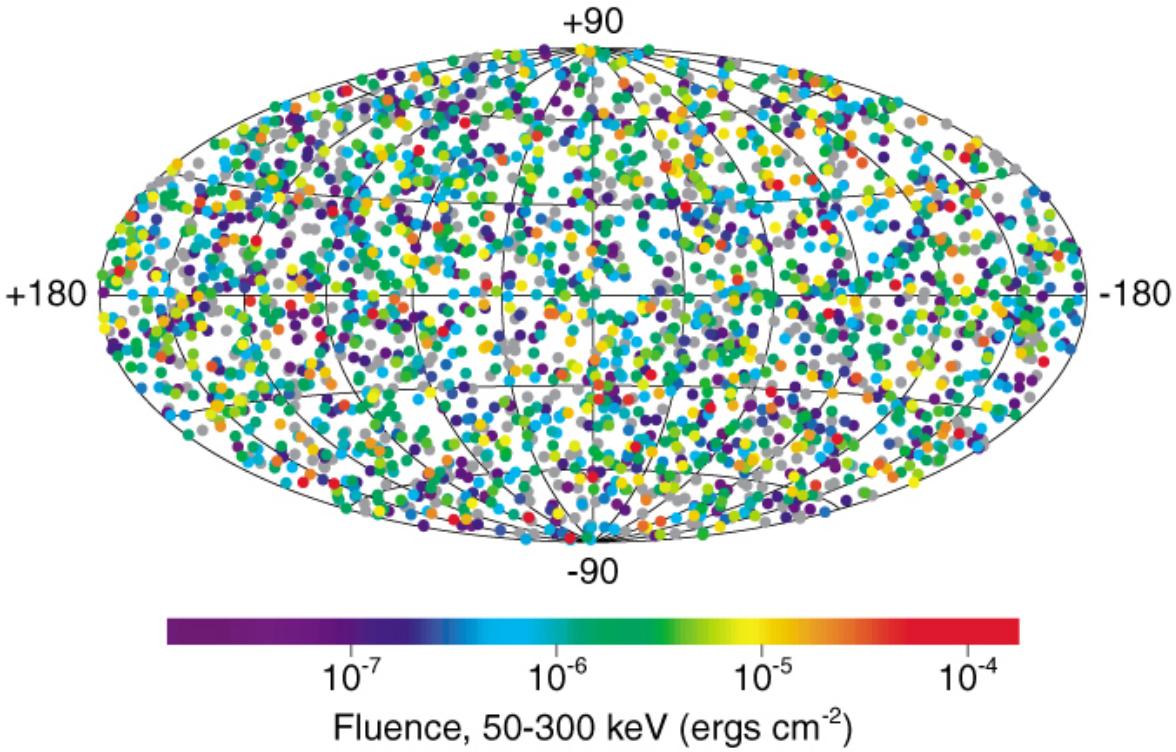


**Figure 3.3:** Distribution of 2704 GRBs recorded by BATSE of the CGRO satellite in galactic coordinates. The color code of the GRB distribution shows the GRB's flux integrated over the GRB's duration. Strong GRBs with a long duration are red, while weak, short GRBs are purple. The distribution appears to be completely uniform across the sky. Since the Milky Way has a disc structure, this could either be realized if GRBs were a common phenomenon occurring frequently throughout our whole galaxy or if the origin of the GRBs was extragalactical. The latter was confirmed by the ground observations of the afterglow, identifying the GRBs with extragalactical sources. These observations were following-up the detection of GRBs by observatories like BeppoSAX, HETE and recently by Swift. Swift is a NASA mission, dedicated to the study of GRBs and was launched in 2004. The mission consists of a satellite with three different instruments: The Burst Alert Telescope, the X-ray Telescope and the Ultraviolet/Optical Telescope. With these instruments Swift is able to detect GRBs as well as to observe their afterglows. Until today, July 14, 2014, Swift has observed a total of 891 GRBs. *(Source and image: NASA)*

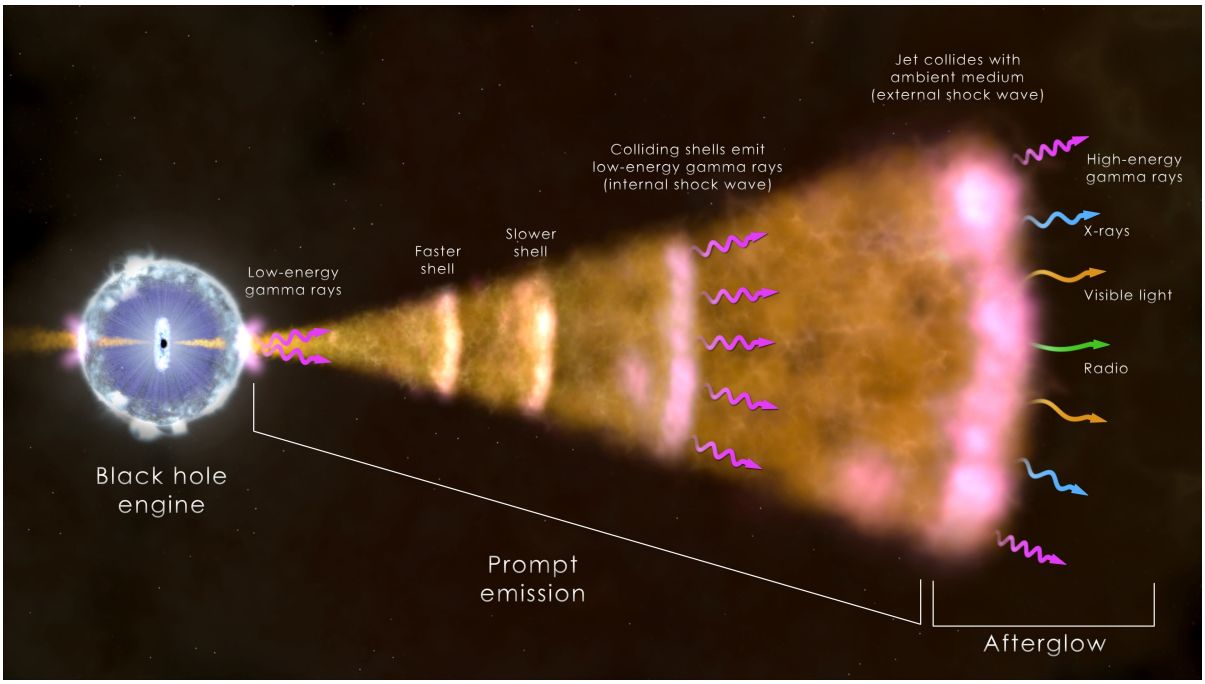


**Figure 3.4:** Schematic illustration of the GRB process. *Left:* Initial engine of the GRB. This can either be the merging of any combination of neutron stars and black holes or a star's collapse into a black hole. *Middle:* Ejected material builds a fireball with shells moving at different velocities. The collision of these shells creates the internal shocks and the prompt emission. At this point velocities are still relativistic and the emission is focused by relativistic beaming. *Right:* The fireball is decelerated below relativistic velocities by interaction with the surrounding interstellar medium and remaining material of the supernova, creating the afterglow. *(Image: NASA)*

### Fireball model

The fireball model describes the GRB's energy mainly as thermal energy released by the initial event. A fireball is then ejected due to expansion under its own thermal pressure and most of its thermal energy is converted to kinetic energy (Shemi and Piran 1990). These fireballs have low baryon and high photon densities so that after a short initial acceleration, they reach relativistic velocities. The fireball itself has shells moving at different velocities resulting in so-called internal shocks. The interaction of the different shells produces $\gamma$-radiation through inverse Compton scattering and synchrotron emission. When the fireball becomes optical thin due to expansion, $\gamma$-radiation can escape resulting in the prompt emission. As a result of the high velocities, relativistic beaming takes place and the radiation is strongly focused in the moving direction. As the fireball propagates outwards, it becomes decelerated by the interstellar medium creating a forward and a reverse shock. While the reverse shock can produce a bright optical flash, the so-called external shock in forward direction creates the afterglow by interaction with the interstellar medium. A schematic illustration of this process is found in Figure 3.4.

### Electromagnetic model

In the electromagnetic model, rotational energy of the central engine is transformed into magnetic energy. Particles in the emitting region of the GRB are then accelerated by strongly magnetized winds. According to Lyutikov and Blandford 2003, the jets are focused by hoop stress of the magnetic field. In contrast to the fireball model, no shocks are necessary because the bulk energy is carried subsonically by the magnetic field (Lyutikov 2006).

Several more specific theories have been developed over the years, which combine the electromagnetic and the fireball model. Some of these theoretical models favored in recent publications are listed here for reasons of completeness:

- Fireball internal model (Mészáros and Rees 2000; Kumar and Narayan 2009)
- Magnetized engine - internal shock model (Bošnjak, Daigne, and Dubus 2009; Daigne, Bošnjak, and Dubus 2011)
- Dissipative photosphere model (Giannios 2008; Veres and Mészáros 2012)
- Internal collision-induced magnetic reconnection and turbulence model (Zhang and Yan 2011)
- Magnetic reconnection switch model (McKinney and Uzdensky 2012)
- Current instability model (Lyutikov and Blandford 2003)

Since these models all make different predictions on the GRB's prompt emission, its spectral shape and the hard to soft evolution, the WFM of LOFT will be useful to constrain these models by performing measurements in the 2 keV - 50 keV band.

### Classification of GRBs

Even though the exact mechanism of GRBs is still unknown, they can be classified in two classes mainly depending on their duration, which is defined as the time during which 50% ($T_{50}$) or 90% ($T_{90}$) of the counts above background are measured (Gehrels, Ramirez-Ruiz, and Fox 2009; Kouveliotou et al. 1993):

### Long GRBs

These events have a duration greater than two seconds and are the most common GRB class, with a contribution of about 75% of all observed GRBs (Kouveliotou et al. 1993). The observation of highly red shifted galaxies as host galaxies of long GRBs and their identification with supernovae counterparts associated long GRBs with starforming regions of distant galaxies (Hjorth et al. 2003; Pian et al. 2006; Galama et al. 1998). Therefore long GRBs are most likely the result of the collapse of a massive rotating star into a compact object (Woosley and Bloom 2006).

### Short GRBs

Short GRBs have a duration of less than two seconds and contribute to about 25% of all observed GRBs. They originate from older star populations and thus exclude massive stars (also no supernova counterpart could be observed). Most likely they are the result of the merging of two compact objects (NS-NS, NS-BH or BH-BH) (Narayan, Paczynski, and Piran 1992). During the merging process there is a shortlived massive increase of the accretion rate and therefore a burst in the emission of photons, creating the GRB. Short GRBs have harder spectra and have been detected at lower redshifts than long GRBs. Since short GRBs have much lower energies than long GRBs, this might limit their detectability beyond redshifts at $Z = 1$.

### X-ray flashes

According to Pélangeon et al. 2008 these events have lower peak energies and their flux is dominant in the X-ray band and lower for $\gamma$-emission. Their afterglow, distribution and duration are similar to those of classical GRBs. Since there also seems to be a continuum in the peak energies between X-ray flashes and classical GRBs, these phenomena seem to

be closely related (Sakamoto et al. 2008). One possible explanation is that X-ray flashes are long GRBs observed slightly off the beaming axis, making the observed spectra softer. Another possibility is a fireball model with a higher fraction of baryonic matter, the so-called "dirty fireball model". A higher content of baryonic matter makes the accelerated matter slower and therefore the spectrum softer. With a proposed detection rate of about 40 – 50 per year the WFM of LOFT will provide further insights in the nature of this GRB subclass.

## 3.2 Scientific Requirements

Several requirements have to be fulfilled to achieve the proposed scientific goals. These requirements are calculated based on the statistics needed to state the achievement of the proposed goals and the available statistics for transient events, which are based on the RXTE observations. These statistics for transient events determine the mission duration. Three elements have to be taken into account for this determination:

- The overall observing time
- The accessibility of the required sources
- The probability for a transient source to be active during the mission

The driving point for the duration of the LOFT mission are the transient observations necessary for the LAD's scientific goals. To achieve the goals, at least 3 outbursts of transient black holes and at least 3 outbursts of accreting millisecond X-ray pulsars have to be observed. For an observing probability of >95% a mission duration of 3 years is required (Barret et al. 2013). The scientific requirements for the WFM are determined by the Burst Alert System, the accessibility for monitoring of transient sources and the necessity to provide good triggers of active sources for the LAD. The elements that need to be taken into account are:

- The sky accessibility and field of view
- Sensitivity
- Location accuracy
- Telemetry rate, available bandwidth and onboard memory
- Energy range and number of energy bands
- Rate triggering for GRBs

**Table 3.1:** Comparison of the technical data of the LOFT WFM, the Rossi X-ray Timing Explorer's All Sky Monitor (RXTE ASM) (Levine et al. 1996) and the Swift Gamma-Ray Burst Mission's Burst Alert Telescope (SWIFT BAT) (Barthelmy et al. 2005)

| Item | LOFT WFM | RXTE ASM | SWIFT BAT |
|---|---|---|---|
| Energy range | 2 keV–80 keV | 1.5 keV–12 keV | 15 keV–50 keV |
| Energy resolution | 300 eV FWHM at 6 keV | | ~7 keV |
| Time resolution | 150 s per image | 80% of the sky every 90 minutes | 64 sec |
| Spatial resolution | <3 arcmin | 3 arcmin x 15 arcmin | 4 arcmin |
| Field of view | 4.1 sr | $3 \times 6° \times 90° \approx 0.5$ sr | 1.4 sr |
| Effective area | 170 $cm^2$ | 69 $cm^2$ at 10 keV | 5200 $cm^2$ |
| Detector | 10 coded mask cameras, 40 Silicon Drift Detectors | 3 scanning shadow cameras, position-sensitive Xenon proportional counter | Coded mask instrument with 256 modules of 128 elements/module, made of CdZnTe |
| Sensitivity | 3 mCrab (5 σ, 50 ks) | 30 mCrab | 5.3 mCrab |
| GRB detection rate | >100 GRBs $yr^{-1}$ | | >100 GRBs $yr^{-1}$ |

These requirements set the technical standard for the LOFT hardware. A complete overview of the WFM's requirements and its envisaged goals are listed in Table 3.2. The WFM's attributes are compared to the ASM instrument of the past mission RXTE and to the current Swift mission's BAT in Table 3.1.

## 3.3 The design of the WFM

A crucial point for the WFM set by the scientific requirements is its wide field of view. This is realized by ten cameras combined in pairs. The cameras of each pair are orthogonal, since the detectors provide different accuracy to measure the event position on the detector plane in vertical and horizontal direction. This way the position measurement accuracy is optimized by a combination of the pictures of both cameras. A WFM image created by the overlay of the observations of two cameras can be seen in Figure 3.7 and Figure 3.8. Each camera pair provides a field of view of 91.7° x 91.7°. The pairs are arranged at different angles to cover a large fraction of the sky, while the direction blocked by the sunshield is left bare (see Figure 3.5). The reason for the sunshield is the limiting maximum temperature difference of 10 °C for the coded mask due to its thermal expansion. Within these 10 °C it is still possible to reconstruct the sources regarding the pursued error limits. The anticipated field of view covers 4.1 sr at 20% of the peak camera response. The WFM field of view is illustrated in Figure 3.6.

**Table 3.2:** List of the requirements and the planned performance of the WFM

| Item | Requirement | Goal |
|---|---|---|
| Location accuracy (confidence level 90%) | <1 arcmin | <0.5 arcmin |
| Angular resolution | <5 arcmin | <3 arcmin |
| Peak sensitivity in LAD pointing direction ($5\,\sigma$ source detection) | 1 Crab (1 s)<br>5 mCrab (50 ks) | 0.2 Crab (1 s)<br>2 mCrab (50 ks) |
| Absolute flux calibration accuracy | 20% | 15% |
| Relative flux calibration precision | 5% | 2,5% |
| Sensitivity variations knowledge | 10% | 5% |
| Duration for rate triggers | 0.1 s –100 s | 1 ms–100 s |
| Rate meter data | 16 ms | 8 ms |
| Field of view | $\pi$ sr around the LAD pointing | $1.5\pi$ sr for large Sun angles part of the LAD accessible sky would otherwise not be monitored |
| Energy range | 2 keV–50 keV primary<br>50 keV–80 keV extended | 1.5 keV–50 keV primary<br>50 keV – 80 keV extended |
| Energy resolution | 500 eV | 300 eV |
| Energy scale calibration accuracy | 4% | 1% |
| Number of energy bands for compressed images | $\geq 8$ | $\geq 16$ |
| Time resolution | 300 s for images<br>10 µs for event data | 150 s for images<br>5 µs for event data |
| Absolute time calibration accuracy | 2 µs | 1 µs |
| Event/image data downlink maximum delay | 3 h | 1.5 h |
| Onboard storage of triggered date | 3 h | 2 h |
| Broadcast of trigger time and position to end user | < 30 s after on board detection of the event for 65% of the events | < 20 s |
| Number of triggers for WFM | » 1 per day | » 1 per orbit |
| Modularity | No full loss of FoV due to single point failure | |
| On-board memory | 5 min at 100 Crab | 10 min at 100 Crab |

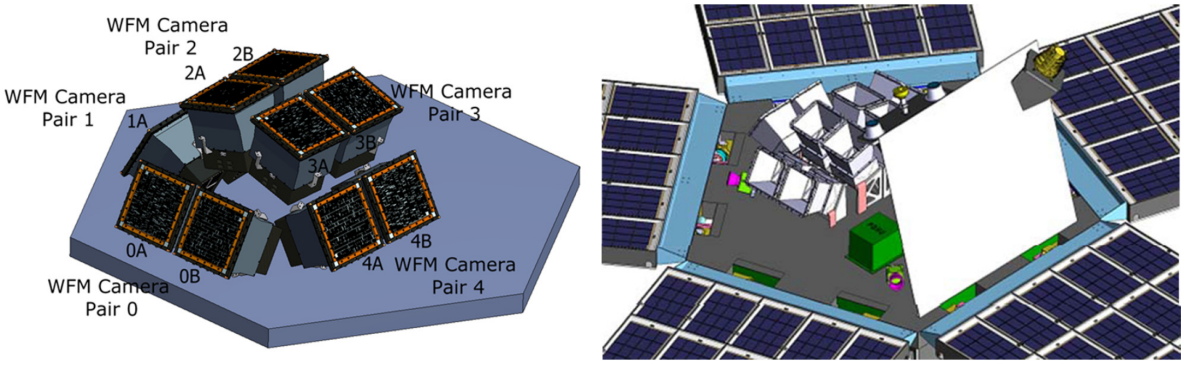


**Figure 3.5:** *Left:* Alignment of the WFM cameras. There are five pairs, each adjusted at a different angle to cover a large fraction of the sky. In a pair each camera is rotated by 90 degree relative to the other camera. This is due to the fact that the horizontal resolution of the camera is better than the vertical resolution. Therefore, providing sufficient statistics, a combination of the pictures of both cameras yields a better resolution than they would have without rotation. The fact that there is no pair pointing in the upper right direction in the figure is because this direction will be blocked by the sun shield. *Right:* Possible realization of the WFM in the five panel solution of LOFT. The upright white plane aligning to the panel on the lower right hand side of the figure is the sunshield. *Image: D. Karelin / LOFT Assessment Study Report*

Each camera consists of 4 Silicon Drift Detectors (SDD), while each SDD is subdivided in two detector halves. Each detector half is read out by 7 application-specific integrated circuits (ASICs). This SDD subdivision is important for the electronic design and is described in detail in Section 3.4.

Figure 3.9 shows the composition of a WFM camera. The top component is a coded mask, which is required for position measurements with the WFM. An explanation of its working mechanism is given in Section 3.5. Below the coded mask is the collimator. It shields the detector plane from background radiation. While the collimator itself is made of 3 mm thick carbon-fiber-reinforced plastic, it is coated with a 150 µm thin film of Tungsten to shield the detector from the diffuse X-ray background of the sky. Thin layers of Mo and/or Cu may also be introduced to allow an on-board calibration of the detector by fluorescence lines avoiding the mounting of a radioactive source. (Brandt et al. 2012) Because of the large opening angle of the instrument, the detector has to be shielded from the impact of micro-meteorites. This is achieved by placing a Beryllium layer of 25 µm thickness approximately 8 mm above the detector plane. (Gálvez et al. 2013) The plane will act as a so-called Whipple Shield, smashing larger particles that penetrate the layer into a cascade of smaller particles, thus robbing the impact particle of the energy used to penetrate the layer and distributing its remaining energy on the area covered by the secondary particle shower. This reduces the damage to the detector and ensures its performance over a longer mission lifetime.

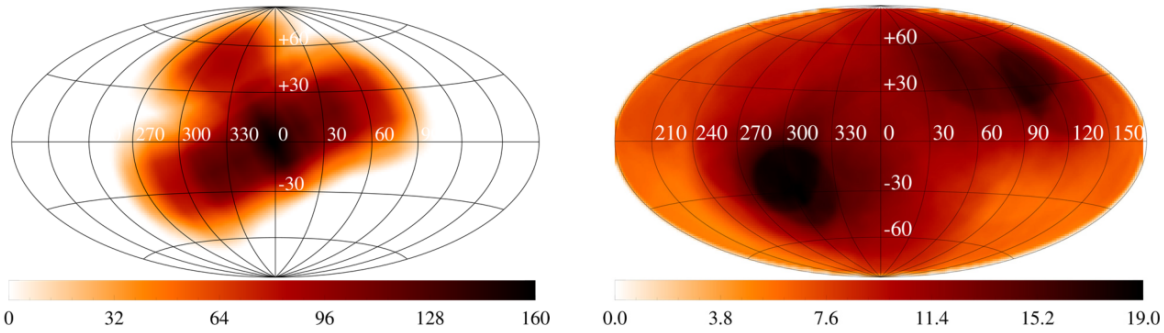


**Figure 3.6:** *Left:* Exposure map in galactic coordinates for a measurement directed towards the galactic center. The color coded scale represents the active detector area in $cm^2$.
*Right:* Exposure map in galactic coordinates after a 1 yr measurement. Only positions that covered at least 10 $cm^2$ of the detector area were counted. Color coded scale is the exposure time in Ms. *Image: Barret et al. 2013*

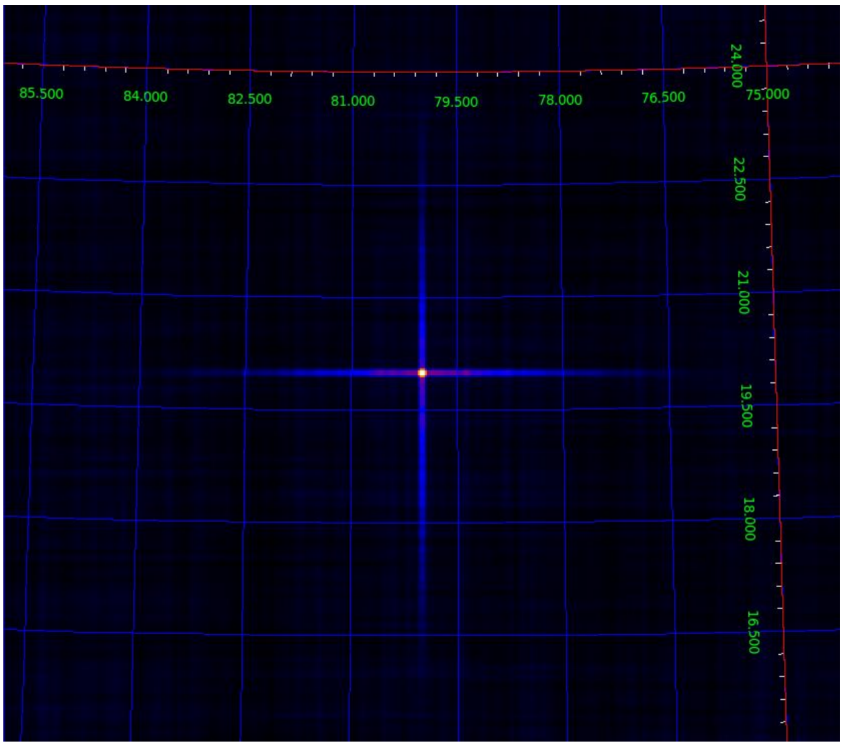


**Figure 3.7:** Image of an isolated source as acquired from the WFM. The image was created by the overlay of the images of two different cameras rotated by 90° and the cross structure is a result of the different accuracy of the camera in horizontal and vertical direction. *Image: LOFT Design Description*


**Figure 3.8:** Simulated observation of the galactic center with an exposure time of 10 ks. The overlay of the rotated cameras' images causes the stripe structure of the resulting image. *Image: LOFT Design Description*

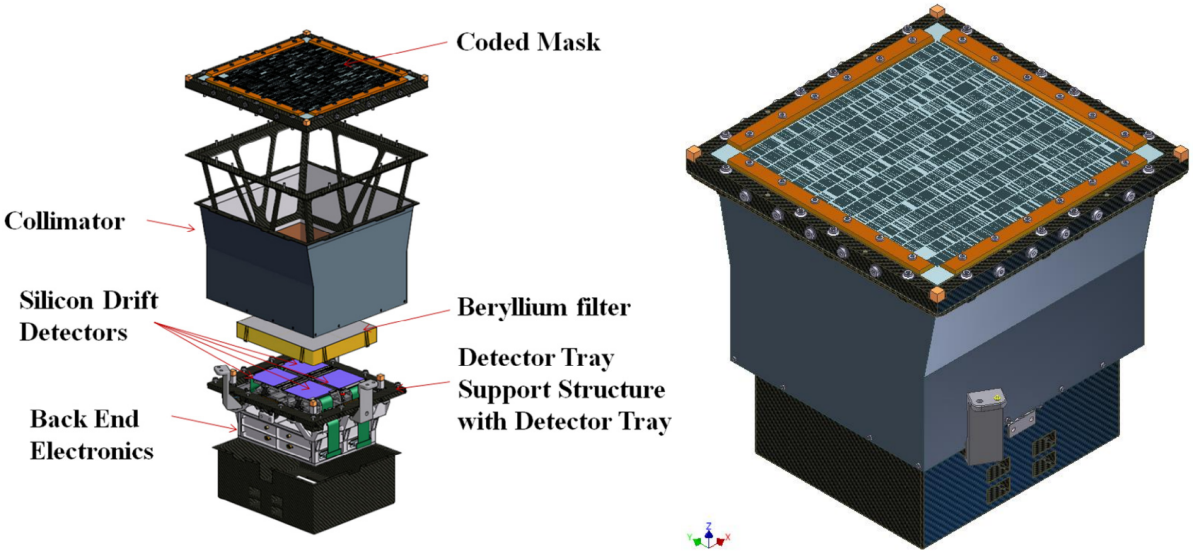


**Figure 3.9:** *Left:* Schematical composition of a WFM camera. *Right:* A WFM camera illustration.
*Image: D. Karelin / LOFT Assessment Study Report*

The 4 SDDs and the corresponding Front End Electronics (FEE) of each camera are held in place by the Titanium detector tray. The detector tray also has a mechanism allowing to control the alignment of each SDD/FEE pair in height, tilt and twist direction. Below the detector tray are the Back End Electronics (BEE) and the Power Supply Unit (PSU). The BEE as the topic of this thesis is described in Chapter 4. The camera is passively cooled from the backside by a radiator.

## 3.4 The Silicon Drift Detector

The detectors used for the WFM cameras and the LAD are SDDs, that are based on the SDDs used in the Inner Tracking System of the ALICE experiment at CERN. (Gatti and Rehak 1983; Rashevsky et al. 2002) The advantages of SDDs are their possible large photon collecting area, their low weight of around $1\,\mathrm{kg\,m^{-2}}$ and their low noise readout anodes. The SDDs used in LOFT were composed of a 450 µm thick neutron transmutation doped n-type silicon wafer, with a $SiO_2$ layer containing a series of parallel cathodes on both sides. The left hand side of Figure 3.10 illustrates this setup. These cathodes are kept at different electrical potentials to completely deplete the silicon layer as well as to form an electric field parallel to the silicon wafer. The potential has a maximum at the cathode in the middle of the layer, while the readout anodes are kept at minimum potential. Since the SDDs used in LOFT have a width of 70 mm with readout anodes on either of the two sides, the potential maximum is at a distance of 35 mm from the readout anodes which is also the maximal drift distance for the charges created by an incident photon. In case of LOFT this potential difference or so-called drift voltage is 1300 V. Heavily p-doped cathodes are used to create a block-voltage at the p-n injunction that keeps the charges focused in the vertical middle of the plane. Vice versa the anodes are heavily n-doped to favor the acception of electrons.

The functionality of the SDD is as follows: If an incident X-ray photon is absorbed in the Si layer via the photoelectric effect, it initially creates one single electron-hole pair. Since the electron has all of the photon's energy, it quickly creates a charge cloud through impact ionization. This cloud is accelerated towards the anodes by the drift voltage. As the charge cloud propagates towards the anodes, it broadens by the repulsion between the electrons and by diffusion. Finally the signal charge is collected at the anodes and integrated on the feedback capacitance of the charge sensitive amplifier inside the ASIC. This situation is illustrated on the right hand side of Figure 3.10. The figure also illustrates the necessity of this subdivision. Since the cathode in the middle of the SDD is at maximum potential, the events on the top half of the SDD's sensitive area create a charge cloud moving towards the top anodes while an event below the middle creates a charged cloud moving towards the bottom anodes. The top half and the bottom half of the SDD are independently handled by seven ASICs each. If one detector half registers

an event and starts communicating with the BEE (see Section 4.2), the other half can still detect further events.
Up to this point, the working principle of the SDDs for the LAD and the WFM are the same. However they differ in the number of anodes for each SDD. This is due to the different tasks of the instruments. The LAD is a non imaging instrument, so the energy resolution is the important property of the detector. The WFM's purpose instead is the tracking of the state of a source distribution in the sky, so spatial resolution as well as energy resolution are important. Because energy resolution and spatial resolution cannot be optimized at the same time, this leads to a different SDD setup for both instruments. For a better spatial resolution more anodes are needed, while at the same time this worsens the energy resolution, because the noise of each anode contributes to the total noise of the signal. To optimize the energy resolution of the LAD, a number of $2 \times 116$ anodes per SDD with a pitch of 970 µm was selected, resulting in an energy resolution of 180 eV–240 eV FWHM at 6 keV. For the WFM a number of $2 \times 448$ anodes per SDD with a pitch of 145 µm was selected, yielding an energy resolution of 300 eV FWHM at 6 keV. The position reconstruction of the event on the SDD is treated in detail for the WFM in Section 4, while Section 3.5 treats the technique used to deduce the position of a star in the sky from the position where the incident photon was absorbed in the detector plane.

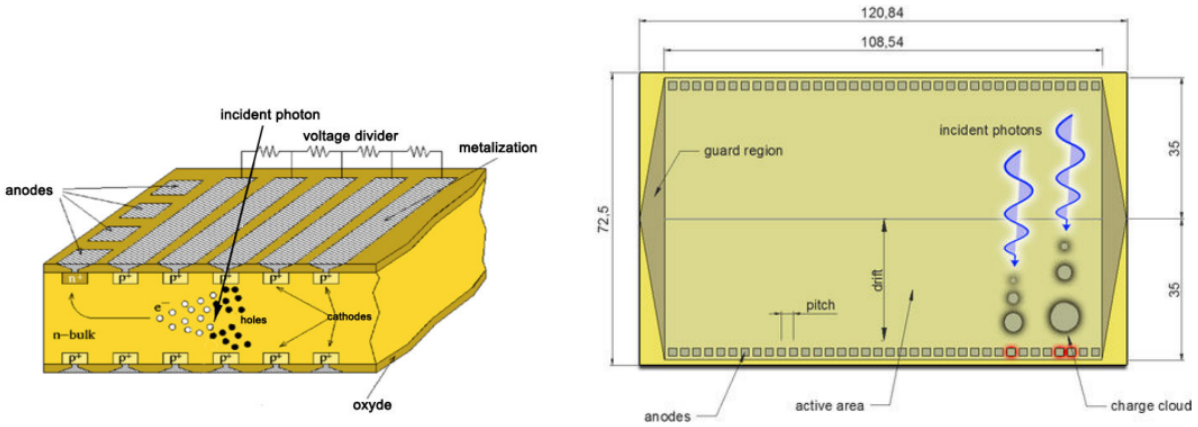


**Figure 3.10:** *Left:* An incident photon is absorbed in the detector and creates a charge cloud. The electrons are accelerated towards the anodes in the electric field created by the voltage dividers. The charge induced in the anodes by the moving charge cloud is then detected.
*Right:* Top view on the SDD. In this image it can be seen, that the charge cloud broadens due to the self repulsion of its electrons and diffusion. Note that this illustration was created for the LAD and due to the smaller anode pitch in the WFM up to eight anodes can be affected by the charge cloud. *Image: Rashevsky et al. 2002*

## 3.5 Coded mask

The imaging technique used for the WFM is called coded mask imaging or coded aperture imaging. The idea of this technique is to have a pattern mask at a fixed distance from the detector, so that incident light of a star will cast a shadow on the detector plane as illustrated on the left hand side of Figure 3.11. The angle of the star at the sky is then reconstructed from the position of the shadow on the plane. The pattern mask itself is opaque, but has transparent spots. Since this technique is used for observations in the keV regime or in the case of the WFM for energies of 2 keV–50 keV, the material used is usually Tungsten to avoid fluorescence lines from lead. The mask used for the WFM has a size of 280 mm × 280 mm with a coded area of 260 mm × 260 mm and a thickness of 150 µm. The individual elements of the mask have a size of 250 µm × 16 mm, resembling the different spatial resolution of the SDD in anode and drift direction and consist of 75% full elements and 25% holes, i.e. the mask has an open area of 25%. For the position reconstruction of sources in the sky from the position of their shadows on the detector plane a cross-correlation technique is used. This technique is based on the Cross-Correlation-Function (CCF)

$$\mathrm{CCF}(\alpha, \delta) = \iint_{\forall x,y} D(x, y) M(\alpha, \delta, x, y) dx\, dy$$

which correlates the shadow pattern $M(\alpha, \delta, x, y)$ of a simulated source on position $\alpha$, $\delta$ in the sky with the actually measured shadow pattern $D(x, y)$ at the x,y-coordinate of the detector plane. The function $D(x, y)$ is the event distribution as measured by the detector or, in other words, a two dimensional histogram of the detected incident photons on the detector plane. The multiplication of $D(x, y)$ and $M(\alpha, \delta, x, y)$ for certain values $\alpha$ and $\delta$ integrated over the detector plane yields the likelihood for the direction $\alpha, \delta$ at the sky.

## 3.6 Electronic Design

The WFM's electronic setup consists of a chain of different electronic modules in order to perform the distinct tasks of amplification, signal shaping, signal correction and data transmission of the SDD data. It is illustrated by Figure 3.13. The first component is called the Front End Electronics (FEE). The FEE reads out one SDD, communicates with the BEE and consists of 14 ASICs, that are subdivided in two groups, each handling one side of the SDD. Each SDD has 896 readout anodes and groups of 64 of these anodes are handled by one of the fourteen ASICs. When an incident photon interacts with the silicon layer of the detector plane, an electric current is induced on the readout anodes as described in Section 3.4. If the current on one or more anodes exceeds a certain value, the ASIC triggers an event. The ASIC then communicates with the BEE, which tests if the

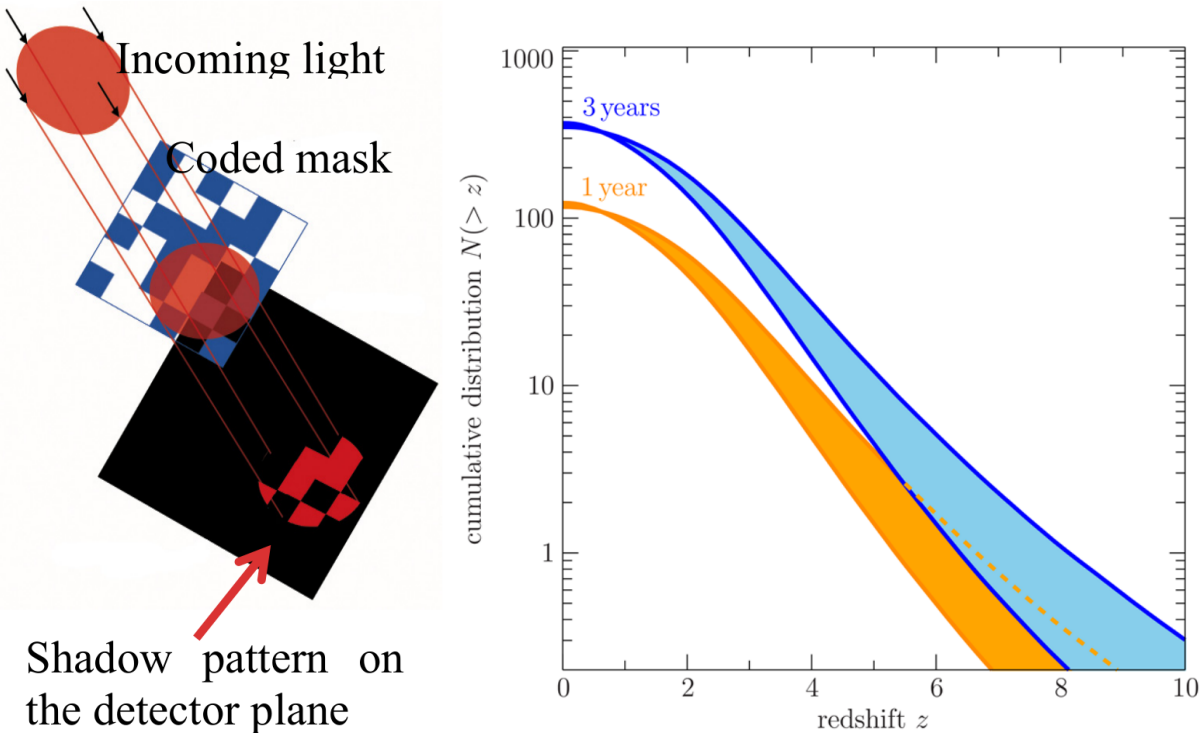


**Figure 3.11:** *Left:* Illustration of the coded mask imaging working principle. Incident light from a source in the sky passes through the coded mask and casts a shadow on the detector plane. The position of the source can then be reconstructed by using a CCF or FFTs. *Source: B.J. Mattson, L3/NASA/GSFC*
*Right:* GRB detections as predicted for the LBAS. The orange curve represents the predictions in GRB detection after a mission duration of one year, while the blue curve represents the number of detections after three years. *Image: A. Watts / LOFT Assessment Study Report*

**Table 3.3:** Hierarchic illustration of the components of the electronic design of the WFM

| Unit | Total number in WFM | Controlled units | |
|---|---|---|---|
| DHU | 2 | 10 | Cameras/BEEs |
| Camera | 10 | 4 | SDDs/FEEs |
| SDD/FEE | 40 | 14 | ASICs |
| ASIC | 560 | 64 | Anodes |

event was valid. If that is the case, the ASIC transmits the digitized data of all anodes to the BEE and resets the anodes. Otherwise the event data is discarded and anode values are reset. In any case, the anode values are reset afterwards. The BEEs main task is to create a time tag and apply a number of different corrections to the event data and to reconstruct the position of the photon's interaction on the detector plane. To achieve this goal, certain different working modes are provided, which allow the comparison of the raw data and the processed data as well as the recalibration of individual parameters. The BEE also keeps track of the detector temperature and handles the Power Supply Unit (PSU). The BEE's functionality is topic of this diploma thesis and a detailed description is given in Chapter 4. The BEE's data is then transmitted to the Data Handling Unit (DHU) via a SpaceWire link. There are two DHUs included in the WFM, while one is redundant. The DHU handles all ten BEEs, distributes the power and stores the data until a link to the ground can be established. It also integrates the events on the detector plane to images in 8 different energy bands over a time interval of T = 300 s, even though with the WFM's energy resolution of 300 eV at 6 keV this results in a loss of information. This is a result of the restricting average downlink speed, which is limited to <100 kbit/s and prevents the transmission of each event separately. The position reconstruction of the source via the CCF (see Section 3.5) will be performed on ground. One orbit of LOFT will take approximately 100 minutes with a contact duration to the ground stations in Kourou and Malindi of about 20 minutes. During these 20 minutes calibration data can be updated by the ground station with an upload speed of 64 kbps and a total of 6.7 Gbit of science and housekeeping data can be transmitted to the ground. However this data volume is for LOFT in total and the WFM data contributes only ~10% of the data bandwidth. The only exception from this communication concept is the LOFT Burst Alert System (LBAS), for which the data is transmitted separately. Figure 3.12 shows a map of the ground stations used for telemetry.

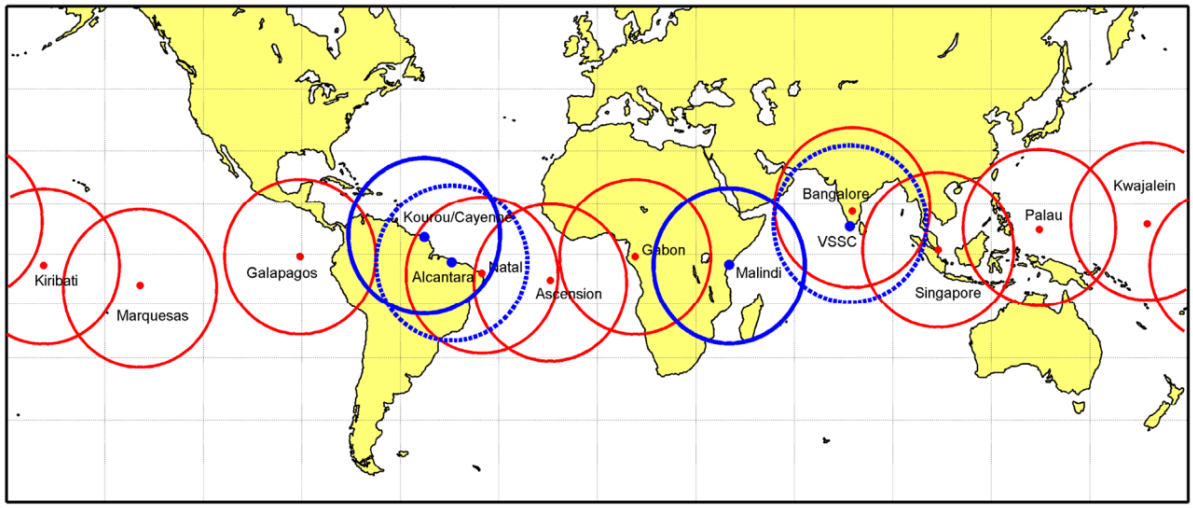


**Figure 3.12:** This figure shows LOFT's ground stations for telemetry. The blue circled stations in Kourou and Malindi are used for the regular telemetry for the LAD and the WFM including the transmission of science data, housekeeping data and configuration data. The red circled stations are part of the SVOM network and would provide a low bandwidth contact to LOFT during the complete orbit. It is used for the transmission of the event data of GRBs. *Image: D. Goetz / LOFT Assessment Study Report*

## 3.7 The LOFT Burst Alert System

The LBAS is designed for fast identification of GRBs and the transmission of the corresponding event data to the ground in less than 30 s. This is important since it is not possible to predict when and where a GRB will occur and a GRB's emission is fading quickly (see Section 3.1.2). Therefore follow-up measurements with other observatories have to be performed as soon as possible. For this reason the position reconstruction of the source is in the case of GRBs performed directly on-board, which would however be too resource intensive for the regular observations. Instead of calculating the CCF directly, a Fast Fourier Transformation (FFT) algorithm is used. (Brandt 2012) Three FFTs are needed to achieve a cross correlation:

$$S = FFT^{-1}(FFT(D) \times FFT(M)^*)$$

FFT(M) is the transformation of the mask, which can already be calculated in advance. Thus only the FFT of the shadow pattern on the detector plane and one inverse FFT are left. Even though this is still hardware intensive, it is somewhat simplified by special hardware primitives on the FPGA, that are designed for FFT. The LBAS then uses a system of VHF receivers that are positioned along the equatorial regions of the Earth and are accessible during LOFT's complete orbit. The expected data rate of the VHF

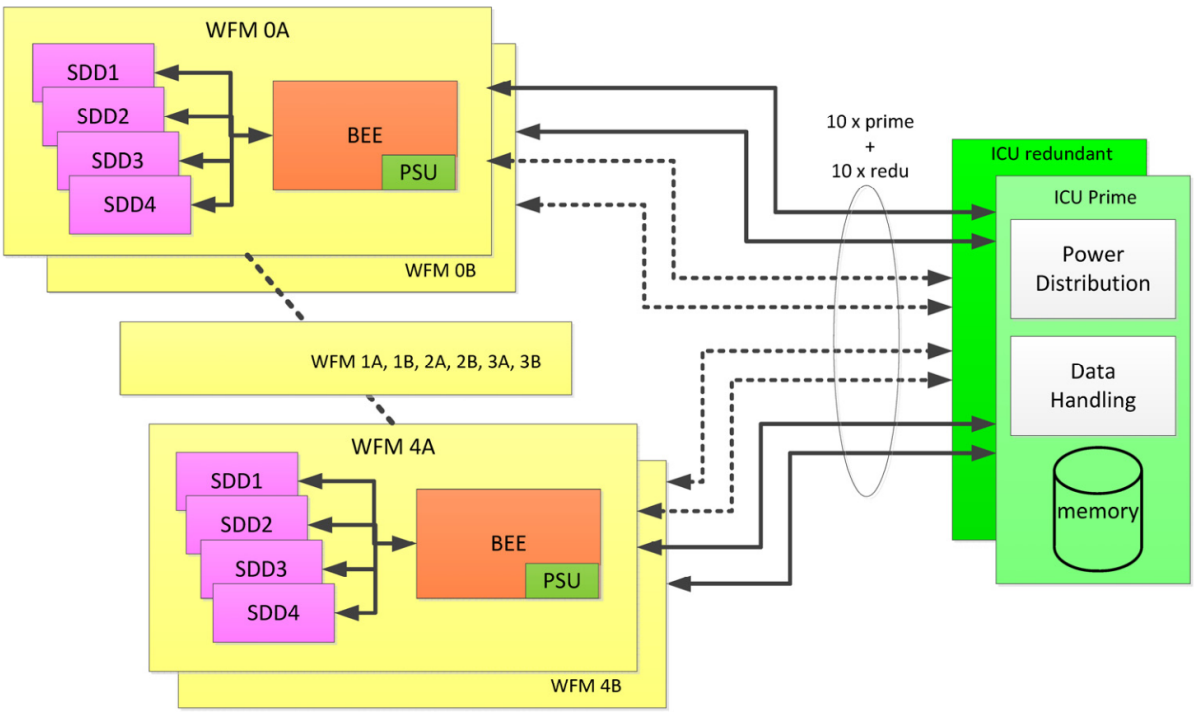


**Figure 3.13:** The electronical design of the WFM. Each of the 10 Cameras of the WFM consists of 4 SDDs/FEEs. Each camera is handled by its own BEE. The BEE communicates with the FEEs and transmit the data to the DHU. *Image: D. Walton / LOFT Assessment Study Report*

connection is very limited and in the order of 600 bit/s. This way follow-up afterglow measurements in the NIR and optical can be performed, determining spectral evolution, the redshift and the host galaxy of the burst. For the LBAS the LOFT consortium estimates a detection rate of ~120 GRBs/year. (Barret et al. 2013) The expected redshift distribution of the detected GRBs is shown on the right hand side of Figure 3.11.

Up to this point the previous chapters gave insights in the observational and scientific goals of the LOFT mission, in the instruments and techniques used and in the objects of scientific interest. They were all based on the work of the LOFT consortium and the publications of other authors. The next chapter will now focus on the BEE and the work don within the frame of this diploma thesis. It will explain the BEE's functionality, the communication with the FEE and DHU, and technical details such as the SpaceWire interface. It will also discuss the initial goals of the work and to what extend they were fulfilled. For the case of the science mode of the BEE the results are also compared with the scientific requirements discussed in Section 3.2.

# Chapter 4

# The WFM Back End Electronics

The task for this diploma thesis was the creation of a functional hardware code for the BEE FPGAs using VHDL. The main tasks the BEE should be able to perform are

- the communication with the FEE and the controlled readout of its ASICs (see Section 4.2)
- the application of corrections to the detector data and reconstruction of the event's position on the detector (see Section 4.4)
- the handling of different working modes
- the communication with the DHU via a SpaceWire connection (see Section 4.5)

The BEE will also include a housekeeping unit, that will keep track of parameters such as the temperature at the detector, the number of valid and invalid events on the detector and a power supply unit, that will distribute high voltage to the FEE. While the communication with these units is not part of this thesis, the corresponding working modes for a possible communication with these units should be included. This chapter will start with an overview of the mechanical and electronics design of the BEE in Section 4.1. Afterward it will treat the communication with the FEE and the reception and the format of the event data in Section 4.2. The different working modes of the BEE will be introduced in Section 4.3, while Section 4.4 will give a detailed explanation of the procession of the detector data in the science mode. The science mode was one of the essential parts of this diploma thesis and each of its components will therefore be discussed in detail. This chapter will then be concluded by Section 4.5, which treats the communication with the DHU and the SpaceWire interface. The results and the progress of the diploma thesis are discussed in Chapter 5.

## 4.1 BEE design

In the current design of the WFM, each camera is handled by its own BEE. Each BEE is located in a box at the bottom of the camera structure. Figure 4.1 illustrates this situation. The BEE is connected to a nominal and a redundant DHU via SpaceWire cables for communication. It receives its power by connectors to a nominal and a redundant Power Distribution Unit (PDU). The BEE is connected to each of the four FEEs of a camera by three cables. To each FEE there is one MDM-31 connectors for data transmission and two coaxial cables for the supply voltage and the drift voltage of the SDDs. A schematic illustration of the electronics design of the BEE is shown in Figure 4.2.

Communication between the BEE and the FEE is performed by the BEE's Detector Handling Unit. This unit is responsible for the transmission of commands from BEE to FEE and also for the reception of data from the FEE. The event data is handled by the BEE depending on the selected working mode. The different working modes are explained in Section 4.3. After the event data is processed, it is sent to the DHU. For this reason the BEE also possesses a Communication Unit, which is responsible for the SpaceWire interface to the DHU. The BEE can send data to the DHU and can receive telecommands in turn via this SpaceWire connection. With this illustration of the electronics design of the BEE in mind, the whole functionality of the BEE is now described step by step. The next section starts with the BEE-FEE communication.

## 4.2 Communication with the FEE

The SDDs are subdivided logically in detector halves, which are treated independently as mentioned in Section 3.3. Each detector half is handled by one Data Processing Unit (DPU) of the BEE. The component of the DPU responsible for the communication with the FEE is called Detector Handling Unit. Thus each FEE is connected to two Detector Handling Units. In the following explanation, mentions of the connection from BEE to FEE always refer to the connection of one Detector Handling Unit to the Front End Electronics of the corresponding detector half and not to the connection between the BEE and the FEE in total. The connection between BEE and FEE is illustrated in Figure 4.3. One of the tasks handled by the BEE is the distribution of a clock signal to all ASICs. Each ASIC of the detector half has its own address ranging from one to seven represented by a three bit value, which allows the addressing of commands to certain ASICs with one shared command line. There are separate lines for the transmission of commands to the ASICs as well as for the transmission of reset and hold signals. Each of these lines is connected to all of the seven ASICs and so every of these signals is sent to all seven ASICs. This way the command line for example must transmit not only the

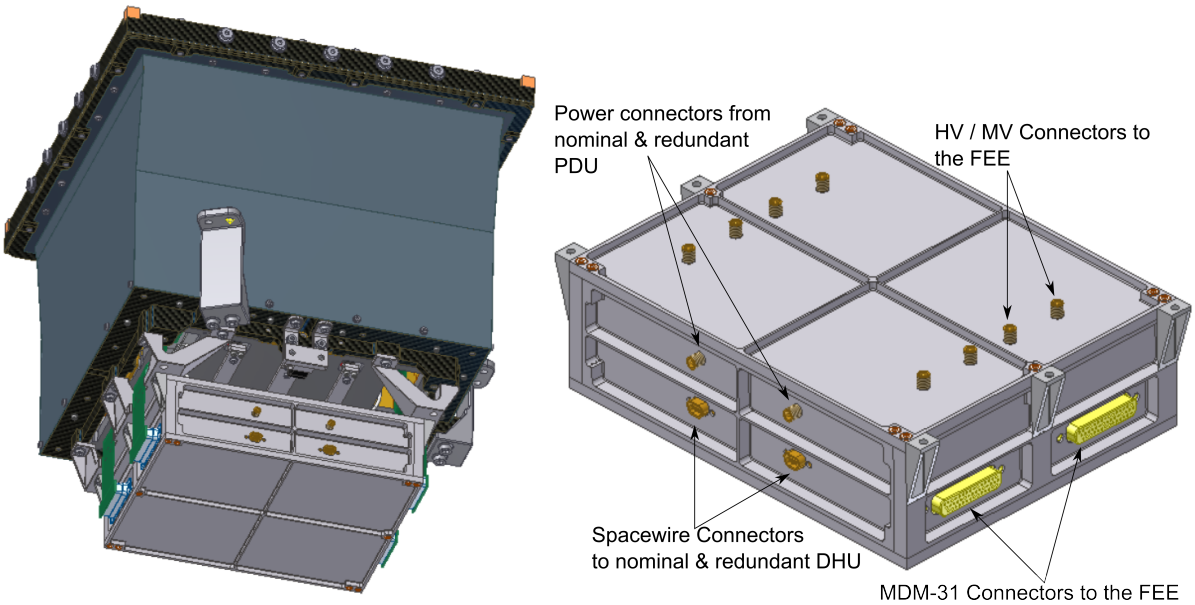


**Figure 4.1:** *Left:* WFM camera box with bottom cover removed. *Image: D. Karelin / LOFT Assessment Study Report Right:* Mechanical design of the BEE box. On the left hand side of the box are the SpaceWire connectors to the DHU and the power connectors to the PDU. On the top side are two voltage connectors for each FEE, while the data connectors are located on the front and back side of the box. *Image: S. Diebold / LOFT Assessment Study Report*

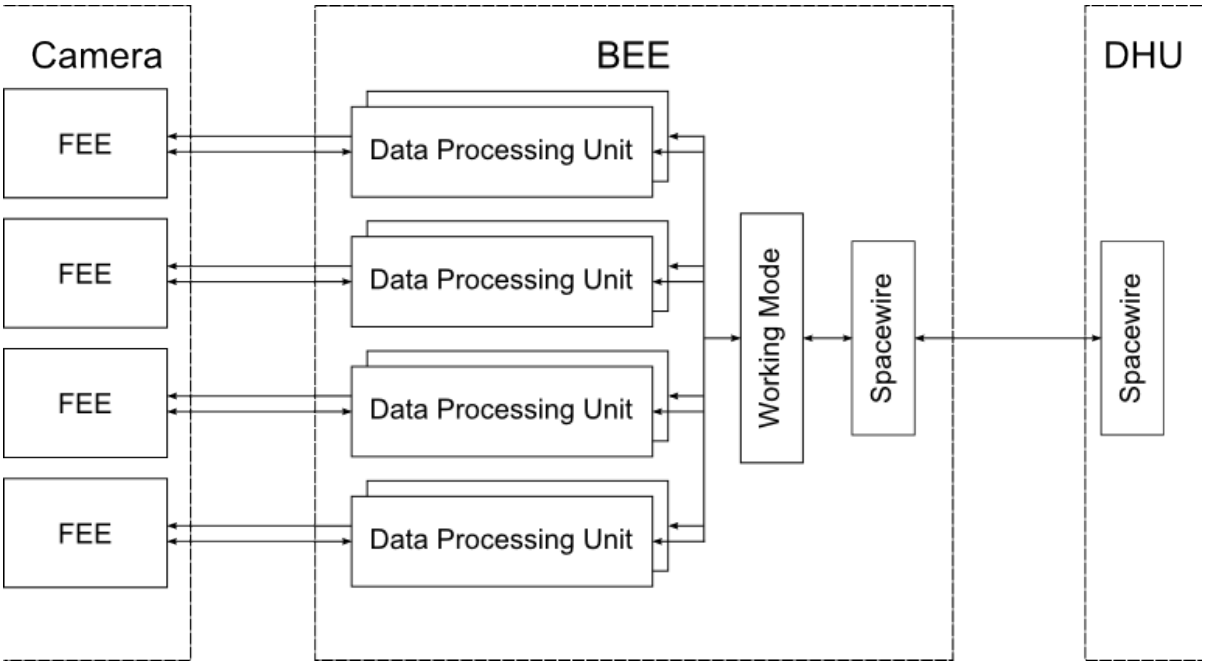


**Figure 4.2:** Schematic illustration of the electronics design of the BEE. The BEE handles the four FEEs of one camera. Each of these FEEs controls two detector halves and has one connection to a Data Processing Unit of the BEE. The Data Processing Unit communicates with the FEE of the detector half. It can send commands and configuration data to the FEE and receives the event data. Inside the BEE the data is processed depending on the selected working mode. The working mode is implemented as a state machine. The working mode can be changed by telecommands from the DHU. Event data is send from the BEE to the DHU via a SpaceWire link between these units and telecommands can be received vice versa. The DHU handles all ten BEEs.

bit sequence for a certain command, but also the targeted ASIC's address. All ASICs then compare their own address with the address in the command sequence and only act if they are the target of the command. For data transmission all odd numbered ASICs share one line and all even numbered ASICs share one data line to the BEE. This way two neighbouring ASICs can be read out at the same time, which leads to an increase in bandwidth and thus a reduction of the deadtime between events. Each ASIC has a certain trigger threshold and if the charge on an anode surpasses this threshold an event is triggered. In case of a triggered event, the readout process of the SDD is as follows:

1. If the charge accumulation rate of one or more anodes exceeds a certain threshold, an event is registered by the corresponding ASIC. The ASIC then freezes the current anode values and sends a hold signal via the trigger line to the other ASICs of the detector half, which then freeze their current anode values, and to the BEE, i.e. to the Detector Handling Unit. The ASIC then waits for commands from the BEE.

2. The Detector Handling Unit then creates a time tag. After the time tag is created, the Detector Handling Unit requests the trigger map from the ASICs. A trigger map is an array of bits, that contains a bit for each anode which is 1 if the anode value is above the threshold value or a 0 otherwise.

3. All seven ASICs transmit their trigger maps to the detector handling unit.

4. The detector handling unit evaluates the trigger maps. An event is valid, if all triggered anodes are neighbors. If the event is not valid, then the detector handling unit resets the ASICs. Otherwise the detector handling unit stores the triggered ASIC's number and requests the so-called charge map.

5. The charge map contains the digitized values of all anodes of one ASIC. In the current design each anode contains 11 bit of data. So a charge map for a WFM ASIC consists of $64 \times 11$ bit. These values are transmitted bit by bit. The odd even design of the detector half allows the simultaneous readout of two ASICs and thus reduces the time needed for transmission. This is important for so-called split events. A split event is an event, where the triggered anodes are distributed amongst two ASICs, so both charge maps are needed to reconstruct the event. For every event two neighbouring ASICs are read out to respect split events, even if only one ASIC contains triggered anodes. With the separate data lines for the odd and even ASICs this does not take extra time. These two charge maps are then transmitted to the Detector Handling Unit.

6. The Detector Handling Unit accepts the charge maps. Then it sends a reset signal to the ASICs, which then reset their anode values and continue with the measurement.

Since there is only one data line for each read out ASIC, the Detector Handling Unit receives the anode values of the charge map bit by bit. The signal of each anode consists of 11 bit, so the Detector Handling Unit stores these values in a 11 bit shift register. Each time a complete anode is transmitted and the shift register is full, the anode values are

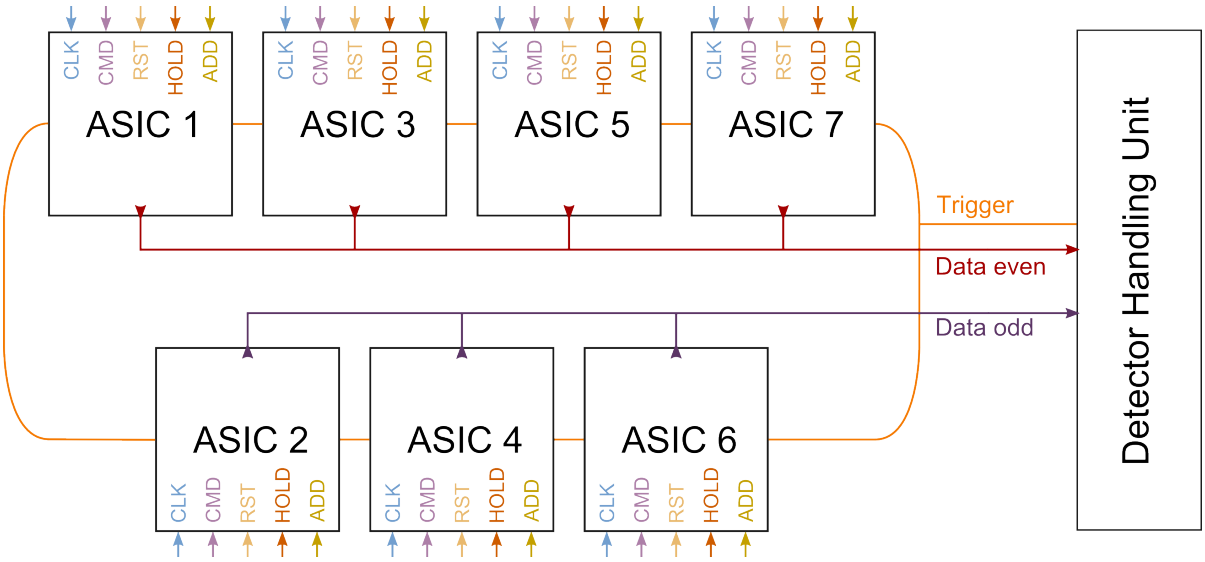


**Figure 4.3:** Illustration of the FEE BEE communication. The ASICs all share the same trigger line. If one ASIC triggers, the signal is sent to the detector handling unit of the BEE as well as to all the other ASICs, which will in turn set to hold and freeze the current anode values. The BEE distributes a clock to the ASICs of the FEE. There are separate lines to set the ASICs on hold and reset them as well as to send commands to the ASICs. The ASICs are arranged by their number in a way that the odd numbered ASICs and the even numbered ASICs each share a line for event data transmission.

set on the output signals. For the output signal of the anode, a bit that indicates if the anode triggered is added, so it is of the form

| Anode after Detector Handling Unit [12 bit] | |
|---|---|
| Triggered [1 bit] | Unsigned integer [11 bit] |

At the same time the Detector Handling Unit also sets the corresponding ASIC number signals, the timestamp signal and the output_valid signal high for one clock cycle. The output for the odd and even ASIC occurs at the same time, because of the parallel readout structure. Table 2 gives an overview of the Detector Handling Unit's output signals. The event data is then processed further by the pipeline structure of the DPU.

The Detector Handling Unit for the BEE is not yet existing. This is mainly due to the fact that there is no hardware board for the BEE yet. Therefore, there was no possibility to test the DPU in total, including the communication with an ASIC simulator. The Detector Handling Unit was simulated by a testbench, which handed the anode values, the ASIC numbers and the timestamp to the DPU. Its functionality is based on the LAD MBEE Detector Handling Unit, which works in a very similar way. Before this pipelining is explained in further detail, the different working modes of the BEE are explained.

## 4.3 The BEE Working Modes

The BEE includes several different working modes. These working modes are:

- The engineering mode allows the procedure of the DPU step by step. Thus the functionality of different components can be tested separately. The engineering mode is not yet included in this work. However the idea is to include two working modes in each component. In one of the working modes it has its usual functionality. In the other working mode it simply shifts the data from register to register to match the runtime of its normal functionality. It also changes the size of the input data to match the size of the output data in the normal functionality, without changing its actual value.

- The calibration mode is used to configure different components of the pipeline, such as the correction factors for the gain and pedestal. The calibration mode is also used to update factors of the FEE, e.g. the anode threshold. In this mode, the raw detector data can be transferred to the DHU without applying the DPU corrections. This is needed to calculate new pedestal values for the different anodes of the ASICs, which occurs in the DHU.

- The science mode is the basic working mode for the BEE. In the science mode the data of both read out ASICs are processed through the pipeline, where different corrections will be applied to the data and ADU to eV conversion takes place. After the pipeline, the position of the photon on the SDD is reconstructed and transformed to global coordinates, i.e. the camera coordinates. The output data will be a 64 bit vector containing the 16 bit fine position, 8 bit drift position, 16 bit energy and a 24 bit time stamp. These data will then be transferred to the DHU by the Communication Unit.

The current working mode of the BEE can be changed by commands from the DHU. As mentioned above, the basic working mode, in which science data is acquired, is the science mode. The functionality of this working mode was the main part of the diploma thesis and it is therefore treated in all detail in the next section.

## 4.4 Science mode

The science mode is the common working mode for the WFM. In this working mode the incident photon's energy and position on the camera are reconstructed. The data is then handed to the BEE and processed to the DHU via the SpaceWire interface. A science data packet contains the following data:

| Fineposition | Driftposition | Energy | Timestamp |
|---|---|---|---|
| 16 bit | 8 bit | 16 bit | 24 bit |

The main part of the science mode is performed by the DPU. The next subsection explains the components and the functionality of this unit.

### 4.4.1 Data Processing Unit

The DPU is responsible for the communication with the FEE and the processing of the event data. For each FEE the BEE instantiates two DPU as shown in Figure 4.2. Table 1 in the appendix lists all the input and output signals of the DPU. This table does not yet include the signal lines for the Detector Handling Unit, because it was not implemented in hardware but simulated in software. However the necessary signals are included in Table 2 in the appendix and can be looked up there. It is the main purpose of the DPU to reconstruct the photon energy and position and to create a time stamp for the initial event. Figure 4.4 illustrates the signal flow inside the DPU. The time stamp is created by the Detector Handling Unit, while the following components achieve the reconstruction of the photon energy and position. The time stamp is therefore temporally stored until the reconstruction of the other quantities is completed. The application of the pedestal, common mode and gain correction treats both ASICs separately. The parallel part and the responsible unit is called Pipeline. A list of the input and output lines of the Pipeline can be found in Table 3 in the appendix. For the reconstruction of the incident photon's energy and position the data has to pass through all units. This is done in the working mode called science mode. In the not yet implemented engineering mode, the Pipeline and the position reconstruction can be processed in parts, as described in Section 4.3. The DPU includes all components that are needed for the reconstruction of the position and energy, as well as the RAM to store certain correction values. The single steps and corrections that are necessary are explained in the next sections.

### 4.4.2 Pedestal correction

The pedestal correction is the first correction, that is applied to the anode values as received from the Detector Handling Unit. The pedestal is an offset, which results from the dark current on the detector. Thermal energy is stored in the silicon waver of the SDD in form of phonons. These phonons can cause a transition of an electron from the valence band to the conduction band and thus create an electron-hole pair. This released charge is then accelerated in the drift field the same way as charge induced by incident photons and creates a constant current on the anodes. The pedestal is the reason why

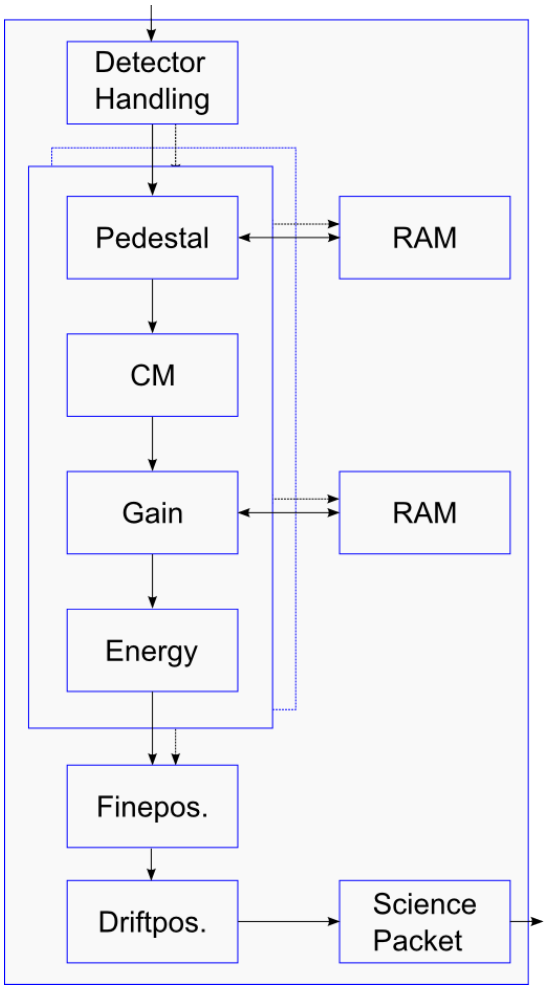


**Figure 4.4:** Illustration of the signal flow inside the PDU for the science mode. The Detector Handling Unit receives the event data from the FEE. Both ASICs have their anodes corrected separately leading to a parallel structure. Each anode has then its pedestal value subtracted. These corrections are stored inside a RAM in the PDU. The anodes then have their common mode corrected. After the Common Mode Unit follows the Gain Unit. The corresponding correction values are stored in a RAM located in the PDU as for the pedestal values. Now the energy is reconstructed and the parallel treatment ends. After that the fineposition and the driftposition are reconstructed before the data is handed to the BEE.

the detectors are cooled by a radiator on the back of the camera. While the pedestal may be constant on small time scales, it increases with mission time. Errors in the crystal structure of the silicon waver result in a decline in the band gap near the damaged location. That way more charge is induced by phonons. Since the errors in the crystal are not necessarily distributed equally on the detector plane, the pedestal is different for each anode. These correction values are stored in a $448 \times 12$ bit RAM located in the PDU and can be updated in the calibration mode during the mission. The Detector Handling Unit receives the anode values bit by bit and an anode consists of 11 bit charge data (the first bit of the 12 bit anode value is the triggered bit and is received with the trigger map), so there are 11 clock cycles between each anode input to the DPU. The anode values are still in ADU and represent an unsigned integer value. The pedestal values are 12 bit unsigned values with 11 integer bit and one fractional bit. Since the pedestal values are simply subtracted from the anode values, the resulting anode values have a length of 14 bit and following composition:

| Anode after pedestal correction [14 bit] | | | |
|---|---|---|---|
| Triggered [1 bit] | Signed [1 bit] | Integer [11 bit] | Fractional [1 bit] |

As mentioned above, this pedestal correction takes place in the Pipeline. The Pipeline counts the anodes it receives and hands the number for the next anode to the PDU. Together with the ID of the current ASIC the PDU can then load the corresponding correction value from the RAM and transmit it to the Pipeline. Since there are 11 clock cycles between two consecutive anodes, there is always enough time to apply the correction. The Pipeline then subtracts the correction value from the anode and transfers the result to the Common Mode Unit.

### 4.4.3 Common mode correction

The common mode error has its origin in fluctuations of the supply voltage. If treated correctly, the common mode consists of two components. One component is located in the signal preamplifier of the ASIC. That preamplifier is located directly at the anodes and it amplifies the current on the anodes and transforms it into a voltage. In an ideal case, the preamplifier would amplify the current each time by the same factor. However small fluctuations in the supply voltage of the preamplifier result in an shift of the bias. This causes a small offset to the anode charge. The supply voltage is the same for all anodes on one ASIC, so the offset is also the same for all anodes on this ASIC. The second error however is more problematic. It is caused by fluctuations in the drift voltage of the SDD. Since this effect affects all electrons drifting in the field, this results in an multiplicative error on each anode. It is very computing power intensive to correct this effect. The correction of the common mode used in the BEE is therefore an approximation as an additive error. It is calculated as the median of all non-triggered anodes of one ASIC

(which is correct for the additive component, but not for the multiplicative component). The component responsible for this correction is called Common Mode Unit. This unit includes two kind of memory. The first one is a $64 \times 14$ bit FIFO, which stores all anodes of one ASIC until the median has been calculated. The second memory is a $64 \times 14$ bit array, in which all non-triggered anodes are stored sorted by their value. After all non-triggered anodes have been sorted, the anodes stored in the FIFO have the median of the not triggered anodes subtracted and are transmitted to the next unit. The output format of the anode's energy data does not change compared to the input format.

| Anode after common mode correction [14 bit] | | | |
|---|---|---|---|
| Triggered [1 bit] | Signed [1 bit] | Integer [11 bit] | Fractional [1 bit] |

While the calculation of the median requires quite some resources to sort and store the anodes, it is superior to the calculation of the mean value since it is not affected by spikes and avoids division, which is computing power intensive on an FPGA. To sort the anodes, the Common Mode Unit simply compares the current anode with all elements already stored in the array, starting with the high numbered elements. If the value of an element is less than the value of the anode, this element and all elements with smaller numbers are shifted by one array slot to smaller numbers and the current anode is stored in its place. While this sorting algorithm would be very slow in software, it is very fast in hardware, because all comparisons are performed in the same clock cycle and thus the whole sorting process is completed in only one clock cycle. However comparing the anode with all elements of the array is quite resource intensive and since resources turned out to be a limiting factor, possible improvements are discussed in Section 5.2.2. A list of the signals of the Common Mode Unit is found in Table 4 in the appendix.

### 4.4.4 Gain correction

The PDU then passes the anodes to the Gain Unit. The Gain Unit corrects an error which has its origin in the constructional differences of some components of the ASICs. The contributing components are

- the charge sensitive amplifier, which converts the current on the anode to a voltage and amplifies it. The charges registered by the anodes are very weak and could not be transmitted over longer distances due to transmission losses. The amplified voltage however can be transmitted with nearly no loss. The charge sensitive amplifier also contributes to the common mode.
- the shaper or filter, which smoothes high frequent noise on the detected signal.
- the Analog Digital Converter, which converts the analog signal into a digital signal.

The gain correction is a multiplicative correction. The formula used for the correction is

$$E_{corrected} = E(1 - \mathrm{C}(T - \mathrm{T}_0)) = E(1 - \mathrm{C}\Delta T).$$

$E$ is the energy measured by the anode and is still in ADU, while $E_{corrected}$ is the energy of the anode after gain correction in eV. The correction is temperature dependent and $\mathrm{T}_0$ is the reference temperature, which should be around $-20\,^{\circ}\mathrm{C}$. C is the gain correction factor, which is individual for each anode. It is given in $\frac{\mathrm{eV}}{\mathrm{ADU}\times\mathrm{K}}$, since this correction also includes the transformation from ADU to eV. These factors are stored in a RAM in the DPU the same way as for the pedestal correction values. Since the temperature is also relevant for the reconstruction of the drift position, each DPU has a port to the BEE to receive the current temperature value. $\Delta T$ is calculated in the DPU and handed to each of both pipelines, i.e. their gain units.

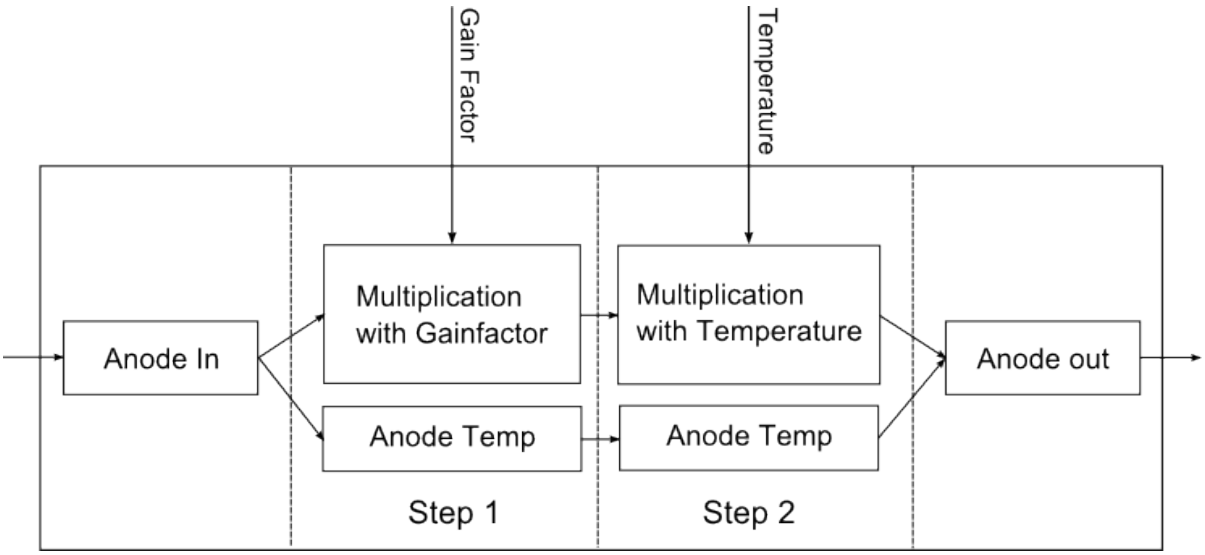


**Figure 4.5:** Illustration of the signal flow in the Gain Unit. The original incoming anode is stored in a register while its energy value is at the same time handed to the multiplier. In step one the energy value of the anode is then multiplied with the corresponding gain factor of the anode. In the second step the result of the previous multiplication is then multiplied with the temperature correction and the temporally stored anode is shifted to the next temporal memory. In the last step the output is defined as the difference of the anode's initial energy and the result of the multiplication.

The energy value of the common mode corrected anode is handed to the Gain Unit as described in the precedent tabular. In the first step the anode's energy value is multiplied with its gain correction factor. The triggered bit is excluded from the multiplications and appended again, after the complete correction of the gain unit has been applied.

| Multiplication of input anode with gain correction factor | | | |
|---|---|---|---|
| Quantity | Signed [bit] | Integer [bit] | Fractional [bit] |
| Input Anode | 1 | 11 | 1 |
| Gain correction factor | 0 | 6 | 7 |
| Anode × Gain | 1 | 17 | 8 |

The result of this multiplication consists of 26 bit. In the next step the temperature correction has to be applied. Since there was no information available on the data format and accuracy of the temperature value, $\Delta T$ was assumed as an unsigned 10 bit value with an accuracy of 0.5°. A later adaption of the data format is possible with the flexible design of the BEE.

| Multiplication of the gain factor corrected anode with temperature correction factor | | | |
|---|---|---|---|
| Quantity | Signed [bit] | Integer [bit] | Fractional [bit] |
| Anode × Gain | 1 | 17 | 8 |
| Anode completely corrected | 1 | 18 | 17 |

The result of this multiplication is now subtracted from the input anode's value, which was temporally stored, to complete the gain correction. Some of the fractional bits of the result are dropped, to reduce the resources used in the FPGA and since the calculation does not yield such an high accuracy. The output of the Gain Unit then has the following format:

| Anode after gain correction [28 bit] | | | |
|---|---|---|---|
| Triggered [1 bit] | Signed [1 bit] | Integer [18 bit] | Fractional [8 bit] |

The value of each anode is now in eV and represents the energy deposed on this anode by the incident photon.

### 4.4.5 Energy Reconstruction Unit

The reconstruction of the energy is now quite simple. The only difficulty, that has to be taken into account, is the deposition of energy in the not triggered anodes, which are next to triggered anodes. That is the energy deposed in the tail of the charge cloud. Figure **??** illustrates this situation. The Energy Reconstruction Unit therefore compares the triggered flag of the current anode with the triggered flag of the previous anode. If

the triggered flags are 01, that indicates the left flank of the photon's charge distribution, while 10 indicates the right flank. Thus the tail of the right flank and respectively the tail of the left flank are considered in the calculation of the total energy. Anodes that have already been considered in the calculation exit the Energy Reconstruction Unit and subsequently the pipeline. Since the following position reconstruction uses only anodes, which detected a part of the photon's energy (triggered anodes plus their neighboring anodes), only these anodes are handed to the next unit. Therefore the triggered bit loses its original purpose and is removed.

| Anode after energy reconstruction [27 bit] | | |
|---|---|---|
| Signed [1 bit] | Integer [18 bit] | Fractional [8 bit] |

When all 64 anodes of one ASIC have passed this unit, the total energy is handed to the output of the pipeline. The pipeline structure, where the even and the odd ASIC where treated parallel, ends here. In case of a split event the energy output of each pipeline contains only a part of the photon's total energy. However the total energy of both ASICs is valid at the same time, since the run time of the pipeline is the same for both ASICs. This allows the DPU to simply sum up the energy results of both pipelines and hand the resulting total energy of the event to the Fineposition Reconstruction Unit.

### 4.4.6 Position Reconstruction

The first goal of this subsection is to explain the physics behind the reconstruction of the event's position on the detector plane. It is based on the work of Crescio and Nouais 2006 and Campana et al. 2011.
The incident photon creates an initial charge cloud with a width of ~20 µm by interaction in the silicon wafer of the SDD. The charge cloud is focused by the electric field in the middle plane of the wafer, where it quickly assumes a Gaussian shape. It is then accelerated by the drift field towards the anodes. On its way to the anodes the charge cloud broadens due to electrostatic repulsion and diffusion of the electrons in drift direction as well as in anode direction. The electrostatic contribution to this broadening process is much smaller than the diffusion's contribution and is therefore neglected in the calculation. The width of the charge cloud on the anodes is given by

$$\sigma(t) = \sqrt{2Dt + \sigma_0^2}. \tag{4.1}$$

D is the diffusion coefficient, t the drift time and $\sigma_0$ the initial width of the charge cloud. The charge distribution on the anodes is given by the projection of the charge cloud on the anodes and follows a Gaussian distribution

$$\rho(x, x_0, \sigma) = A \cdot \mathrm{e}^{-\frac{(x-x_0)^2}{2\sigma^2}}. \tag{4.2}$$

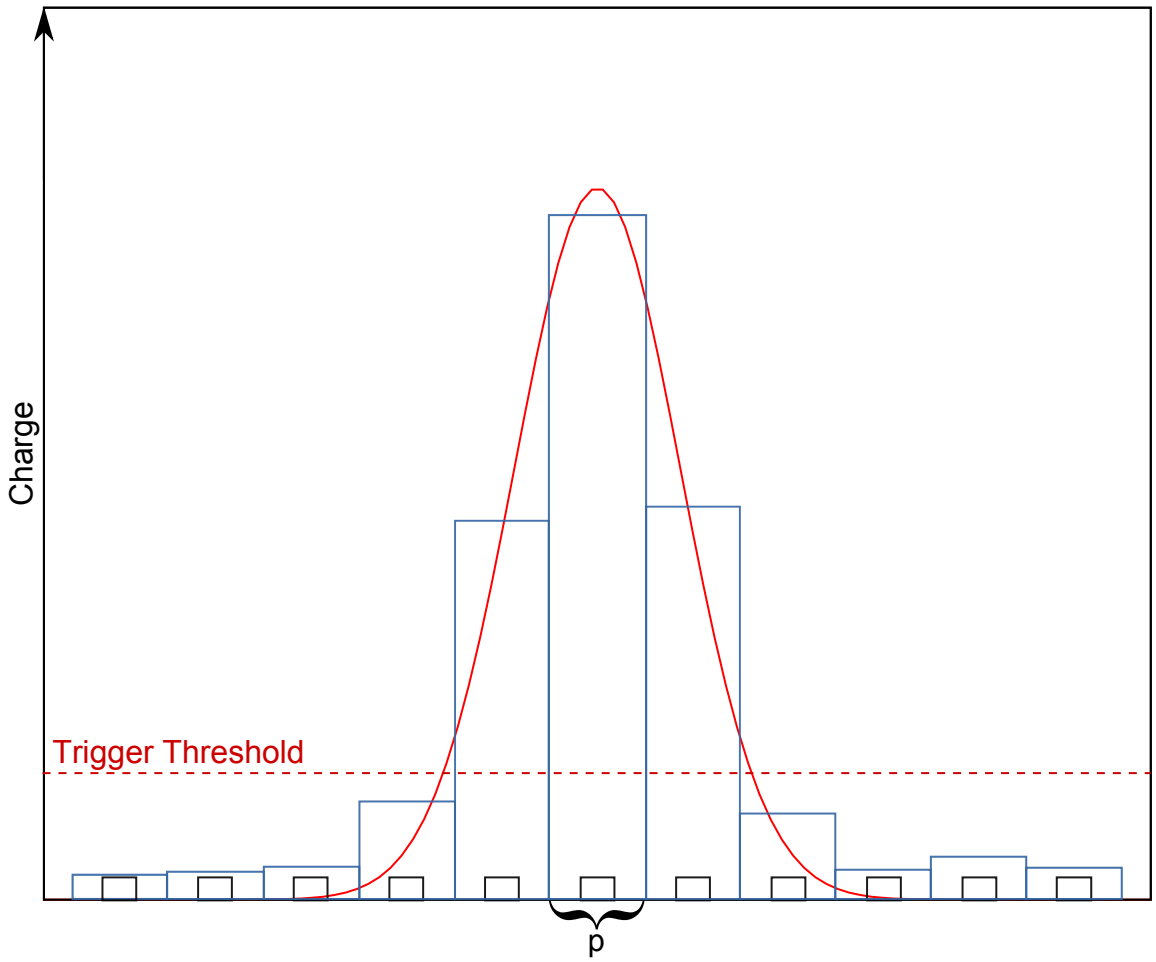


**Figure 4.6:** The red Gaussian function shows the resulting charge distribution of one event, after the charge cloud drifted towards the anodes. This curve results in a discrete charge distribution on the anodes (blue columns). If the charge collected on one anode exceeds the trigger threshold (red dotted line), the anode triggers. If only the triggered anodes are considered in the calculation of the total charge, some charge distributed on the neighboring anodes, that did not trigger, might be lost in the calculation. However if too many anodes are included in the calculation of the total energy, additional noise is added. p is the anode pitch.

A is the total charge of the cloud, while $x_0$ is the center of the Gaussian function and therefore the interaction position of the photon in anode direction. The charge on one anode centered on the origin is calculated by

$$Q = \int_{-\frac{p}{2}}^{+\frac{p}{2}} A \cdot \mathrm{e}^{-\frac{(x-x_0)^2}{2\sigma^2}} \mathrm{d}x \tag{4.3}$$

$$= A \cdot \sigma \sqrt{\frac{\pi}{2}} \left( \mathrm{erf}\left( \frac{p/2 - x_0}{\sigma\sqrt{2}} \right) - \mathrm{erf}\left( \frac{-p/2 - x_0}{\sigma\sqrt{2}} \right) \right). \tag{4.4}$$

p is the anode pitch and the Gauss error function erf($x$) is defined as

$$\mathrm{erf}\,(x) = \frac{2}{\sqrt{\pi}} \int_0^x \mathrm{e}^{-t^2} \mathrm{d}t. \tag{4.5}$$

It is related to the integral of the normal Gauss distribution $\Psi\,(x)$ by

$$\Psi\,(x) = \frac{1}{2} + \frac{1}{2}\mathrm{erf}\left( \frac{x}{\sqrt{2}} \right). \tag{4.6}$$

In this case the anode collects all charge between -p/2 and +p/2, while the anode to the left of it would collect the charge from -3p/2 to -p/2. Figure 4.6 might help to understand this situation. Therefore the total charge of the event is given by

$$Q_{total} = \sum_{n=0}^{N} q_n \tag{4.7}$$

with

$$q_n = \int_{x_l^n}^{x_r^n} A \cdot e^{-\frac{(x-x_0)^2}{2\sigma^2}} \mathrm{d}x \tag{4.8}$$

$$= A \cdot \sigma \sqrt{\frac{\pi}{2}} \left( \mathrm{erf}\left( \frac{-x_r^n - x_0}{\sigma\sqrt{2}} \right) - \mathrm{erf}\left( \frac{-x_l^n - x_0}{\sigma\sqrt{2}} \right) \right). \tag{4.9}$$

$x_l^n$ is the left border and $x_r^n$ the right border for the according anode. While it would be the correct way to extract the event position in anode direction $x_0$ from this equation, this would require a fitting algorithm, because $x_0$ and $\sigma$ are unknown, and a fitting process would require a microcontroller. A better way to calculate $x_0$ in an FPGA is an approximation assuming a discrete charge distribution. For this discrete charge distribution, the centroid is given by

$$x_{\mathrm{SDD}} = \frac{\sum_{n=0}^{N} a_n x_n}{\sum_{n=0}^{N} a_n} = \frac{\sum_{n=0}^{N} a_n x_n}{Q}. \tag{4.10}$$

$a_n$ is the charge of one anode, $x_n$ is the position of the anode on the ASIC and Q the total charge of the event. Since the reconstruction of the position takes place after the

ADU to eV conversion, the charge in this formula is replaced by the energy.
The calculation of the driftposition is a bit more complicated. The basic idea is to calculate the drift distance using the width of the charge distribution on the anodes. This is also an approximation, since the electrostatic component for the broadening of the charge cloud was neglected in Equation 4.1. We start with the drift parameter D from Equation 4.1. The drift parameter D is given by

$$D = \frac{\mathrm{k_B} T v}{qE} = \frac{k_B T x_\mathrm{D}}{\mathrm{q} E t}. \tag{4.11}$$

T is the temperature of the detector, $\mathrm{k_B}$ is the Boltzmann constant, q the elementary charge, E the drift field, v the drift velocity, $x_\mathrm{D}$ the drift distance and t the drift time. Together with Equation 4.1, which describes the width of the cloud as a function of the drift time, this leads to

$$x_\mathrm{D} = \frac{\sigma^2 - \sigma_0^2}{2\mathrm{k_B} T} \mathrm{q} E. \tag{4.12}$$

The resulting formula is independent of the drift time. $\sigma$ can now be calculated with the approximation for $x_\mathrm{SDD}$ as standard deviation

$$\sigma^2 = \frac{1}{E_{total}} \cdot \sum_{n=0}^{N} a_n \left(x_n - x_\mathrm{SDD}\right)^2. \tag{4.13}$$

Combined Equation 4.12 and Equation 4.13 yield the drift distance of the photon

$$x_\mathrm{D} = \frac{\mathrm{q} E}{2\mathrm{k_B} T} \left( \left( \frac{1}{E_{total}} \cdot \sum_{n=0}^{N} a_n \left(x_n - x_\mathrm{SDD}\right)^2 \right)^2 - \sigma_0^2 \right). \tag{4.14}$$

The next subsections will treat the implementation of the algorithms in the BEE design.

### Fineposition Reconstruction Unit

The Fineposition Reconstruction Unit receives the anode values and their corresponding number on the ASIC from the Pipelines. Only anodes, that contribute to the photon energy, are considered in the calculation of the event's position. The anodes at the output of these Pipelines cannot be contributing to the photon energy at the same time, because the event distributes its energy either on one of both ASICs, in which case there is only output of one Pipeline, or on two ASICs in case of a so-called split event, in which the resulting charge distribution extends over the anodes of two ASICs. A split event affects the high numbered anodes on the left one of the affected ASICs and the low numbered anodes on the right one of the affected ASIC. With a maximum number of eleven anodes contributing to one event and 64 anodes per ASIC, there can never be a

time where both Pipelines (which work synchronous) have a contributing anode output. Thus the Fineposition Reconstruction Unit can neglect this case where two anodes have to be considered in the calculation of the event's position at the same time and focus on one contributing anode at a time.
The fineposition is reconstructed as described by Equation 4.10. In a first step the unit multiplies the anode charge with its position. This is done for every anode contributing to the event and the results are summed up.

| Multiplication of the anode charge with the corresponding anode number | | | |
|---|---|---|---|
| Quantity | Signed [bit] | Integer [bit] | Fractional [bit] |
| Anode charge $a_n$ | 1 | 18 | 8 |
| Anode number $x_n$ | 0 | 9 | 0 |
| Result $a_n x_n$ | 1 | 27 | 8 |
| $\sum_{n=0}^{N} a_n x_n$ | 1 | 31 | 8 |

The sum over the weighted anodes has 4 additional bit, because of the up to eleven contributing anodes. When the last anodes have been considered in the calculation and the total energy is valid, the stored sum of the weighted anodes is divided by the total energy. The accuracy of the energy and the weighted sum has to be reduced to fit the restrictions of the divider core used in the implementation.

| Division of the weighted sum by the total energy of the event | | | |
|---|---|---|---|
| Quantity | Signed [bit] | Integer [bit] | Fractional [bit] |
| $\sum_{n=0}^{N} a_n x_n$ | 0 | 26 | 6 |
| Total Energy | 0 | 17 | 6 |
| Fineposition $x_{\mathrm{SDD}}$ | 0 | 9 | 7 |

The anode values are stored in an array during the calculation. They are handed to the Driftposition Reconstruction Unit when the calculation of the fineposition is finished. The reason for this storage is, that the fineposition is needed for the reconstruction of the driftposition, and thus the anodes cannot be processed until the complete calculation is finished. Up to this point the reconstructed fineposition is dimensionless. To get the fineposition in µm, it has to be multiplied with the anode pitch. This however is done at the end of the pipeline, because the multiplication results in a loss of accuracy. The result for the fineposition as handed to the Driftposition Reconstruction Unit is therefore still dimensionless. The least significant bit is equivalent to $x_{\mathrm{SDD,LSB}} = \mathrm{Anodepitch} \times 2^{-7}$, which equals $x_{\mathrm{SDD,LSB}} = 145\,\mu\mathrm{m} \times 2^{-7} \approx 1.133\,\mu\mathrm{m}$ for the current WFM design.

### Driftposition Reconstruction Unit

The calculation of the driftposition starts with the calculation of $\sigma^2$ following Equation 4.13. First $(x_n - x_{\mathrm{SDD}})^2 = \Delta x^2$ is calculated using DSP_48 logic. $\Delta x$ consists of three integer bits and all seven fractional bits of the fineposition. With a Gaussian charge distribution on the anodes and a maximum of eleven contributing anodes, the maximum value of $\Delta x$ should be in the order of ~5. Therefore 3 bits for the integer value are sufficient. Also the sign bit is neglected, since $\Delta x$ is squared afterward by the mentioned DSP_48 core. The result is afterwards multiplied with the anode charge $a_n$, summed up for all anodes and divided by the total energy. Slice logic was used for the instantiation of the cores associated with the multiplication and division.

| Driftposition quantities | | | |
|---|---|---|---|
| Quantity | Signed [bit] | Integer [bit] | Fractional [bit] |
| $\Delta x = x_n - x_{\mathrm{SDD}}$ | 0 | 3 | 7 |
| $\Delta x^2$ | 0 | 6 | 8 |
| $a_n \Delta x^2$ | 1 | 23 | 9 |
| $\sum_{n=0}^{N} a_n \Delta x^2$ | 1 | 26 | 9 |
| $\sigma^2$ | 0 | 6 | 7 |
| $C = y_{anode}^2 \cdot 10^6 \cdot \frac{qE}{2\mathrm{k_B}}$ | 0 | 13 | 4 |
| T | 0 | 9 | 2 |
| Driftposition $x_{\mathrm{D}}$ | 0 | 6 | 2 |

The initial charge cloud size $\sigma_0$ is neglected in the calculation as suggested by Campana et al. 2011. $\sigma_0$ should be around ~20 µm whereas $\sigma$ is in the order of a few mm, making $\sigma_0^2 \ll \sigma^2$. The quantity $\frac{qE}{2\mathrm{k_B}}$ is a constant, that can be calculated in advance. It is however not complete, because sigma is yet dimensionless, but shall be measured in mm. The completed formula therefore is $C = y_{anode}^2 \cdot 10^6 \cdot \frac{qE}{2\mathrm{k_B}}$. The drift voltage of 1.3 kV distributed over a distance of 35 mm leads to a drift field $E = 360\,\mathrm{V\ cm^{-1}}$ and $y_{anode} = 145\,\mu\mathrm{m}$ is the anode pitch. This results in a constant $C \approx 4380.2083\,\mathrm{mm\ K}$. To complete the reconstruction of the driftposition, the result of the multiplication of $\sigma^2 \cdot C$ is divided by the temperature. The least significant bit of the driftposition equals $x_{\mathrm{D,LSB}} = 0.25\,\mathrm{mm}$ for the current WFM design.

### Transformation to global coordinates

The reconstruction of the position in drift and anode direction on the detector plane is completed by multiplying the still dimensionless fineposition with the anode pitch. These positions however refer to the position of the event on the corresponding SDD. An

additional transformation to the camera coordinates is required and this transformation has to take into account small misalignments of the mounting of the SDDs on the FEE board. Figure 4.7 illustrates these misalignments. These displacements occur only in the x-y plane and the SDDs are flat on the FEE board, so that the correction of the position is a simple sin or respectively cos function. The displacement can be measured and the correction can be calculated in advance of the mission, so that the correction on-board involves only a simple multiplication by a correction factor. Adding an offset in drift and respectively in fine direction based on the position of the SDD in the camera completes the transformation. This functionality has not been included in the BEE yet, but the idea is to hand the individual DPUs the correction factors as generics. The implementation therefore only includes an addition and a multiplication of standard logic vectors. However the accuracy, i.e. the bit length of these factors is yet unknown and has to be constrained first.

The results of the reconstruction are then handed to the surrounding functionality of the BEE together with the temporally stored time stamp. The multiplications and divisions, which are necessary for the reconstruction of the incident photon's position on the detector plane, make the Fineposition Reconstruction Unit and the Driftposition Reconstruction Unit the most resource intensive units in the whole pipeline. Section 5 presents a list of the separate units, their resource budget and presents some ideas to reduce this large use of resources. Section 5 also shows the results and the quality of the position reconstruction.

## 4.5 Communication with the DHU

The reconstructed data has now to be transferred to the DHU. The event data as processed by the DPU has at first to be temporally stored, since there can be simultaneous events from different PDUs, which have to be transmitted event by event. The BEE uses an array of $8 \times 65$ bit for this purpose. For each DPU there is one 65 bit element of the array, with a data format as described by the table below.

| Array science data element [65 bit] | | | | |
|---|---|---|---|---|
| Valid | Fineposition | Driftposition | Energy | Timestamp |
| 1 bit | 16 bit | 8 bit | 16 bit | 24 bit |

The BEE checks the array for valid events during each clock cycle, starting with the first element of the array. If there is a valid event in the array, it is then stored in a $16 \times 64$ bit FIFO to allow the acceptance of new events, and the valid bit is set to low. The data stored in the FIFO is then transmitted to the DHU by the so-called Communication Unit via a SpaceWire connection.

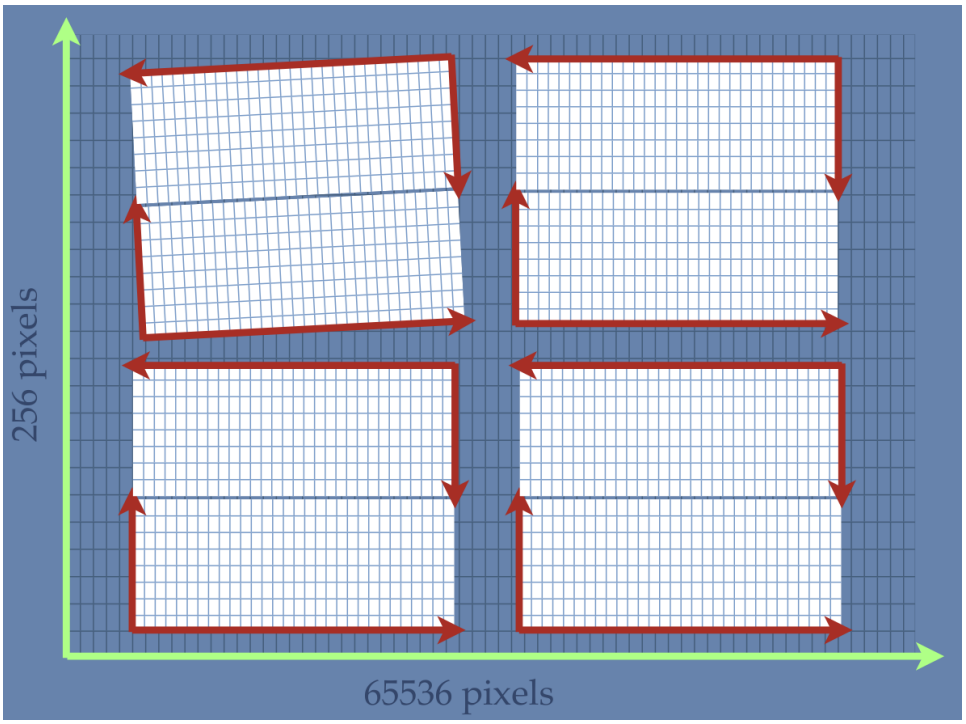


**Figure 4.7:** Illustration of possible misalignments of the SDDs on the FEE tray. While a flat mounting of the SDDs on the FEE tray is possible rotational displacements of the SDDs are most likely to occur. These misalignments have to be considered and corrected when transforming from the event coordinates on one SDD to the camera coordinates. *Image: C. Tenzer, IAAT*

### 4.5.1 SpaceWire

SpaceWire is a low voltage differential signal (LVDS) communication network, based on the IEEE 1355 communication standard. Possible high transmission rate of up to 200 Mbit $s^{-1}$, the low use of resources and the high transmission error resistance have led to its use in many spacecraft missions of the ESA, NASA, JAXA and CNSA. Spacewire connections are used in LOFT for the communication between the BEE and the DHU for the WFM and between the PBEE and the ICU for the LAD. Spacewire cables have multiple features to reduce error susceptibility such as different shieldings, filler materials to provide a uniform impedance over the cable and LVDS transmission. Figure 4.9 shows a cross section of a SpaceWire cable. These cables consist of nine lines as illustrated in Figure 4.8. There are two signals to transmit (DOUT and SOUT) and two signals to receive (DIN and SIN) data. Each of these signals is transmitted as LVDS and therefore requires two lines. The remaining ninth line is the inner shield, which is kept at ground potential. The advantage of the LVDS transmission is the high resistance to transmission errors induced by electromagnetic waves, since the shift in the potential is induced on all lines, but only the difference in the potentials between two lines is measured, which stays the same.
Spacewire uses data-strobe encoding. The data signal transmits the actual data, while the strobe signal changes, whenever the data signal does not change. Figure 4.10 illustrates both the differential signal and the behavior of the strobe signal. The advantage in the use of the strobe signal is the possible recognition of bit flip errors. If there is a bit flip in the data or the strobe signal, then the strobe signal and the data signal either change at the same time, or they remain the same at the same time. Both situations are forbidden by the behavior of the strobe signal. The SpaceWire controller therefore recognizes an error and can thus request a resend of the data packet. The SpaceWire signals can even be used to transmit a clock signal by applying XOR to the strobe signal and data signal, this however is not used in LOFT, because it would require an unnecessary high clock frequency.
Spacewire data is transmitted in packets and there are two different types of packets:

- Data packets consist of 10 bit. The first bit is the parity bit, the second bit is the control flag and then there are 8 bit of data, starting with the least significant bit. The purpose of the parity bit is to allow the detection of bit flip errors. It is set in such a way, that the parity of the 2 or 8 last bits of the previous packet (depending on whether it was a data or an control packet) and the parity bit and the control flag of the current packet have odd parity, i.e. there is an odd number of high bits. The control flag for data packets is low.

- Control packets consists of 4 bit. The first bit is the parity bit and it is set according to the parity bit for data packets. The control flag for control packets is set high and it is succeeded by two bits, that determine the type of the control packet:

- The flow control token (FCT) contains two low bits.
- The end of packet token (EOP) contains one low bit succeeded by one high bit. It indicates the end of a successful transmission of a series of data packets.
- The error end of packet token (EEP) contains one high bit, which is succeeded by one low bit, and is transmitted to end an erroneous data transmission.
- The escape token (ESC), which contains two high bits.

The transmission of an ESC followed by the transmission of a FCT is called NULL token. These token are transmitted at times, when there is no data transmission in the SpaceWire network. This continuous transmission allows the immediate detection of a disconnect of the SpaceWire link. The level of detail of this short discussion of SpaceWire is sufficient to understand the content of this diploma thesis. For further details, such as the establishing of a SpaceWire link, see European Space Agency 2008.

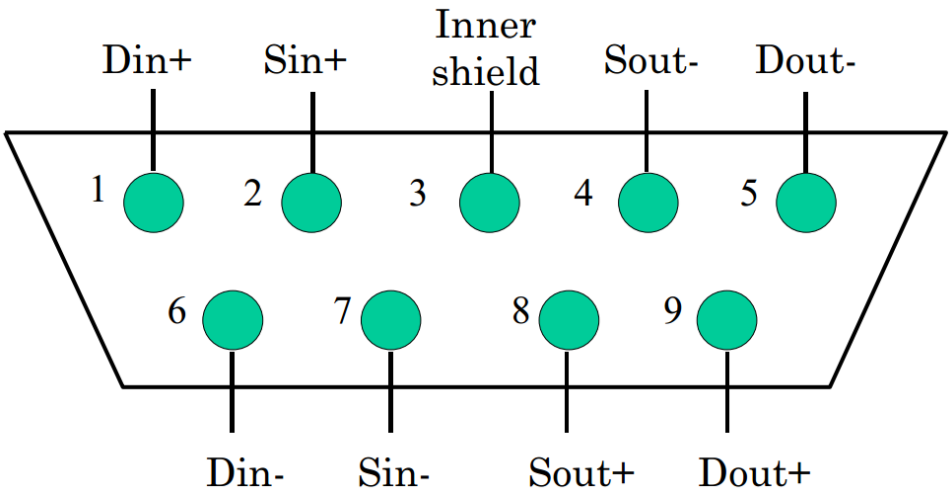


**Figure 4.8:** Illustration of a SpaceWire connector. The connector consists of nine lines. These lines are the inner shield, which is kept at ground potential, and the lines for the strobe and data in and out signals. These signals are LVDS and therefore there are two lines for each signal. *Image: European Space Agency 2008*

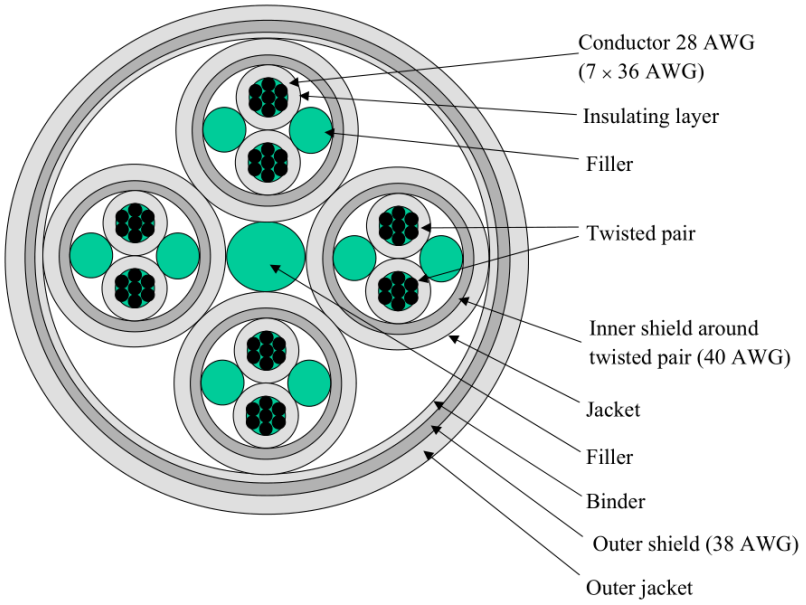


**Figure 4.9:** Illustration of a cross section of a SpaceWire cable, that shows the strong measures to provide error resistance. The twisted pair cables are shielded by multiple shielding layers. Filler materials are used to ensure a constant diameter of the signal line under the shielding and to provide a uniform impedance over the cable. *Image: European Space Agency 2008*

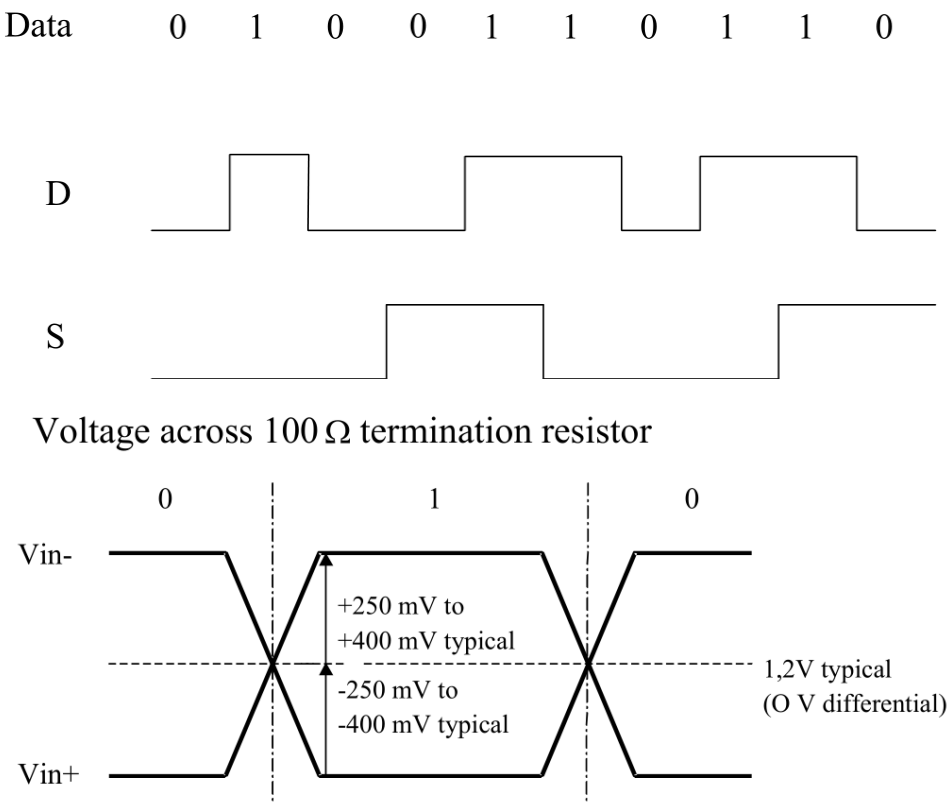


**Figure 4.10:** *Top:* Illustration of the data and strobe signal. The data signals carries the transmitted data, while the strobe signal changes, when the data signal does not change. Therefore bit flip errors can be recognized.
*Bottom:* Schematics of the working principle of LVDS. The potential difference between Vin- and Vin+ is measured. The signal is then high or respectively low, depending on the sign of the difference. A potential shift induced by an electromagnetic wave is induced on both lines and the difference therefore remains unaffected. *Image: European Space Agency 2008*

### 4.5.2 Telemetry Structure

The communication of the BEE and the DHU via the SpaceWire link must follow a certain packet structure as listed in the table below:

| Packet structure for BEE - DHU communication | | | | | |
|---|---|---|---|---|---|
| | Header | | Cargo | CRC | EOP |
| Address | Packet Type | Length | | | |
| 1 byte | 1 byte | 2 byte | 0 byte-65 535 byte | 1 byte | 4 bit |

- The address depends on whether the BEE received the command from the DHU or the BEE transmits data to the DHU. In case of a received command, the address is the destination logical address, i.e. the unit addressed by the command. The possible addressed units can be either the BEE, the Housekeeping Unit, the Power Supply Unit or one or all ASICs of the FEE. In case of a command transmitted by the BEE, the address is the address of the unit the data originates from.
- The packet type states the type of the data contained in the packet. An example would be an update for the pedestal values stored in the RAM of a certain DPU.
- The length contains the total length of the cargo field.
- The cargo field includes the actual data of the packet. Its length can vary from a simple command with few bits such as the readout of the temperature to long commands with many bits, such as the update of the gain values of one DPU.
- The CRC byte contains the CRC-8 check sum. CRC stands for cyclical redundancy check and is a routine to avoid erroneous transmissions, while the number behind the CRC makes a statement about the length of the check sum. The check sum is created as remainder of the polynomial division of the transmitted data by the so-called creator polynomial. This polynomial is then appended to the transmitted data. The receiver divides the transmitted data by the creator polynomial again, but this time including the CRC check sum. If no transmission error occurred, this will result in a remainder of zero.
- The last 4 bit are the EOP command packet as described in Subsection 4.5.1.

#### Communication Unit

The communication of the BEE with the DHU is for the BEE handled by the Communication Unit (CU). This unit includes the SpaceWire and the CRC functionality. The cores used in this work were the SpaceWire Light core from van Rantwijk 2010 and the Ultimate CRC core from Drange 2005. Both can be accessed via opencores.org. The

signal flow in the CU is illustrated in Figure 4.11, while Table 9 in the appendix lists all of the CU's signals.

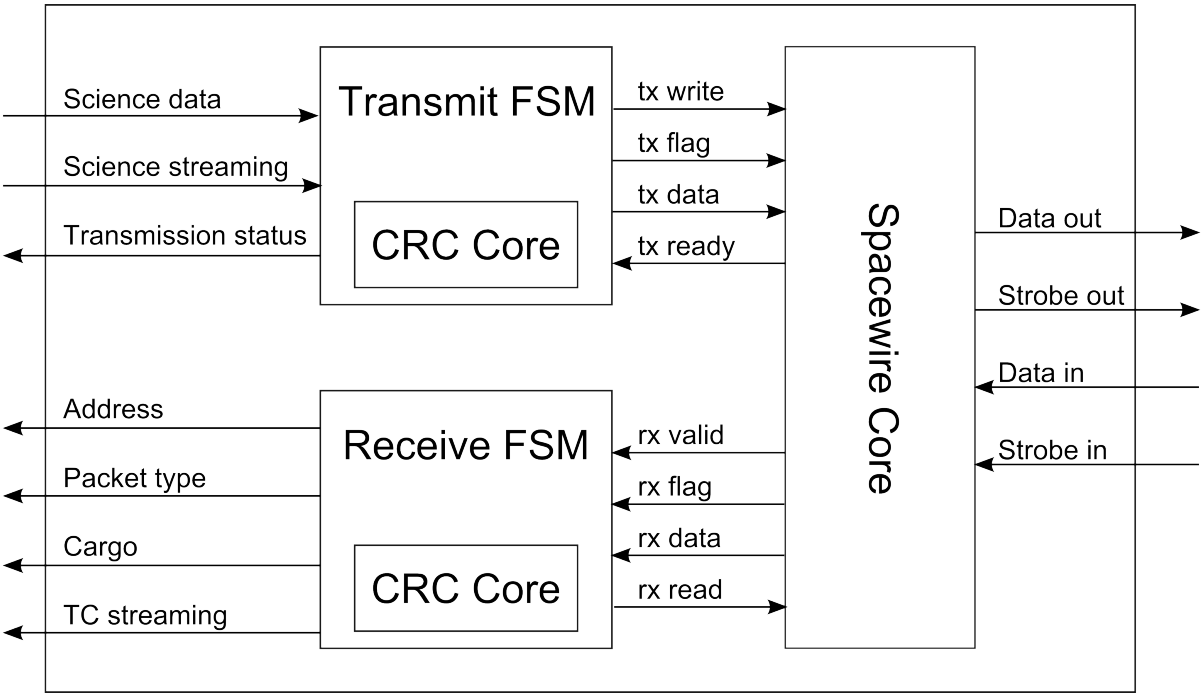


**Figure 4.11:** This figure illustrates the signal flow inside the Communication Unit. Communication with the DHU is performed by the use of the data and strobe signals on the right hand side of the figure. The signals on the left hand side establish the receiving and transmission of data by the BEE side. Both the receiving and the transmitting of data are handled by a separate FSM, which is connected to the according signal lines of the SpaceWire core. The implementation of two CRC cores allows the independent performing of CRC checks during the simultaneous transmission and receiving by these FSM.

The transmission of data from the BEE to the DHU and the receiving of commands of the BEE from the DHU are handled by the CU totally independently. Both the transmission and the receiving have a separate finite state machine (FSM).

### Transmitting data

To send data from the BEE to the DHU, the BEE first has to check the CU's transmission status signal. If the first bit of the signal is high, that indicates, that the CU is ready to transmit a new data packet to the DHU. Vice versa it is set low, when there is an ongoing transmission. The BEE then sets the first bit of the science streaming signal high to start a transmission. This bit stays high until all the cargo of the packet has been transmitted. If the second bit of the transmission status is high, then the CU is

ready to accept a new byte for transmission. In response the BEE sets the second bit of the science streaming signal high for one clock cycle, to indicate that the science data byte is ready to be transmitted. This data byte is sent to the DHU by the FSM via the SpaceWire core. This procedure repeats until the complete packet except the CRC byte has been sent and the first bit of the science streaming signal is set to low. The CU has a separate CRC core for the transmission and the receiving of data. Each transmitted byte is automatically included in the calculation of the CRC check sum. When the transmission of the data by the BEE ends, the CRC byte transmitted to the DHU is succeeded by an EOP token. The CU is now ready to accept a new data packet and the first bit of the transmission status is set high again.

### Receiving data

The receiving of data from the DHU by the CU is again handled by its own FSM. Based on the telemetry structure, the CU recognizes the first byte as the target address, the second byte as the packet type and the third and fourth bytes as the length of the cargo. The CU sets the first bit of the TC streaming signal high until the complete packet is received. Every time a new valid cargo byte is ready, the second bit of the TC streaming is set high for one clock cycle and stays low otherwise. The CU identifies the CRC byte by knowing the total length of the cargo and checks for validity of the received data using its CRC core. The CRC byte is not processed to the BEE. A received EOP token ends the streaming process and the first byte of TC streaming is set to zero. The ability to send resend requests to the DHU on receiving an EEP or an invalid CRC check is already included, however the format of such a request and the reaction of the BEE is still unclear. If the recognition of an invalid packet should occur while the CU is transmitting data to the DHU, the CU will complete the ongoing transmission and send the request afterward.

This treatment of the communication of the BEE and the DHU concludes the current chapter. Chapter 5 will continue with the discussion of the achieved results, while Chapter 6 will give an outlook on future works, improvements and open questions concerning the BEE.

# Chapter 5

# Results

This chapter treats the results of this diploma thesis. It will first address the results concerning the SpaceWire interface between BEE and DHU and continue with the results achieved for the event reconstruction.

## 5.1 Results for the SpaceWire interface

One of the tasks of this thesis was the implementation of a SpaceWire interface to communicate with the DHU. The created solution covers the following points:

- For the SpaceWire interface the separate CU was created. This unit established a SpaceWire connection to the DHU and is able to transmit as well as receive data. It is embedded in the BEE and was discussed in Subsection 4.5.2.
- The CU uses the SpaceWire Light core developed by van Rantwijk 2010.
- The CU includes a CRC functionality to automatically calculate and append the CRC check sum for the transmission of data and the CU thus respectively uses this functionality to check the correctness of received data. The CRC core used was developed by Drange 2005.
- Data packets received by the CU from the DHU are broken down into the target address, the packet type and the included cargo. The packets therefore have to stick to the telemetry structure discussed in Section 4.5.2
- Since there was no DHU counterpart available to test the BEE's CU in hardware, a connection to the PC was established using the SpaceWire-USB Brick from StarDundee. Transmission, receiving, the CRC functionality and the deciphering of received commands worked without problems. In a first test transmission rates of $\sim 8\,\mathrm{Mbit\ s^{-1}}$ were achieved. While this is sufficient for the normal science mode, this has to be tested for the case of GRBs.

## 5.2 Results for the event reconstruction

In order to test the quality of the reconstruction of the event on the detector plane, simulation data was required. In a first step Yuri Evangelista from the LOFT consortium simulated the shadow pattern on a WFM camera created by a fictional source in the sky. Slawomir Suchy of the Institute for Astronomy and Astrophysics Tuebingen used the simulated event distribution to create the resulting charge distribution on the anodes of the SDDs for each incident photon. He added a pedestal value, a gain factor and random fluctuation to simulate noise to each single anode and a common mode to all of the anodes. The resulting data was handed to the Data Processing Unit (DPU) in a way similar to the output of the Detector Handling Unit. The data was then processed in the science mode and the event's energy, driftposition and fineposition were reconstructed. The reconstructed values were then compared to the original values, from which the charge distribution on the anodes was created. Since the single units of the DPU could not always treat the quantities with full precision due to the needed hardware resources and due to the limitations of the used division cores in bit size, a software tool for the reconstruction was created using C++. This software tool applies the same corrections and uses the same reconstruction algorithms, but treats the results with full precision. The results of the software based reconstruction was then again compared to the initial event's data. The results of the hardware based reconstruction and the results of the software based reconstruction are compared in the following figures to give a feeling for the quality of the reconstruction algorithm and of the quality loss due to the limitations in bit size.

A total number of 1678 data sets for incident photons were used for the simulation. This number did not allow to perform a more detailed analysis, e.g. by subdividing the events into different energy bands. The results presented in the following figures therefore have no claim of giving a quantitative statement, but to provide some qualitative insights in the level of accuracy, that can be achieved. Figure 5.1 shows the results for the energy reconstruction, Figure 5.2 shows the results for the reconstruction of the driftposition and Figure 5.3 shows the results achieved for the reconstruction of the fineposition.

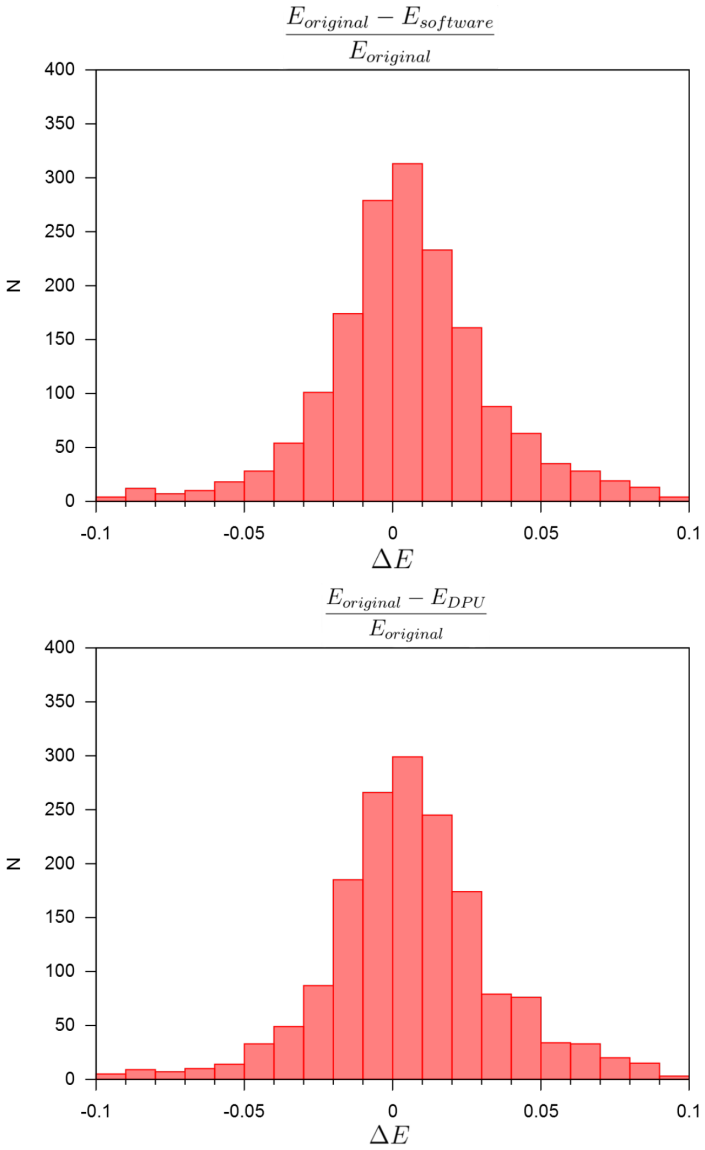


**Figure 5.1:** These figures show the results of the energy reconstruction. The top figure shows the results for the computer simulated reconstruction and the bottom figure for the reconstruction by the DPU. There is a good agreement between both results. However both figures could only show quantitative results, if the energy resolution was a linear function of the energy. That is not the case and therefore the figures give only a qualitative result and no Gaussian function is fitted. For a more quantitative discussion of the results, the initial events would have to be subdivided in different energy bands, which would then be analyzed separately, however more data sets would be required. The goal for the achieved energy resolution is 300 eV at 6 keV for 1 σ accuracy, which is equal to 5 % at 6 keV. The DPU seems to be on a good way to meet these requirements.

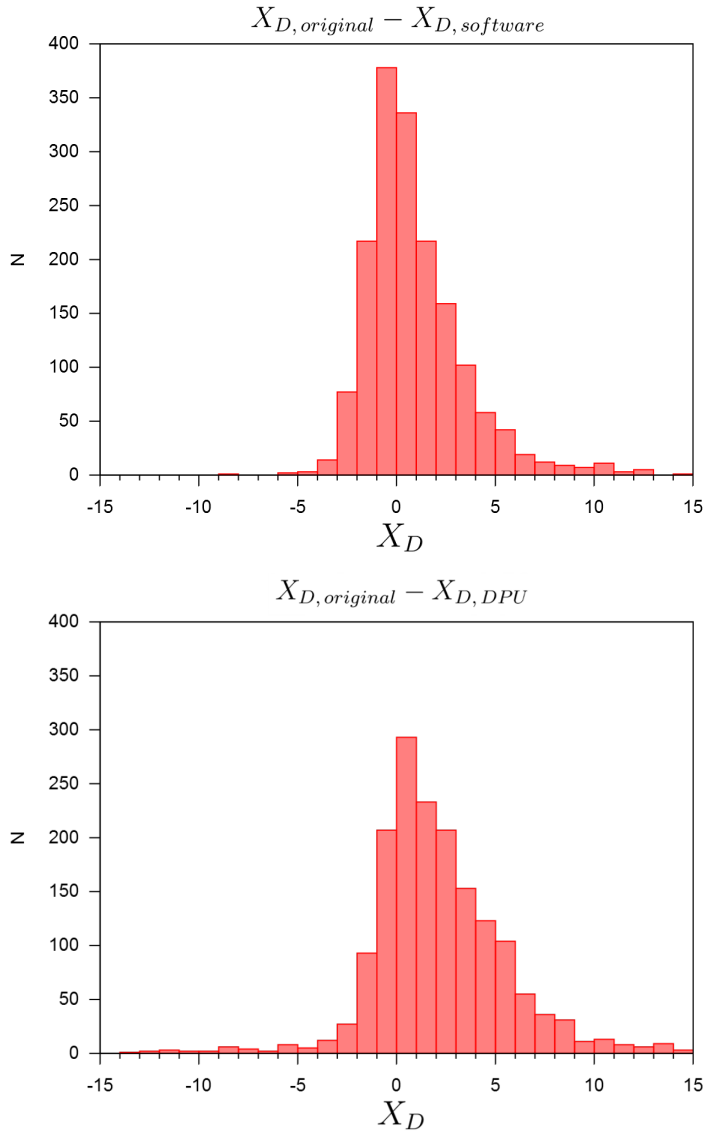


**Figure 5.2:** This figure illustrates the results that were achieved for the reconstruction of the driftposition. The top figure was created using the results of the reconstruction by software, while the bottom figure used results achieved by the hardware. It is easy to see, that the results of the software are better that the results of the DPU. This is a consequence of the fact, that the driftposition is reconstructed at the very end of the chain of corrections and reconstructions performed by the DPU and the propagation of the involved errors. Another error is induced by the limitation of the used divider cores to a size of 23 bit for the divisor. The contribution of this error could be minimized by putting harder constraints on the size of the correction factors, i.e. the temperature correction's resolution or the gain factor's resolution.
The targeted resolution in driftdirection is $X_\mathrm{D} < 7\,\mathrm{mm}$ for $1\,\sigma$ accuracy and again the DPU seems to meet these requirements.

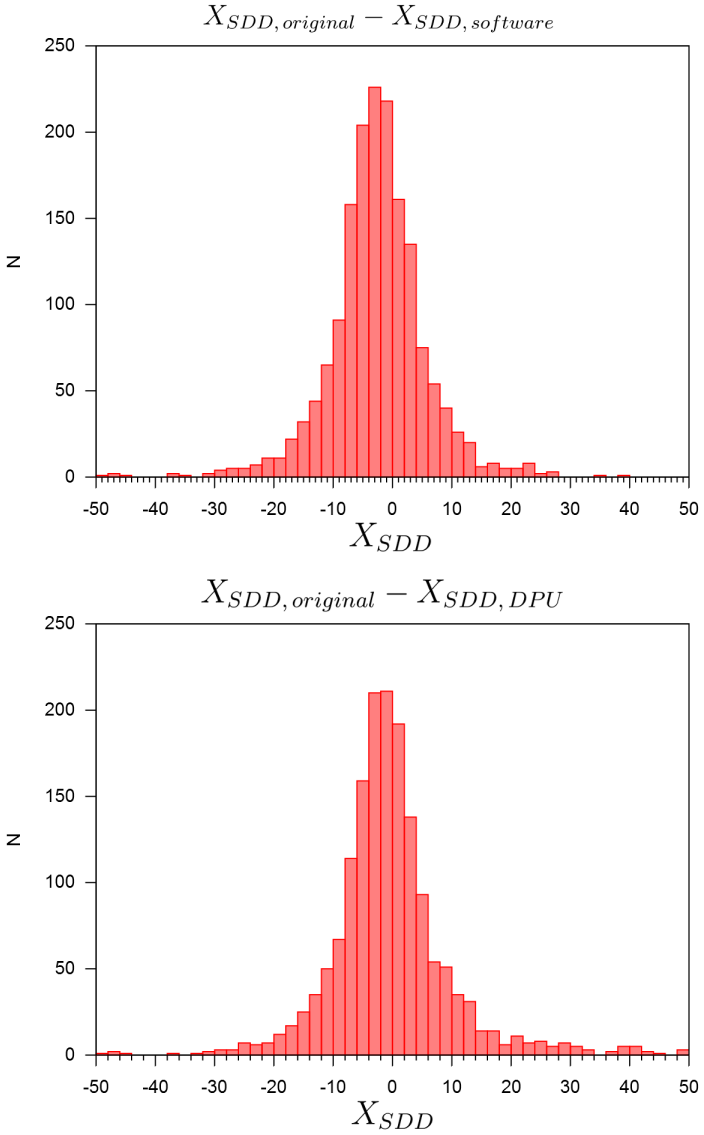


**Figure 5.3:** The top figure shows the reconstruction of the incident photon's position in fineposition as performed by the software, while the bottom figure shows the same performed by the DPU. There is a very good agreement between both figures and both figures seem to fulfill the requirement of $\Delta X_{\mathrm{SDD}} < 30\,\mu\mathrm{m}$ for $1\,\sigma$ accuracy very well.

### 5.2.1 Resource requirements

This subsection discusses the demand of hardware logic components needed for the instantiation of one DPU in its current version. The results for the resource requirements must be understood as qualitative results, similar to the results in the previous section. If the VHDL code is compiled and an output file that can actually be loaded into the FPGA is generated, the compiler (in this case the Xilinx ISE Project Navigator) creates an electronics design based on the VHDL code. The compiler therefore tries to minimize the amount of resources used (i.e. LUTs, flipflops, DSP cores, ...), while at the same time it tries to fulfill the timing constraints (i.e. the signal run time between components has to be less than the time for a clock cycle). The amount of resources used does thus not scale linear with the number of DPUs used.
In the current version, the DPU uses too much resources to be instantiated the needed eight times. Table 5.1 list the resource requirements for the implementation of a DPU and its components on a Virtex4 XC4VFX100 FGPA. The demand of the PDU is listed in total, while the detailed demand of its separate components is listed below, followed by the percentage of the used resources of the correspondent type of the total resources, that the FPGA can provide. The driving point for the resource demand are the Common Mode Unit (CMU), the Fineposition Reconstruction (FPR) and the Driftposition Reconstruction (DPR). The heavy use of logic components by the CMU can be explained with the need to temporally store all the 64 anode values of one ASIC twice (once in their original order and once sorted by size for the calculation of the median) and with the use of compare logic, to sort the anodes. The heavy demand for resources of the FPR and the DPR is a result of the multiplications and especially of the divisions needed to calculate the position of the event. Ideas to reduce the size of the PDU are discussed in Subsection 5.2.2. With the DPU yet consuming too much resources to be instantiated eight times (one DPU for each SDD) and since the signal flow between CU and DPU is not yet completely established, the resource consumption could only be tested for separate PDUs and does therefore only provide qualitative insights. However with the ideas to reduce the resource demand introduced in Subsection 5.2.2, a fitting size for the PDU should be in reach.

| Unit name | Slices | Slice Reg. | LUTs | LUT RAM | DSP48 |
|---|---|---|---|---|---|
| DPU | 9748 | 10185 | 12926 | 252 | 7 |
| Pipeline even | 2356 | 1295 | 4318 | 62 | 2 |
| CMU | 2083 | 951 | 3970 | 56 | 0 |
| Gain Unit | 61 | 33 | 46 | 0 | 2 |
| ERU | 85 | 120 | 165 | 0 | 0 |
| Pipeline odd | 2367 | 1295 | 4322 | 62 | 2 |
| CMU | 2095 | 951 | 3974 | 56 | 0 |
| Gain Unit | 61 | 33 | 46 | 0 | 2 |
| ERU | 85 | 120 | 165 | 0 | 0 |
| DPR | 2519 | 3817 | 1975 | 47 | 2 |
| FPR | 2219 | 3271 | 2094 | 22 | 1 |
| Total demand | 22% | 12% | 15% | 1% | 4% |

**Table 5.1:** Resource demand of one DPU. The columns show the demand in Slices, Slice Registers, Look Up Tables (LUTs), LUT based Random Access Memory (RAM) and DSP48 logic. The second row shows the demand for the DPU in total, while the rows below show the demand of its itemized components. The entries for both pipelines too show the demand of the total pipeline and their itemized components are listed below. The last row shows the percentage of the total resources, that the FPGA can provide, which is used for the DPU.
The used abbreviations are: Data Processing Unit (DPU), Common Mode Unit (CMU), Energy Reconstruction Unit (ERU), Driftposition Reconstruction (DPR), Fineposition Reconstruction (FPR)

### 5.2.2 Possible improvements

There are several possible improvements for the BEE. This includes chances to reduce the required resources, to improve the accuracy of the position reconstruction and the rate for data transmission.

- The largest potential for improvements is without a doubt to put harder constraints on different parameters. By putting constraints on the possible range and the provided accuracy of parameters, the number of bits needed to represent these parameter can be drastically reduced. This is especially important, since multiplicative corrections, e.g. the gain correction, lead to a massive increase in the possible size of the result, if there are no hard constraints on the multiplication factor. This does not only lead to an increase in the overall demand of resources, but in a possible decrease of the possible accuracy of the reconstructed result, since the unnecessarily used bits for the anodes propagate through the successive units in the DPU. The functional cores used in this design for the division in the FPGA, are limited to a total length of 23 bit for the divider and thus some of the least significant bits have to be ignored in the calculation. If the total number of bits needed to represent the total energy and the charge induced in one anode is reduced, then less bits have to be ignored in the calculation. The first approach to reduce the demand for resources should thus be to put harder constraints on the parameters and adjust the code respectively.

- The sorting algorithm used in the Common Mode Unit (CMU) includes some potential in resource reduction. While the used algorithm is the fasted solution for sorting in hardware, it also uses lots of logic components. Because of the bit by bit transmission of the anode values from the FEE to the BEE, there should be at least 11 clock cycles between each valid anode on the input of the CMU. Thus a different sorting algorithm could decrease the amount of needed logic components. The total time for the calculation of the common mode would increase by a few clock cycles, since the last anode of the ASIC requires sorting too. This delay however should be negligible compared to the total run time of the DPU. This possibility of resource reduction should especially be considered, since the CMU is part of the pipeline, which is instantiated twice in each DPU.

- It was already discussed above, that the reconstruction of the fineposition and especially the reconstruction of the driftposition use lots of resources due to the necessary multiplications and divisions. While some multiplication cores already use DSP logic, the division cores yet use slice logic. The reason for this is, that division with DSP logic needs some special algorithms, while the division with cores using slice logic is straight forward. It has to be tested if it is best to replace all division cores by DSP logic or if this would just shift the resource problem from

slice logic to DSP logic. The Virtex4 also includes so-called XtremeDSP 48 slices, which could be used for multiplications.

- The transmission rate achieved with the SpaceWire core of the Communication Unit (CU) is 8 Mbit $s^{-1}$. This is thought to be sufficient and thus there was no try for further improvements. If however this transmission rate should prove to be insufficient, there is the possibility to switch to a faster transmission mode. The CU uses the standard generic working mode for a clock synchronous transmitting and receiving of data, which limits the maximum bit rate to be half of the system clock (which is in our case estimated to be 50 MHz). The SpaceWire core can also be used in a faster working mode. For more details read the SpaceWire Light manual by van Rantwijk 2010.

### 5.2.3 Open tasks

While the main components of the functionality of the BEE were developed in the frame of this thesis, other functionalities must still be included. These open tasks are:

- The configuration and engineering mode described in Section 4.3. The only functional working mode yet is the science mode, which is also the basic working mode for the BEE. The configuration mode and the engineering mode have still to be included, however the detailed functionality of these modes has yet to be defined. The basics for future options such as the possibility to update the correction factors stored in the RAM are already included.
- The transformation to global camera coordinates. While this transformation should be easy to include, the details for this transformation have yet to be developed. This includes the representation of the position in bit in such way, as to avoid losses in the possible resolution due to the non-sensitive area between the SDDs.
- The development of a functional Detector Handling Unit. This should be quite easy, since the functionality of the FEE is the same for the WFM and the LAD. A functional Detector Handling Unit for the LAD has already been developed. Minor changes will have to be applied, including the output of the ID of the triggered ASIC for the position reconstruction and the synchronous output of the anode values of two ASICs. The Detector Handling Unit should already possess the necessary data, but the output has to be modified.
- The realization of a hardware prototype. The complete design of the BEE as developed in this diploma thesis was only tested in software, with the exception of the SpaceWire interface to the DHU, which tested in a Spartan3 FPGA with a PC simulating the DHU. First however the design of the DPU has to be reduced in size.

# Chapter 6

# Conclusion and outlook

A prototype of the VHDL BEE design for the WFM instrument was developed in the frame of this diploma thesis. A functional SpaceWire interface between the BEE and the DHU was established, including CRC8 error recognition, automatic resend requests in case of transmission failures and itemization of the different components included in commands, such as the address, the packet type and the cargo. The communication between BEE and DHU was simulated in hardware by an established connection between BEE and a PC using a SpaceWire brick and a data transmission rate of ~8 Mbit $s^{-1}$ was achieved, which can be increased as described in Section 5.2.2.
A Data Processing Unit was developed, which applies pedestal, common mode and gain corrections to the event data received from the FEE, and which reconstructs the energy and the position of the incident photon in fine direction as well as in drift direction. The achieved results for the reconstruction of the initial event were compared to results calculated with the same algorithm at full precision as described in Section 5 using a software tool, which was developed for this purpose. While these results all were of qualitative nature, they seem to be very well above the required accuracy. The only limiting factor, which prevented the implementation of all eight PDUs, was the demand for hardware resources. However ideas to overcome these limits and ideas for other possible improvements in the design were introduces in Section 5.2.2. While there are still some minor tasks open as described in Section 5.2.3, this prototype already includes the largest and most important parts of the BEE's functionality. It can be concluded, that this diploma thesis showed the feasibility of the WFM BEE as well as proved the quality of the reconstruction algorithm used.

The future for the LOFT mission however is still unclear. While LOFT has not been down-selected for launch within the M3 call, its science goals were fully recognized as very strong, the mission suitable to address them and based on the assessment study, the resulting Yellow Book and more than 3000 pages of technical documentation, its technology was evaluated as very mature. The LOFT consortium therefore announced its intention to continue the development aiming now at the upcoming M4 ESA launch in 2026.

# Danksagung

Nach über einem Jahr am Institut hat die Liste derer, bei denen ich mich bedanken will, doch eine beträchtliche Länge erreicht. Wenn ich mich im Rahmen dieser Seite leider nur auf eine kleine Auswahl dieser Personen begrenzen kann, so danke ich doch ausdrücklich auch all jenen Unerwähnten, die mich in meiner Zeit am Institut begleiteten.

Zuerst möchte ich mich bei **Prof. Dot. Andrea Santangelo** für die lehrreichen Vorlesungen während des Studiums, welche mein Interesse an der Astronomie weckten, bedanken sowie für die Möglichkeit meine Diplomarbeit am Institut verfassen zu können. Mein größter Dank gilt **Dr. Christoph Tenzer** und **Thomas Schanz** für die viele Zeit, die ihr euch für mich genommen habt, und die stetige Unterstützung bei Problemen. Eure Hilfe hat nicht nur meine Zeit am Institut positiv geprägt, sondern auch meine berufliche Zukunft. Ganz besonders bedanken will ich mich auch bei meinen Bürokollegen **Daniel Maier**, **Henning Wende** und **Sabina Pürckhauer**. Ihr wart stets für Fragen und interessante Diskussionen offen und ihr habt dafür gesorgt, dass ich gerne ins Büro gekommen bin. Danke dafür. Mein Dank gilt auch **Dr. Slawomir Suchy**, der während seiner Zeit am Institut immer für Auskünfte zur Verfügung stand und sich auch darüber hinaus für meine Arbeit interessierte. Speziell erwähnen will ich auch noch all jene Leute, die Aktivitäten über das reine Studium hinaus möglich gemacht haben. Das wären das **Irish Quiz Team**, die **Fußballrunde**, die **Crew des Segeltörns** und natürlich meine **Mitläufer**. Euch allen wünsche ich alles Gute für die Zukunft und auch wenn meine Zeit am IAAT nun zu Ende ist, so hoffe ich doch, dass der Kontakt erhalten bleibt. Den Grundstein dafür habe ich jedenfalls bereits gelegt und mir meinen Platz auf dem Fußballverteiler schon für die Zukunft gesichert.

Mit dieser Diplomarbeit geht nicht nur meine Zeit am IAAT zur Neige, sondern sie beendet auch mein Studium an der Universität Tübingen. Daher will ich mich zum Schluss noch bei all jenen bedanken, die zum Gelingen dieses Studiums beigetragen haben, die meine Launen ertragen mussten, wenn es gerade einmal wieder nicht so gut lief, und die mich die Uni auch einfach mal Uni sein ließen. Mein Dank gilt **meinen Eltern** und meinem **Bruder**, die mir das Studium ermöglichten und mir den nötigen Halt gaben, meiner ganzen **Familie**, die sich immer für meine Arbeit interessierte, meinen **Kommilitonen**, die mich während des Studium begleiteten und dies darüber hinaus auch in Zukunft tun werden, meinen **Freunden**, die mich in meinen Vorhaben bestärkten und auf die ich jederzeit zählen konnte, und nicht zuletzt meiner **Freundin**, die mich die ganzen letzten Jahre aushalten musste und trotzdem immer für mich da war.

# Appendix

**Table 1:** IO signals of the DPU.

| Signal name | Port | Length in bit | Description |
|---|---|---|---|
| **Global signals** | | | |
| rst | in | 1 | Synchronous reset |
| clk | in | 1 | Common clock |
| **Configuration signals** | | | |
| working_mode | in | 2 | One of four possible working modes |
| configuration_address_in | in | 9 | RAM address for the configuration data |
| configuration_gain_data_in | in | 13 | Gain correction factor to store in RAM at given address |
| configuration_pedestal_data_in | in | 12 | Pedestal correction factor to store in RAM at given address |
| configuration_gain_valid | in | 1 | High if gain correction factor valid |
| configuration_pedestal_valid | in | 1 | High if pedestal correction factor valid |
| **Science signals** | | | |
| fine_position | out | 16 | Fineposition output |
| drift_position | out | 8 | Driftposition output |
| energy | out | 16 | Energy output |
| timestamp | out | 24 | Timestamp output |
| science_valid | out | 1 | High if fineposition, driftposition and energy are valid |

**Table 2:** IO signals of the Detector Handling Unit

| Signal name | Port | Length in bit | Description |
|---|---|---|---|
| **Global signals** | | | |
| rst | in | 1 | Synchronous reset |
| clk | in | 1 | Common clock |
| timestamp_reset | in | 1 | Reset for timestamp |
| **Communication with ASIC** | | | |
| trigger_in | in | 1 | trigger signal from ASICs |
| data_odd | in | 1 | Data line odd |
| data_even | in | 1 | Data line even |
| command_out_even | out | 1 | Command line even |
| command_out_odd | out | 1 | Command line odd |
| to_ASIC_reset | out | 1 | Reset ASICs |
| **Communication with DPU** | | | |
| data_from_TL | in | variable | Data from top level. E.g. callibration data |
| command_enabled | in | 1 | High if command data on data_from_TL |
| idle | out | 1 | High if ready to accept data |
| solid_send | out | 1 | |
| anodes_valid | out | 1 | High if anodes valid |
| anode_even_out | out | 12 | Anode from even ASIC |
| anode_odd_out | out | 12 | Anode from odd ASIC |
| asic_id_even | out | 3 | Number of even ASIC |
| asic_id_odd | out | 3 | Number of odd ASIC |
| ids_valid | out | 1 | High if Numbers valid |
| timestamp | out | 24 | Timestamp |

**Table 3:** IO signals of the pipeline.

| Signal name | Port | Length in bit | Description |
|---|---|---|---|
| **Global signals** | | | |
| rst | in | 1 | Synchronous reset |
| clk | in | 1 | Common clock |
| **Communication with PDU RAM** | | | |
| ram_ped_anodenumber | out | 6 | Number of the next anode on the ASIC for the pedestal correction |
| ram_pedestal | in | 12 | Pedestal value for the next anode |
| ram_gain_anodenumber | out | 6 | Number of the next anode on the ASIC for the gain correction |
| ram_gainfactor | in | 13 | Gain factor for the next anode |
| **Input signals** | | | |
| anode_in | in | 12 | Anodes handed from Detector Handling Unit to pipeline_shell |
| enabled | in | 1 | High if anode_in is valid |
| **Output signals** | | | |
| anode_out | out | 27 | Anode output is full precision |
| anode_number_out | out | 6 | Number of anode on ASIC for position reconstruction |
| valid_anode | out | 1 | High if anode output is valid |
| energy | out | 31 | Energy output in full precision |
| valid_energy | out | 1 | High if energy output is valid |

**Table 4:** IO signals of the Common Mode Unit.

| Signal name | Port | Length in bit | Description |
|---|---|---|---|
| **Global signals** | | | |
| rst | in | 1 | Synchronous reset |
| clk | in | 1 | Common clock |
| **Input signals** | | | |
| enabled | in | 1 | High if anode is valid |
| anode | in | 14 | Pedestal corrected anode |
| **Output signals** | | | |
| valid | out | 1 | High if anode_cm_corrected is valid |
| anode_cm_corrected | out | 14 | Common mode corrected anode |

**Table 5:** IO signals of the Gain Unit.

| Signal name | Port | Length in bit | Description |
|---|---|---|---|
| **Global signals** | | | |
| rst | in | 1 | Synchronous reset |
| clk | in | 1 | Common clock |
| **Input signals** | | | |
| enabled | in | 1 | High if anode is valid |
| anode | in | 14 | Common mode corrected anode |
| gain | in | 13 | The gain correction factor |
| temp_correction | in | 10 | Temperature dependent correction factor, i.e. $\Delta T = T - \mathrm{T}_0$ |
| **Output signals** | | | |
| valid | out | 1 | High if anode_gain_corrected is valid |
| anode_gain_corrected | out | 28 | Gain corrected anode |

**Table 6:** IO signals of the Energy Reconstruction.

| Signal name | Port | Length in bit | Description |
|---|---|---|---|
| **Global signals** | | | |
| rst | in | 1 | Synchronous reset |
| clk | in | 1 | Common clock |
| **Input signals** | | | |
| enabled | in | 1 | High if anode_in is valid |
| anode_in | in | 28 | Gain corrected anode |
| **Output signals** | | | |
| valid | out | 1 | High if anode_out is valid |
| anode_out | out | 27 | Anode output, already considered for the reconstruction of the energy |
| energy_valid | out | 1 | High if total energy is valid |
| energy_out | out | 31 | Total energy of the event on the deposed in the ASIC |

**Table 7:** IO signals of the Fineposition Reconstruction Unit.

| Signal name | Port | Length in bit | Description |
|---|---|---|---|
| **Global signals** | | | |
| rst | in | 1 | Synchronous reset |
| clk | in | 1 | Common clock |
| **Input signals** | | | |
| energy | in | 31 | Total energy of the event |
| energy_enabled | in | 1 | High if energy is valid |
| anode_even | in | 27 | Anode from even ASIC |
| anode_number_even | in | 9 | Number of anode_even on the ASIC |
| enabled_even | in | 1 | High if anode_even is valid |
| anode_odd | in | 27 | Anode from odd ASIC |
| anode_number_odd | in | 9 | Number of anode_odd on the ASIC |
| enabled_odd | in | 1 | High if anode_odd is valid |
| **Output signals** | | | |
| anode_out | out | 27 | Anode output |
| anode_out_number | out | 9 | Number of anode_out on the ASIC |
| anode_out_valid | out | 1 | High if anode_out is valid |
| energy_out | out | 23 | Total energy of the event |
| fine_position_out | out | 16 | Fineposition of the event |

**Table 8:** IO signals of the Driftposition Reconstruction Unit.

| Signal name | Port | Length in bit | Description |
|---|---|---|---|
| **Global signals** | | | |
| rst | in | 1 | Synchronous reset |
| clk | in | 1 | Common clock |
| **Input signals** | | | |
| energy_in | in | 23 | Total energy of the event |
| anode_in | in | 27 | Anode from even ASIC |
| anode_in_number | in | 9 | Number of anode_in on the ASIC |
| anode_in_enabled | in | 1 | High if anode_in is valid |
| fine_position_in | in | 16 | Fineposition of the event |
| temperature | in | 11 | Temperature of the detector |
| **Output signals** | | | |
| energy_out | out | 16 | Total energy of the event |
| fine_position_out | out | 16 | Fineposition of the event |
| drift_position_out | out | 8 | Driftposition of the event |
| output_valid | out | 1 | High if output is valid |

**Table 9:** IO signals of the Communication Unit.

| Signal name | Port | Length in bit | Description |
|---|---|---|---|
| **Global signals** | | | |
| rst | in | 1 | Synchronous reset |
| clk | in | 1 | Common clock |
| **Spacewire signals** | | | |
| spw_di | in | 1 | Data in signal for the SpaceWire core |
| spw_si | in | 1 | Strobe in signal for the SpaceWire core |
| spw_do | out | 1 | Data out signal for the SpaceWire core |
| spw_so | out | 1 | Strobe out signal for the SpaceWire core |
| **BEE to DHU communication signals** | | | |
| science_data | in | 8 | Data packet for transmission |
| science_streaming | in | 2 | First bit: High as long as data belongs to the same packet<br>Second bit: High for one clock cycle when science_data is valid |
| transmission_status | out | 2 | First bit: High if ready to accept new streaming of a data packet<br>Second bit: High if ready to accept a new science_data byte of the packet |
| **DHU to BEE communication signals** | | | |
| address | out | 8 | Address of the received packet |
| packet_type | out | 8 | Packet type of the received packet |
| cargo | out | 8 | Current received cargo byte |
| tc_streaming | out | 2 | First bit: High as long as data belongs to the same packet<br>Second bit: High for one clock cycle when cargo byte is valid |

# List of Figures

# List of Tables

# Bibliography


Altamirano, D. et al. (2008). "Intermittent Millisecond X-Ray Pulsations from the Neutron Star X-Ray Transient SAX J1748.9-2021 in the Globular Cluster NGC 6440". In: ApJ 674, pp. L45–L48. DOI: 10.1086/528983. arXiv: 0708.1316.

Balman, S. (2014). "Inner Disk Structure of Dwarf Novae in the Light of X-ray Observations". In: *ArXiv e-prints*. arXiv: 1403.4437 [astro-ph.HE].

Barret, D. et al. (2013). *The Large Observatory for X-ray Timing, Assessment Study Report*. Tech. rep. European Space Agency.

Barthelmy, S. D. et al. (2005). "The Burst Alert Telescope (BAT) on the SWIFT Midex Mission". In: Space Sci. Rev. 120, pp. 143–164. DOI: 10.1007/s11214-005-5096-3. eprint: astro-ph/0507410.

Barucci, M. et al. (2013). *MarcoPolo-R, Assessment Study Report*. Tech. rep. European Space Agency.

Bauböck, M. et al. (2013). "Relations between Neutron-star Parameters in the Hartle-Thorne Approximation". In: ApJ 777, 68, p. 68. DOI: 10.1088/0004-637X/777/1/68. arXiv: 1306.0569 [astro-ph.HE].

Bednarek, I. et al. (2012). "Hyperons in neutron-star cores and a 2 $M_{\hat{a}\check{S}TM}$ pulsar". In: A&A 543, A157, A157. DOI: 10.1051/0004-6361/201118560. arXiv: 1111.6942 [astro-ph.SR].

Bode, M. F. et al. (2006). "Swift Observations of the 2006 Outburst of the Recurrent Nova RS Ophiuchi. I. Early X-Ray Emission from the Shocked Ejecta and Red Giant Wind". In: ApJ 652, pp. 629–635. DOI: 10.1086/507980. eprint: astro-ph/0604618.

Bongs, K. et al. (2013). *STE-QUEST, Assessment Study Report*. Tech. rep. European Space Agency.

Bošnjak, Ž., F. Daigne, and G. Dubus (2009). "Prompt high-energy emission from gamma-ray bursts in the internal shock model". In: A&A 498, pp. 677–703. DOI: 10.1051/0004-6361/200811375. arXiv: 0811.2956.

Brandt, S. (2012). *LOFT Wide Field Monitor LOFT Burst Alert System*. Tech. rep. European Space Agency.

Brandt, S. et al. (2012). "The LOFT wide field monitor". In: *Society of Photo-Optical Instrumentation Engineers (SPIE) Conference Series*. Vol. 8443. Society of Photo-Optical Instrumentation Engineers (SPIE) Conference Series. DOI: 10.1117/12.926060. arXiv: 1209.1499 [astro-ph.IM].

Campana, R. et al. (2011). "Imaging performance of a large-area Silicon Drift Detector for X-ray astronomy". In: *Nuclear Instruments and Methods in Physics Research Section A: Accelerators, Spectrometers, Detectors and Associated Equipment* 633.1, pp. 22 –30. ISSN: 0168-9002. DOI: http://dx.doi.org/10.1016/j.nima.2010.12.237.

Casella, P. et al. (2008). "Discovery of Coherent Millisecond X-Ray Pulsations in Aquila X-1". In: ApJ 674, pp. L41–L44. DOI: 10.1086/528982. arXiv: 0708.1110.

Chaty, S. (2012). "An INTEGRAL view of High Mass X-ray Binaries : their nature, formation and evolution". In: *Proceedings of "An INTEGRAL view of the high-energy sky (the first 10 years)" - 9th INTEGRAL Workshop and celebration of the 10th anniversary of the launch (INTEGRAL 2012). 15-19 October 2012*. arXiv: 1302.4195 [astro-ph.HE].

– (2013). "Optical/infrared observations unveiling the formation, nature and evolution of High-Mass X-ray Binaries". In: *Advances in Space Research* 52, pp. 2132–2142. DOI: 10.1016/j.asr.2013.09.010. arXiv: 1403.0792 [astro-ph.HE].

Crescio, E. and D. Nouais (2006). "Electron cloud size measurement in silicon drift detectors and spatial resolution improvement". In: *Nuclear Instruments and Methods in Physics Research Section A: Accelerators, Spectrometers, Detectors and Associated Equipment* 564.1, pp. 475 –481. ISSN: 0168-9002. DOI: http://dx.doi.org/10.1016/j.nima.2006.04.077.

Daigne, F., Ž. Bošnjak, and G. Dubus (2011). "Reconciling observed gamma-ray burst prompt spectra with synchrotron radiation?" In: A&A 526, A110, A110. DOI: 10.1051/0004-6361/201015457. arXiv: 1009.2636 [astro-ph.HE].

Dauser, T. et al. (2010). "Broad emission lines for a negatively spinning black hole". In: MNRAS 409, pp. 1534–1540. DOI: 10.1111/j.1365-2966.2010.17393.x. arXiv: 1007.4937 [astro-ph.HE].

Drange, G. (2005). "Ultimate CRC".

Drossart, P. et al. (2013). *EChO, Assessment Study Report*. Tech. rep. European Space Agency.

European Space Agency (2008). *ECSS-E-ST-50-12C*. Tech. rep. European Space Agency.

Feroci, M. et al. (1998). "BeppoSAX follow-up search for the X-ray afterglow of GRB970111". In: A&A 332, pp. L29–L33. eprint: astro-ph/9803015.

Feroci, M. et al. (2012). "The Large Observatory for X-ray Timing (LOFT)". In: *Experimental Astronomy* 34, pp. 415–444. DOI: 10.1007/s10686-011-9237-2. arXiv: 1107.0436 [astro-ph.IM].

Galama, T. J. et al. (1998). "An unusual supernova in the error box of the $\gamma$-ray burst of 25 April 1998". In: Nature 395, pp. 670–672. DOI: 10.1038/27150. eprint: astro-ph/9806175.

Gálvez, J. L. et al. (2013). "The WFM Instrument of the LOFT mission". In: *Highlights of Spanish Astrophysics VII*, pp. 886–891.

Gatti, E. and P. Rehak, eds. (1983). *Semiconductor drift chamber: An application of a novel charge transport scheme*.

Gehrels, N., E. Ramirez-Ruiz, and D. B. Fox (2009). "Gamma-Ray Bursts in the Swift Era". In: ARA&A 47, pp. 567–617. DOI: 10.1146/annurev.astro.46.060407.145147. arXiv: 0909.1531 [astro-ph.HE].

Giacconi, R. et al. (1962). "Evidence for x Rays From Sources Outside the Solar System". In: *Physical Review Letters* 9, pp. 439–443. DOI: 10.1103/PhysRevLett.9.439.

Giannios, D. (2008). "Prompt GRB emission from gradual energy dissipation". In: A&A 480, pp. 305–312. DOI: 10.1051/0004-6361:20079085. arXiv: 0711.2632.

Gold, T. (1968). "Rotating Neutron Stars as the Origin of the Pulsating Radio Sources". In: Nature 218, pp. 731–732. DOI: 10.1038/218731a0.

Haensel, P. et al. (2009). "Keplerian frequency of uniformly rotating neutron stars and strange stars". In: A&A 502, pp. 605–610. DOI: 10.1051/0004-6361/200811605. arXiv: 0901.1268 [astro-ph.SR].

Hays, E., T. Cheung, and S. Ciprini (2013). "Detection of gamma rays from Nova Delphini 2013". In: *The Astronomer's Telegram* 5302, p. 1.

Hebeler, K. et al. (2013). "Equation of State and Neutron Star Properties Constrained by Nuclear Physics and Observation". In: ApJ 773, 11, p. 11. DOI: 10.1088/0004-637X/773/1/11. arXiv: 1303.4662 [astro-ph.SR].

Hernanz, M. (2013). "Novae in gamma-rays". In: *ArXiv e-prints*. arXiv: 1301.1660 [astro-ph.HE].

Hessels, J. W. T. et al. (2006). "A Radio Pulsar Spinning at 716 Hz". In: *Science* 311, pp. 1901–1904. DOI: 10.1126/science.1123430. eprint: astro-ph/0601337.

Hjorth, J. et al. (2003). "A very energetic supernova associated with the $\gamma$-ray burst of 29 March 2003". In: Nature 423, pp. 847–850. DOI: 10.1038/nature01750. eprint: astro-ph/0306347.

Ivanova, N. (2013). "Low-mass X-ray binaries in globular clusters: puzzles and solutions ". In: Mem. Soc. Astron. Italiana 84, p. 123. arXiv: 1301.2203 [astro-ph.HE].

Klebesadel, R. W., I. B. Strong, and R. A. Olson (1973). "Observations of Gamma-Ray Bursts of Cosmic Origin". In: ApJ 182, p. L85. DOI: 10.1086/181225.

Kouveliotou, C. et al. (1993). "Identification of two classes of gamma-ray bursts". In: ApJ 413, pp. L101–L104. DOI: 10.1086/186969.

Kumar, P. and R. Narayan (2009). "GRB 080319B: evidence for relativistic turbulence, not internal shocks". In: MNRAS 395, pp. 472–489. DOI: 10.1111/j.1365-2966.2009.14539.x. arXiv: 0812.0021.

LOFT Consortium (2012). "Strong gravity studies with the Large Observatory For X-ray Timing (LOFT) ". In: Mem. Soc. Astron. Italiana 83, p. 352.

Lasota, J.-P. (2001). "The disc instability model of dwarf novae and low-mass X-ray binary transients". In: New A Rev. 45, pp. 449–508. DOI: 10.1016/S1387-6473(01)00112-9. eprint: astro-ph/0102072.

– (2004). "The implications of disc instabilities on cataclysmic variable structure and evolution". In: *Revista Mexicana de Astronomia y Astrofisica Conference Series*. Ed. by G. Tovmassian and E. Sion. Vol. 20. Revista Mexicana de Astronomia y Astrofisica, vol. 27, pp. 124–127. eprint: astro-ph/0402190.

Lense, J. and H. Thirring (1918). "Über den Einfluß der Eigenrotation der Zentralkörper auf die Bewegung der Planeten und Monde nach der Einsteinschen Gravitationstheorie". In: *Physikalische Zeitschrift* 19, p. 156.

Levine, A. M. et al. (1996). "First Results from the All-Sky Monitor on the Rossi X-Ray Timing Explorer". In: ApJ 469, p. L33. DOI: 10.1086/310260. eprint: astro-ph/9608109.

Lo, Ka Ho et al. (2013). "Determining Neutron Star Masses and Radii Using Energy-resolved Waveforms of X-Ray Burst Oscillations". In: *The Astrophysical Journal* 776.1, p. 19.

Lyutikov, M. (2006). "The electromagnetic model of gamma-ray bursts". In: *New Journal of Physics* 8, p. 119. DOI: 10.1088/1367-2630/8/7/119. eprint: astro-ph/0512342.

Lyutikov, M. and R. Blandford (2003). "Gamma Ray Bursts as Electromagnetic Outflows". In: *ArXiv Astrophysics e-prints*. eprint: astro-ph/0312347.

McConnell, N. J. et al. (2011). "Two ten-billion-solar-mass black holes at the centres of giant elliptical galaxies". In: Nature 480, pp. 215–218. DOI: 10.1038/nature10636. arXiv: 1112.1078 [astro-ph.CO].

McKinney, J. C. and D. A. Uzdensky (2012). "A reconnection switch to trigger gamma-ray burst jet dissipation". In: MNRAS 419, pp. 573–607. DOI: 10.1111/j.1365-2966.2011.19721.x. arXiv: 1011.1904 [astro-ph.HE].

Mészáros, P. and M. J. Rees (2000). "Steep Slopes and Preferred Breaks in Gamma-Ray Burst Spectra: The Role of Photospheres and Comptonization". In: ApJ 530, pp. 292–298. DOI: 10.1086/308371. eprint: astro-ph/9908126.

Narayan, R., B. Paczynski, and T. Piran (1992). "Gamma-ray bursts as the death throes of massive binary stars". In: ApJ 395, pp. L83–L86. DOI: 10.1086/186493. eprint: astro-ph/9204001.

Paul, B. and S. Naik (2011). "Transient High Mass X-ray Binaries". In: *Bulletin of the Astronomical Society of India* 39, pp. 429–449. arXiv: 1110.4446 [astro-ph.HE].

Pélangeon, A. et al. (2008). "Intrinsic properties of a complete sample of HETE-2 gamma-ray bursts. A measure of the GRB rate in the Local Universe". In: A&A 491, pp. 157–171. DOI: 10.1051/0004-6361:200809709. arXiv: 0811.3304.

Pian, E. et al. (2006). "An optical supernova associated with the X-ray flash XRF 060218". In: Nature 442, pp. 1011–1013. DOI: 10.1038/nature05082. eprint: astro-ph/0603530.

Pons, J. A. et al. (2002). "Toward a Mass and Radius Determination of the Nearby Isolated Neutron Star RX J185635-3754". In: ApJ 564, pp. 981–1006. DOI: 10.1086/324296. eprint: astro-ph/0107404.

Psaltis, D., F. Ozel, and D. Chakrabarty (2013). "Prospects for Measuring Neutron-Star Masses and Radii with X-Ray Pulse Profile Modeling". In: *ArXiv e-prints*. arXiv: 1311.1571 [astro-ph.HE].

Rashevsky, A. et al. (2002). "Large area silicon drift detector for the ALICE experiment". In: *Nuclear Instruments and Methods in Physics Research A* 485, pp. 54–60. DOI: 10.1016/S0168-9002(02)00531-4.

Rauer, H. et al. (2013). *PLATO, Assessment Study Report*. Tech. rep. European Space Agency.

Reig, P. (2011). "Be/X-ray binaries". In: Ap&SS 332, pp. 1–29. DOI: 10.1007/s10509-010-0575-8. arXiv: 1101.5036 [astro-ph.HE].

Sakamoto, T. et al. (2008). "Global Properties of X-Ray Flashes and X-Ray-Rich Gamma-Ray Bursts Observed by Swift". In: *The Astrophysical Journal* 679.1, p. 570.

Schwarz, G. J. et al. (2011). "Swift X-Ray Observations of Classical Novae. II. The Super Soft Source Sample". In: ApJS 197, 31, p. 31. DOI: 10.1088/0067-0049/197/2/31. arXiv: 1110.6224 [astro-ph.SR].

Seward, F.D. and P.A. Charles (2010). *Exploring the X-ray Universe*. Cambridge University Press.

Shemi, A. and T. Piran (1990). "The appearance of cosmic fireballs". In: ApJ 365, pp. L55–L58. DOI: 10.1086/185887.

Singh, K. P. (2013). "X-ray emission from magnetic cataclysmic variables". In: *Astronomical Society of India Conference Series*. Ed. by S. Das, A. Nandi, and I. Chattopadhyay. Vol. 8. Astronomical Society of India Conference Series, pp. 115–122. arXiv: 1310.0579 [astro-ph.HE].

Tauris, T. M. and E. P. J. van den Heuvel (2006). "Formation and evolution of compact stellar X-ray sources". In: *Compact stellar X-ray sources*. Ed. by W. H. G. Lewin and M. van der Klis, pp. 623–665.

Veres, P. and P. Mészáros (2012). "Single- and Two-component Gamma-Ray Burst Spectra in the Fermi GBM-LAT Energy Range". In: ApJ 755, 12, p. 12. DOI: 10.1088/0004-637X/755/1/12. arXiv: 1202.2821 [astro-ph.HE].

Woosley, S. E. and J. S. Bloom (2006). "The Supernova Gamma-Ray Burst Connection". In: ARA&A 44, pp. 507–556. DOI: 10.1146/annurev.astro.43.072103.150558. eprint: astro-ph/0609142.

Woosley, S. E. and A. Heger (2014). "The Deaths of Very Massive Stars". In: *ArXiv e-prints*. arXiv: 1406.5657 [astro-ph.SR].

Zdunik, J. L. and P. Haensel (2013). "Maximum mass of neutron stars and strange neutron-star cores". In: A&A 551, A61, A61. DOI: 10.1051/0004-6361/201220697. arXiv: 1211.1231 [astro-ph.SR].

Zhang, B. and H. Yan (2011). "The internal-collision-induced magnetic reconnection and turbulence (ICMART) model of gamma-ray bursts". In: ApJ 726, 90.

van Rantwijk, J. (2010). "SpaceWire Light". In: *opencores.org/*.

van der Klis, M. et al. (1996). "Discovery of Submillisecond Quasi-periodic Oscillations in the X-Ray Flux of Scorpius X-1". In: *The Astrophysical Journal Letters* 469.1, p. L1.

# Statement of Authorship

I hereby state that this diploma thesis with the title ***Development of the Back End Electronics for the Wide Field Monitor on-board LOFT*** has been composed by myself, Florian Jetter, and describes my own work unless otherwise acknowledged in the text.

Tübingen, July 14, 2014

# Erklärung der Urheberschaft

Hiermit erkläre ich, Florian Jetter, dass ich die vorliegende Diplomarbeit mit dem Titel ***Development of the Back End Electronics for the Wide Field Monitor on-board LOFT*** selbstständig verfasst und dabei keine anderen als die angegebenen Quellen und Hilfmittel benutzt habe.

Tübingen, den 14. Juli 2014